Spring 1-1-2010

Assessing Supraglacial Water Volume and the Changing Dynamics of the Surface Topography Near the Jakobshavn Glacier, Greenland

John Adler
University of Colorado at Boulder, john.adler@colorado.edu

Assessing supraglacial water volume and the changing dynamics of the surface topography near the Jakobshavn Glacier, Greenland

by

John J. Adler

B.A., University of California, Santa Barbara, 1987

B.S. University of California, Santa Barbara, 1987

M.S. Physics, Naval Postgraduate School, 1993

A thesis submitted to the Faculty of the Graduate School of the

University of Colorado in partial fulfillment of the requirement for the degree of

Doctor of Philosophy

Department of Geography

2010

This thesis entitled:

Assessing supraglacial water volume and the changing dynamics of the surface topography near the Jakobshavn Glacier, Greenland

for the Doctor of Philosophy degree

written by

John J. Adler

has been approved for the Department of Geography

By

_____

Dr. Konrad Steffen

_____

Dr. James Maslanik

The final copy of this thesis has been examined by the signatories, and we find that both the content and the form meet acceptable presentation standards of scholarly work in the above mentioned discipline. Date: November 19th, 2010

Abstract

Adler, John (Ph.D., Geography)

Assessing Supraglacial Water Volume and the Changing Dynamics of the Surface Topography Near the Jakobshavn Glacier, Greenland

Thesis directed by Professor Konrad Steffen

On the Greenland Ice Sheet (GIS), the effect of the melt season's changing supraglacial lakes on outlet glacier discharge is not well understood. It is known that many supraglacial lakes drain rapidly during each melt season. While there are conflicting theories of the significance of supraglacial lake drainages towards enhancing ice sheet flow, it is highly important to quantify the actual water volume of supraglacial lakes since their drainage via crevasses or moulins enables the injection of melt water directly into the GIS.

The 2008 Arctic MUltiSensor Cryospheric Observation eXperiment (Arctic MUSCOX) was the first scientific Unmanned Aircraft System (UAS) used in Greenland. The goal was determination of the changing volumes of supraglacial melt water lakes through the fusion of disparate data sets from in-situ, airborne, and satellite sensors. Near the Jakobshavn Isbrae region, four supraglacial lakes at different elevations along a transect at 68.73°N were monitored over the 2006, 2007, and 2008 melt seasons. The changing lake volumes are calculated for each day of usable MODIS imagery, employing DEM's from both

ASTER Global and the MUSCOX lidar survey. During this three year period, no observed lake was larger in volume than 0.15km^3, or larger in area than 10.4km^2, implying a size limit for supraglacial lakes.

In this study a new technique is developed calculating runoff using daily changing albedo and surface height measurements (dH) from the Greenland Climatic Network (GC-Net) Automatic Weather Stations (AWS) at locations JAR1 and JAR2. Runoff is calculated on a daily basis, both regionally and for a 1,183km^2 inset strip straddling the transect. At JAR1 the calculated linear runoff for 2006, 2007, and 2008 is 1.79m, 1.99m, and 1.96m, respectively; at JAR2 the calculated runoff is 2.11m, 2.86m, and 2.40m, respectively. Regional projections are made that account for future atmospheric temperature increases between 0.5°C and 3.0°C; they indicate up to a 43.3% increase in the area available for the formation of supraglacial lakes in the GIS.

Finally, a proposal is presented to obtain scientific measurements of Arctic Key Parameters (AKP's) in the region's data sparse areas via UAS through the cooperation of the international community.

Dedication

To my father who showed the path forward in so many ways,

and

To my mother who never gave up on what she believed in.

Acknowledgements

I would like to give my deepest gratitude to those who supported this project, and who continue to support its future efforts. My special thanks goes to my advisor, Dr. Konrad Steffen, who mentored me through all aspects of my Ph.D. program. I would also like to thank Drs. James Maslanik, Marty Ralph, and Betsy Weatherhead who all believed in the mission from the beginning and enabled it to happen. I am also deeply grateful to Mr. Mark Angier who put his faith, and his company's backing, in using autonomous unmanned aircraft for scientific purposes. I would also like to thank my other committee members, Drs. Peter Blanken, Roger Pielke, Jr., and Mark Serreze, who helped me navigate through academic challenges. My best wishes are to Ian Crocker, my fellow graduate student, who ensured all systems were "go".

Many enterprises pulled together to enable these flights, the first civil use of unmanned aerial vehicles in Greenland: Advanced Ceramics Research, UNAVCO, VECO, the 109th Airlift Wing, Air Greenland, the Danish Aviation Flight Authorities, Digital Globe, and the Office of Marine and Aviation Operations of NOAA. My hat is off to all the members of these organizations who each assisted in many unseen ways in making this project so successful.

There are four other individuals who were with me in a virtual sense throughout this journey: Kevin F. Baird, Miles Davis, Jean Luc Ponty, and Pat Metheny. Kudos for making all of the moments so sublime.

Most importantly, I need to deeply thank my wife Diane who began this trek with me, and carried me throughout the past four years to its completion; she is always there with a cheerful word and a thoughtful deed regardless of the hecticity of the situation!

Y mi tres amigos, Austen, Ian, and Collin: we were able to grow together even though we were apart. May the force be with all three of you, mi hijos!

John J. Adler

Table of Contents

List of Tables

List of Figures

Chapter 1: Project Introduction

Motivation

The southwestern flank of the Greenland Ice Sheet (GIS) has numerous melt lakes that form on the surface of the ice during the summer melt season. This project calculates the volume of water present in the supraglacial lakes near the Jakobshavn Isbrae region on the GIS, shown in Fig. 1-1. The relationship between the ice sheet ablation region and supraglacial lake formation and drainage is not well understood (Luthcke et al., 2006), though recently more attention has been paid to this important process. This lack of understanding is partly due to the challenge and dangers of measuring supraglacial lake depths in remote Arctic regions, and partly due to the complexity of the physical system itself.

Fig. 1-1: Global view of the Greenlandic study area.

Recent studies show supraglacial lake areal extents are between 0.5% and 1.0% of the ice sheet area in the southwest, northwest, and the northeastern portions of the GIS

(Sundal et al., 2009). This study is in the southwestern portion of the GIS as shown in Fig. 1-2, also seen is the local town of Ilulissat and the locations of three Automated Weather Stations (AWS): JAR1, JAR2, and Swiss Camp. Of note, the town of Ilulissat, Greenland has an airfield and is an ideal research logistic center from which to assess melt water volume stored in supraglacial lakes on the ice sheet.

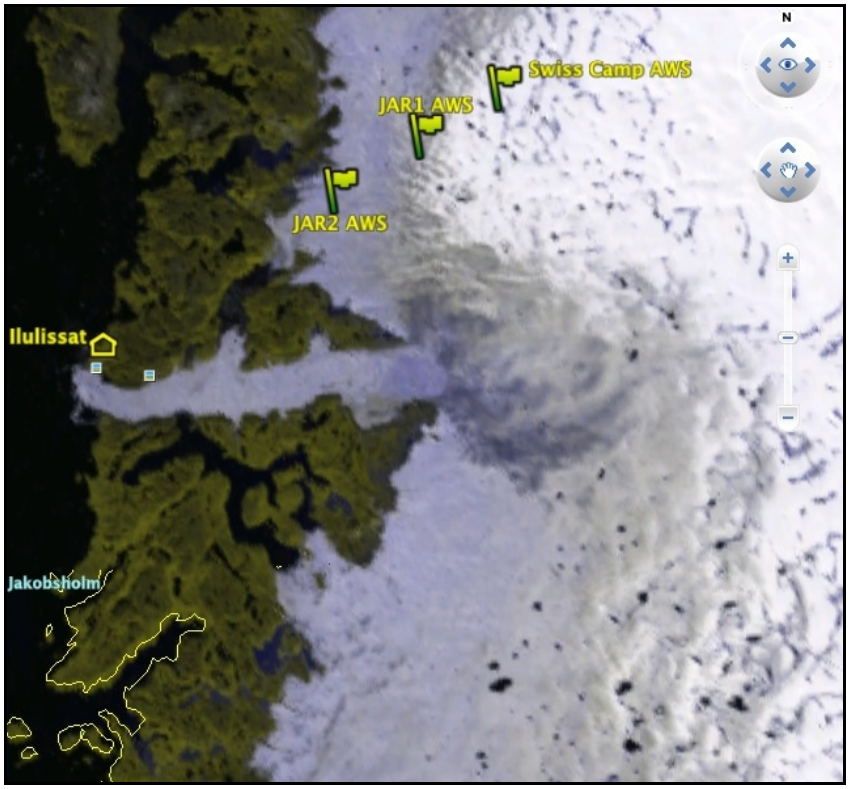

Fig. 1-2: The Jakobshavn study region near Ilulissat, Greenland.
(from NASA MODIS imagery, 29 Jul 2006 at 1605z)

If Arctic warming (Serreze and Francis, 2006) continues, it is theorized more melt and runoff will occur, resulting in more supraglacial lake formations and the appearance of supraglacial lakes at higher elevations. If supraglacial lakes (also referred to as 'lakes' in this study) were static (or even on a static surface), volume estimates, once made, would be highly reliable over time. However, supraglacial lakes have two complicating factors: a) the entire base of ice upon which a supraglacial lake sits is itself in motion; and

b) lake drainage events occur, where the entire lake drains in less than 24 hours (Das et al., 2008) into the ice sheet itself. It is this large quantity of water that can disappear into the ice sheet that motivates this study.

Ice sheet dynamics is the response of ice sheets to forcing conditions such as ice-temperature evolution, grounding-line migration, and flow law (Huybrechts and de Wolde, 1999). The correlation of ice sheet dynamics with supraglacial lake water volume has not received much scientific attention in the past (Zwally et al., 2002), and could be important if the lakes can directly transfer heat and lubricating fluid to the glacier base, or if they enhance englacial water movements.

Some speculate that once water moves beneath a glacier, the coefficient of friction for the glacial movement is reduced, allowing the glacier to move more quickly downslope to the sea (Vaughan and Athern, 2007). Although the dynamics are not yet understood, it has been shown that flow rates of some glaciers have doubled over a recent 5 year period (Dowdeswell, 2006), and that melt water may play an important role.

Others speculate the melt water will enlarge the existing drainage channels found within a glacier, creating a more robust drainage network (personal communications with Ian Howat, December 2009 and January 2010). The more efficient water drainage system would actually increase the coefficient of friction and slow a glacier's advance.

Another important aspect of the GIS melt water and runoff is its contribution to sea level rise. During the 20th century the global average sea level rise rate was estimated by the UN Intergovernmental Panel on Climate Change (IPCC) to be 1.7mm/yr, with a current rate (1993-2006) of 3.1mm/yr (IPCC, 2007). Greenland's estimated contribution

to sea level rise ranges between 0.13mm/yr and 0.74mm/yr (van den Broeke et al., 2009).

While the annual net precipitation differences will affect the absolute amount of Greenland's contribution to sea level change, the percent contribution between calving ice and runoff appears relatively similar to each other. Hanna et al. (2005) found the ratio between runoff and the summation of calving ice and bottom melt to be 1.0 between 1961-1990, 1.3 between 1993-1998, and 1.4 between 1998-2003. Accurate runoff calculations are therefore relatively as important as calving ice mass calculations.

If the earth continues to experience climatic warming, logically the amount of liquid water present on the surface of the ablation zone will increase during the summer melt season. Further, it is logical to predict that there will be more supraglacial lakes forming at higher elevations due to an increase in ambient temperature. The result of increasing melt area with altitude has already been documented by Huff and Steffen in 2005, as shown in Fig. 1-3. The image shows the increased melt area from 1992 to 2005, as derived from passive microwave techniques described by Abdalati and Steffen (1997).

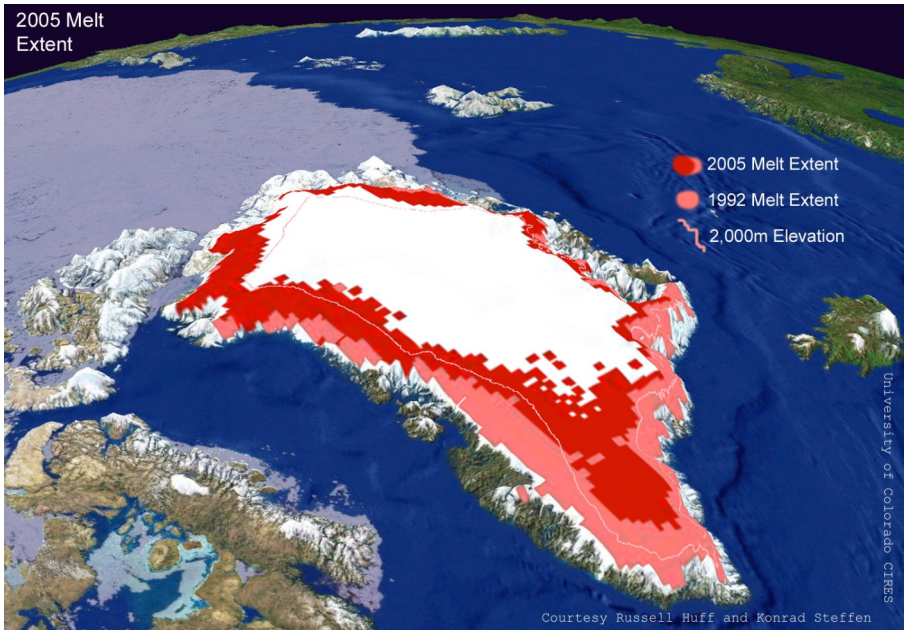

Fig. 1-3: Increasing melt with altitude as detected by passive microwave instruments on polar orbiting spacecraft. http://cires.colorado.edu/steffen/greenland/melt2005/

Additionally, higher elevations (>1500m) of the western GIS have a more gradual slope than the lower elevations (<1000m), as shown in Fig. 1-4. Here, the formation of supraglacial lakes would also be aided by the topography, since less slope discourages runoff. Therefore, if climatic warming continues, the higher and flatter areas of the GIS should begin to experience supraglacial lake formation in addition to the existing supraglacial lake areas. Thus it is important to develop a way to accurately and efficiently measure lake water volumes beyond in-situ methods that rely on human deployment, monitoring, and recovery.

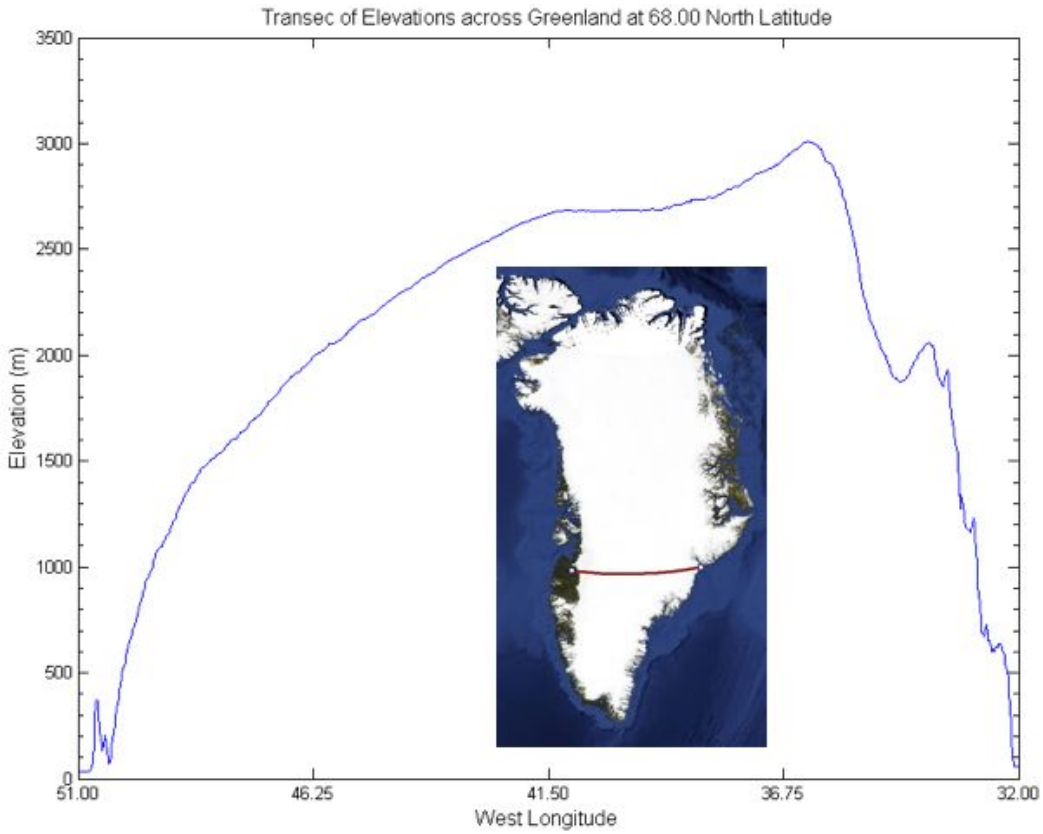

Fig. 1-4: The elevation of the Greenland Ice Sheet at 68° N from west to east. Note the steeper slope in the west below 1000m elevation. Inset graphic shows the transect line in red, across the GIS. (Digital Elevation Model from Scambos and Haran, 2002)

Measuring the volume of a lake requires knowledge of all three dimensions: width, breadth, and depth. While satellite images such as MODIS (Moderate Resolution Imaging Spectroradiometer) provide an aerial view of width and breadth, no accurate depth information is readily available. Limited in-situ measurements of Greenlandic glacial lake depths have been made (Box and Ski, 2007; Das et al., 2008; Luthcke et al., 2006) on a handful of supraglacial lakes. Box and Ski directly sounded two of the 24 lakes in their study; their estimated maximum depth of any of the 24 lakes was 12.2m. Das et al. also measured supraglacial lake depths, finding a maximum measured depth between two

specific points to be 9m. The limited in-situ collections by scientists are due to both funding and logistic challenges. Traveling in the ablation region by skidoo is potentially hazardous due to crevasse crossings, and has limited geographical coverage. Flying by fixed-wing aircraft or helicopter is very expensive; while manned aircraft missions are tenable for a small number of lakes, it is not economically feasible for the large numbers of supraglacial lakes that appear on the West Coast of Greenland, as shown in Fig. 1-2.

The mission of the Arctic MUltiSensor Cryospheric Observation eXperiment (Arctic MUSCOX) is to determine the volume of supraglacial melt water lakes. Arctic MUSCOX was founded in 2007, and uses small (wingspan <2m) unmanned aerial vehicles (UAV's) to collect light detection and ranging (lidar) rangefinder, hyperspectral imagery, color video, ambient temperature, humidity, and surface temperature information when flying over supraglacial lakes. The ability to measure numerous supraglacial lake volumes very rapidly, and at low cost, would enable many new data points for future modeling of englacial water movements and runoff processes.

As described in this dissertation, employing UAV's to obtain these data is a practical and prudent way to gather scientific measurements in remote regions such as the Arctic. These autonomous flying devices are known in a broader sense as Unmanned Aircraft Systems (UAS). The term UAS includes the supporting ground stations, communications equipment, and related system software to ensure successful mission flights; the term UAV applies specifically to the airborne vehicle. Both acronyms will be used throughout this dissertation, particularly in Chapter 7, dedicated to the efficacy of using UAS across the Arctic for gathering scientific data to monitor changes in climate, sea ice thickness, and ocean surface temperature.

Research Objectives

The overall goal of this study is to determine supraglacial melt lake volumes on a daily basis during the melt season in western Greenland's ablation region. A secondary goal is to characterize these volumes as a percentage of available local runoff. This information is needed to better understand how large ice sheet melt and runoff contribute to global sea level changes and outlet glacier movements.

The purpose of this research is to characterize the daily surface runoff in the ablation region of southwestern Greenland by looking in detail at one area, near the Jakobshavn Isbrae, during the melt season (defined as May 13th to August 31st) of three years: 2006, 2007, and 2008. This area was chosen due to the large number of melt lakes, and its proximity to a usable airfield. The three years were chosen to provide a high melt year (2007), a moderate melt year (2006), and the reference year (2008) when the UAV flew.

After calculating the total daily available volume of liquid water, the study will determine how much water is actually retained in storage form, via daily MODIS satellite images of supraglacial lakes on the ice sheet surface and a Digital Elevation Model (DEM). Using various in-situ and remote sensing techniques the following research questions will be answered:

1. Can automated weather station surface height measurements be used to calculate daily and seasonal surface melt water equivalent (MWE)?
2. What is the daily and total seasonal runoff for the ablation region in the observed study area for 2006, 2007, and 2008?

3. Can supraglacial lake volumes be determined from DEM topography at 30m or 625m resolution, and how do they compare to an unmanned airborne lidar survey within the study area?

4. Is the derived lake volume accurate enough to study interseasonal variability?

5. How much melt water is retained in supraglacial lakes as compared to the total annual runoff?

Methodological Overview

The July 2008 Arctic MUSCOX project investigated supraglacial lakes near the Jakobshavn Isbrae region. The combination of laser profiling techniques from the UAS, moderate-resolution satellite imagery, and the new 2009 ASTER (Advanced Spaceborne Thermal Emission and Reflection Radiometer) Global DEM enabled detailed mapping and the calculation of supraglacial lake volumes.

Fig. 1-5 is a flow chart introduced to help clarify the process of determining supraglacial lake volumes relative to calculated runoff for the study region. Inputs are on the left, and consist of in-situ, DEM's, and satellite imagery. Outputs are the daily lake volumes and runoff calculations. The blue shapes in the middle functionally describe the interactions of the inputs to enable these calculations. It is hoped the graphic will enable the reader to better understand the interactions described in this dissertation.

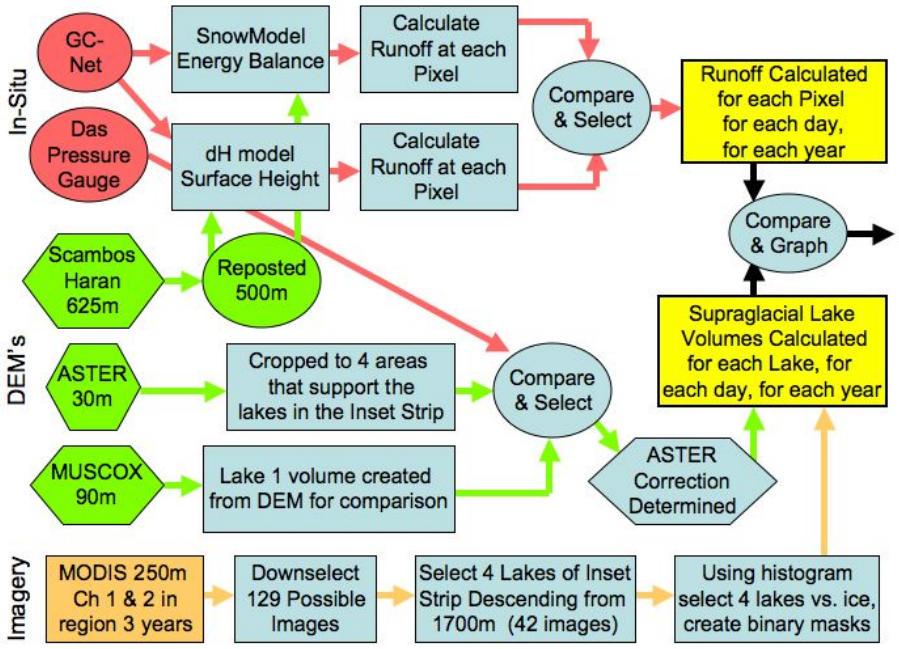

Fig. 1-5: Functional overview of the calculation processes to determine lake volumes.

Previously, manned airborne lidar measurements of terrain elevation have allowed for precise determination of ice sheet elevation (Krabill et al., 1995). By flying annually or bi-annually over the same flight tracks, elevation changes (and hence mass changes) were determined using lidar measurements. Arctic MUSCOX's unmanned flights augment the previous measurements by producing a high resolution DEM where each flight track is separated by only 250m, vs. the 5km spacing of the manned missions. Segments of this project were deliberately flown over the same terrain as the 2008 Airborne Topographic Mapper (ATM) mission flights to facilitate data comparison.

Most previous investigations into calculating Greenland's melt water and runoff used broad climate indicators and modeling techniques that rely on both manned and unmanned weather station observations. Data sets are used from coastal weather stations, run by the Danish Meteorological Institute (DMI), and interior automated

weather stations located throughout the ice sheet and run by Dr. Konrad Steffen (Steffen and Box, 2001). One approach to calculate melt and runoff involves calculating the number of Positive Degree Days (PDD), and applying this to various elevations along the western GIS. A second approach, adopted by this study, calculates melt and runoff using surface height changes observed by the AWS.

Estimates of Greenland's total runoff for 1995-2007 are on the order of ~400 km^3/yr, as shown in Fig. 1-6 (Mernild et al., 2010). This study calculates runoff only in the vicinity of the Jakobshavn region, but the results could be extrapolated to a larger area.

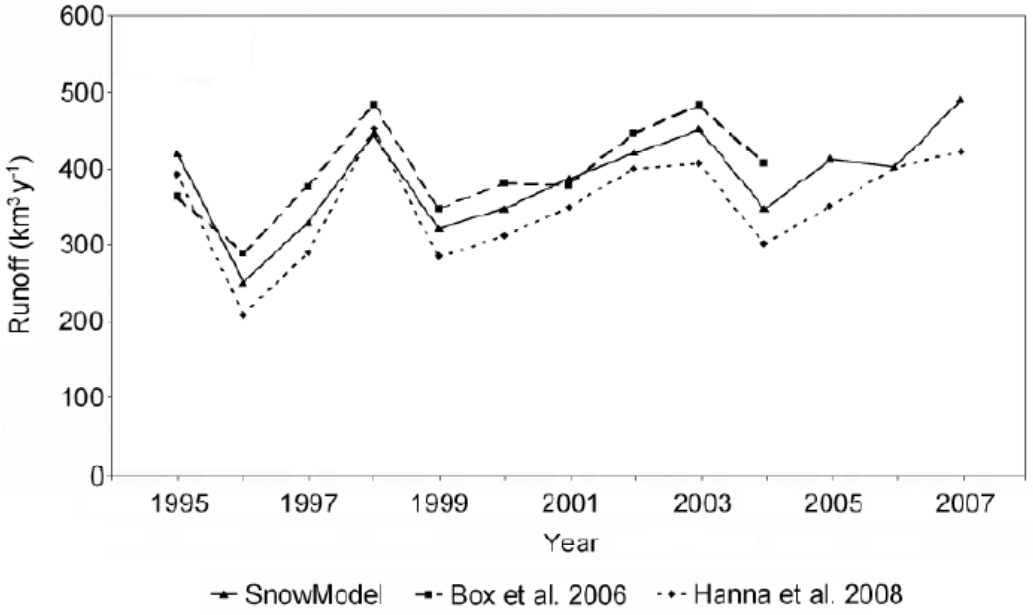

Fig. 1-6: Three Greenland runoff calculation results as compiled by Mernild et al. (2010)

In-situ measurements are made by the Greenland Climatic Network (GC-Net) series of 18 AWS. Two stations in particular, JAR1 (elevation 962m) and JAR2 (elevation 568m) near the Jakobshavn Isbrae region are used in this study; their locations are shown in Fig. 1-2. Daily average readings of 2m temperature, humidity, albedo, surface height change,

wind speed, and wind direction were computed for the melt seasons during 2006, 2007, and 2008 from JAR1 and JAR2. Approximately 110 days were analyzed during the melt season for each year.

A simulated runoff for each geographic pixel location of the study area was created by Dr. Sebastian Mernild of the Los Alamos National Laboratory using the four-section energy balance computer program SnowModel (Liston and Elder, 2006). SnowModel, as modified by Mernild et al. (2010), computes simulated runoff calculations from inputs of temperature, humidity, wind speed and wind direction. It is used as a reference for the calculations made in this dissertation.

This study developed a new runoff model based on observed height changes (dH) of snow and ice on the surface. The Matlab-based dH Model was created using sonic height measurements made at JAR1 and JAR2. Daily height changes of the ice sheet were obtained at these locations and processed independent of the SnowModel program to calculate linear runoff, defined as the vertical water equivalent of the surface height loss at a particular location (a datum point).

After obtaining the GC-Net AWS environmental data from Dr. Konrad Steffen, the AWS data were processed to remove any discovered spurious data. Temperature, humidity, wind speed, wind direction, incoming shortwave, outgoing shortwave, and changes in ice/snow height observations were processed to obtained 24-hour averages. For example, Fig. 1-7 shows in red the 2006 JAR1 raw surface height changes in meters, as measured by the two sonic instruments. Smoothed individual dH data are shown in green and labeled “smoothed” for each instrument. The final 24-hour two-instrument average dH product is shown in black. For the SnowModel simulations, averaged

temperature, humidity, wind speed, and wind direction were used as inputs. For the dH Model, incoming shortwave, outgoing shortwave, and surface height change were used as inputs.

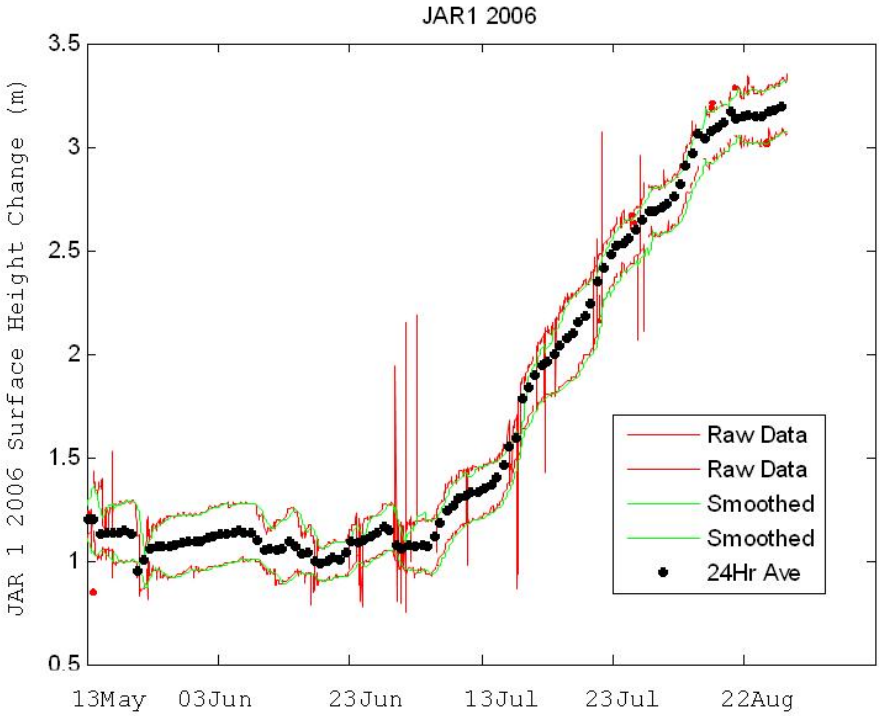

Fig. 1-7: Example of processed 2006 JAR1 AWS data processed from surface height change (dH) measurements averaged over 24-hour periods.

After calculating the regional surface runoff, a small inset strip of supraglacial lakes, as shown in Fig. 1-8, was selected for detailed analysis. The area was chosen because the supraglacial lakes cascade downward from 1361m to 993m along a direct line, and Arctic MUSCOX overflew three of the lakes in 2008. Secondarily, the four chosen lakes were large enough that 250m resolution MODIS images could detect surface area changes over time.

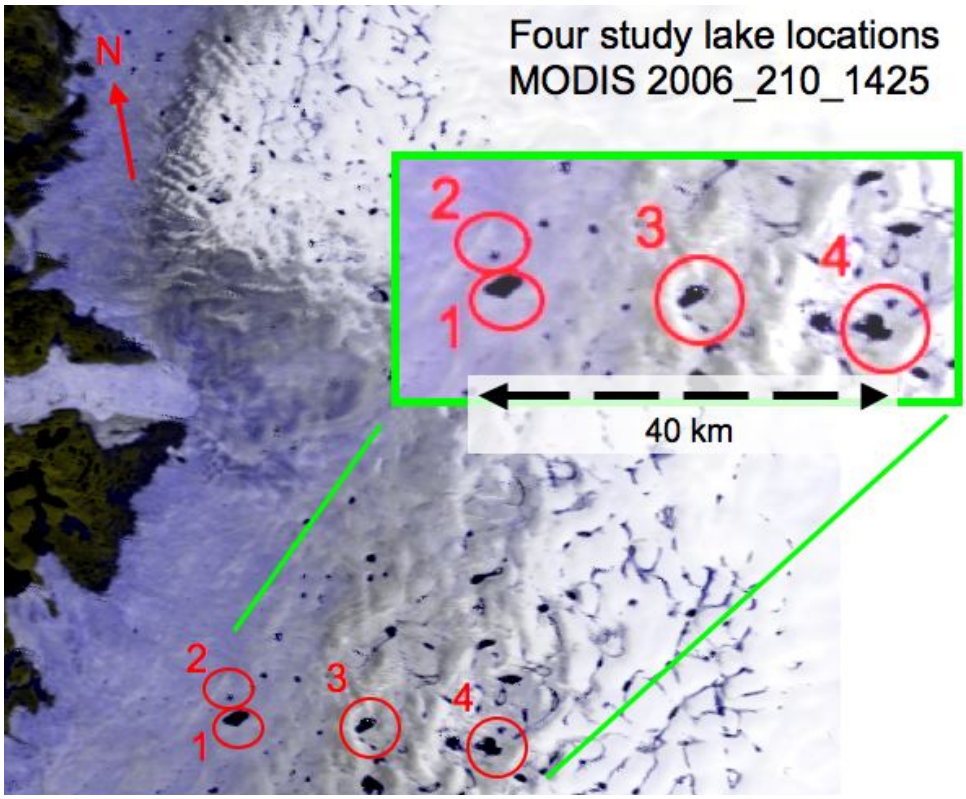

Fig. 1-8: The inset strip of four supraglacial lakes used in this study for detailed volume analysis and runoff calculations. Lakes 1, 2, and 3 were overflown by the Manta UAV in July, 2008.

The location and elevation of each lake are given in Table 1-1; no estimate is given for Lake 4 from the Arctic MUSCOX campaign because it was the only lake not overflown.

Table 1-1: Location and elevation of each supraglacial lake studied. Elevations are indicated for each DEM

Lake	Latitude (N)	Longitude (W)	MUSCOX (m)	Scambos - Haran (m)	ASTER (m)
1	68.720	049.500	985	1014	922
2	68.750	049.535	968	997	923
3	68.709	049.025	1204	1215	1154
4	68.674	048.556	-	1363	1270

Three DEM's are utilized in this study due to the strengths and limitations of each DEM dataset. The newest DEM, ASTER Global, did not have an outlier removal and

smoothing filter applied before its release. Even re-posting the ASTER DEM to 500m resolution and applying a smoothing algorithm resulted in erroneous elevation fluctuations. The 625m DEM from Scambos and Haran (2002) was employed, but due to the large pixel size artificially low lake volumes were produced. A third DEM (the MUSCOX DEM) was created using the lidar elevation points collected during five UAV flights, providing a detailed physical description of a recently drained lake bottom. The Lake 1 volume estimate (0.043 km^3) from the MUSCOX DEM, compared very favorably to a volume estimate (0.044 km^3) calculated from an in-situ pressure sensor located at the bottom of Lake 1 (Das et al., 2008).

The MUSCOX DEM, and the in-situ depth gauge were combined to provide a ground-checked reference for the entire modeled area. This analysis resulted in a correction factor of 0.42 for the ASTER DEM during volumetric analysis, as described in Chapter 3.

This study better quantifies surface runoff water estimates by estimating standing water volume of the surface lakes on the ice sheet as a percentage of total calculated runoff. The difference between the calculated runoff and standing water is the amount of water available to move as englacial flow within the ice sheet, or supraglacial flow on the ice sheet's surface.

Surface water flow will follow the gradient of gravity, barring some physical barrier. Physical barriers on the ice sheet consist of crevasses, mounds, and other forms of frozen water, as shown in Fig. 1-9.

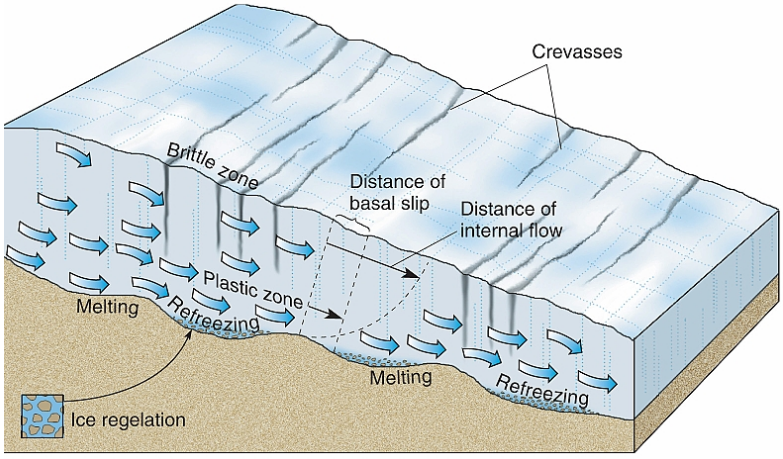

Fig. 1-9: Notional glacial surface and subsurface features.
(Christopherson, 2009)

Recent work discusses the two processes that must occur before melt water becomes runoff. First, the percolating melt water must raise the temperature of the snow pack to the melting point; secondly, the irreducible water content conditions in the snow/pore matrix must be met; essentially, the capillary pressure airspace voids must be filled. Assuming these conditions are met, it was found that the maximum extent of runoff over one season from an elevation of 1700m near the Jakobshavn region would be 5km; from an elevation of 1000m the maximum extent of runoff would be 12km (Rick, 2008). This implies surface water could run between relatively close lakes, such as between Lakes 1 and Lake 2, but it is improbable water from Lake 3 could travel on the surface to reach Lake 1 or Lake 2.

Runoff is calculated over the entire large study region (13,102km^2 non-masked) using two methods: 1) the observed changes in snow/ice height (dH) at two GC-Net AWS stations converted to runoff values, and 2) employing the energy balance program SnowModel to compute simulated runoff. Both the dH Model and SnowModel techniques

are then compared to the in-situ measurements, and the dH Model was selected for runoff calculations in the smaller inset strip study area (1,183km^2 non-masked).

To determine the size and location of supraglacial lakes and monitor their changes over time, MODIS imagery was obtained over the three summer melt seasons (2006, 2007, and 2008). The four targeted lakes are arranged perpendicularly to the contour lines of the western part of the GIS. Using ENVI image processing software, 129 relatively cloud-free two-channel MODIS images were selected as usable, and cropped to the large study area size. Each resized image was then re-evaluated for cloud-free clarity over the 13km by 91km smaller inset strip selected for supraglacial lake volume analysis. Of the 129 initial images, 87 had to be discarded due to cloud obscuration of the lakes in question, leaving 42 MODIS images to calculate lake volumes.

Once the surface areas of the lakes were calculated, the depths were determined via Matlab DEM routines using the corrected ASTER DEM elevations. Finally the total liquid water volume of each lake, for each day, was calculated by combining the surface area and depth information.

Chapter Summary

This dissertation's objective is to develop a method for calculating supraglacial melt lake water volumes in the ablation zone near the Jakobshavn region of the Greenland Ice Sheet. This knowledge could help resolve unknown influences that melt water has on the basal motion of outlet glaciers once the supraglacial lakes drain into the ice sheet or along the ice surface. Additionally, a new technique to determine runoff from observed surface height changes is introduced, and the ratio of supraglacial lake volume (water storage) to total runoff is presented.

The importance of blending various data sources is discussed, including overhead satellite imagery, unmanned aircraft systems, and in-situ automated weather systems. The Arctic MUSCOX website (www.arcticmuscox.org) will have selected data from these mission posted. In the next chapter, background information is presented on Greenland's surface energy processes, with an emphasis on the summer melt season.

Chapter 2: Background

Climatology of the Greenland Ice Sheet

There are four distinct water-related facies, or zones, in Greenland's ice sheet denoted by the net change in water (mass) balance (Benson, 1960). The original designation of the four zones is shown in Fig. 2-1, where we see:

1. the dry zone where there is no surface melt,
2. the percolation zone where limited melting is locally absorbed by underlying snow,
3. the wet or soaked zone where the melt accumulates and can run locally at the surface, and
4. the ablation region where more water (mass) completely leaves the area via sublimation, calving, or runoff processes, than remains for the next season.

A second categorization of the Greenland Ice Sheet (GIS) involves dividing it into two general regions: an annual accumulation zone and an ablation zone, which are separated by the equilibrium line (Henneken et al., 1994). The equilibrium line altitude (ELA) is the elevation where there is no net change in ice surface height over a one-year period, and is a variable height depending upon its physical location in Greenland. Factors such as latitude (northward is colder, and therefore has a lower ELA), longitude (the eastern slopes are more moist than the western side of Greenland), and the slope/aspect of the surface affect the ELA (Zwally and Giovinetto, 2001).

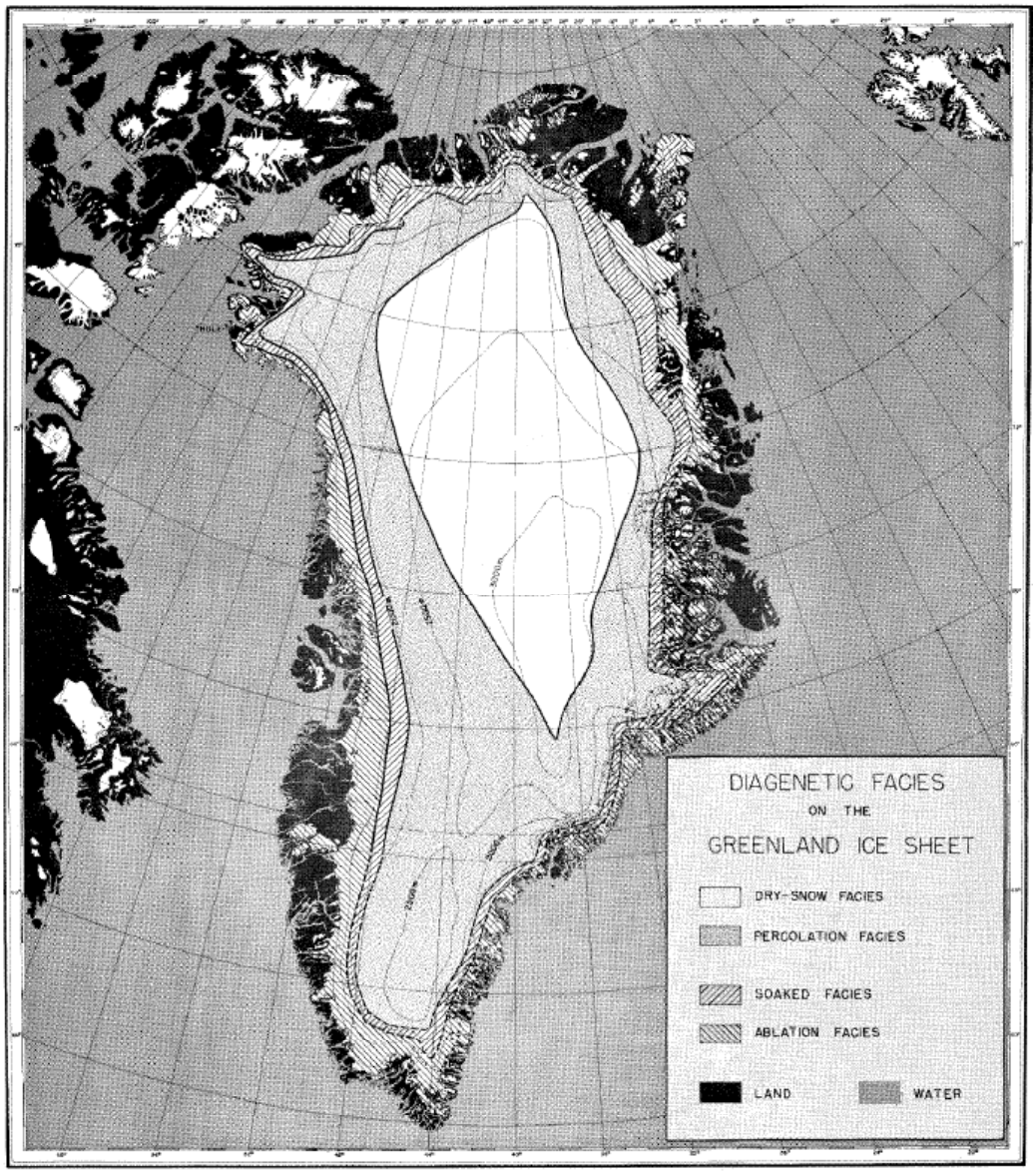

Fig. 2-1: The Four Major Water Zones on the Greenland Ice Sheet.
(Benson, 1960)

At the project location, the ELA is estimated to be 1250 meters, as shown in Fig. 2-2. This places Lakes 1, 2, and 3 below the ELA, and Lake 4 above the ELA (Table 1-1).

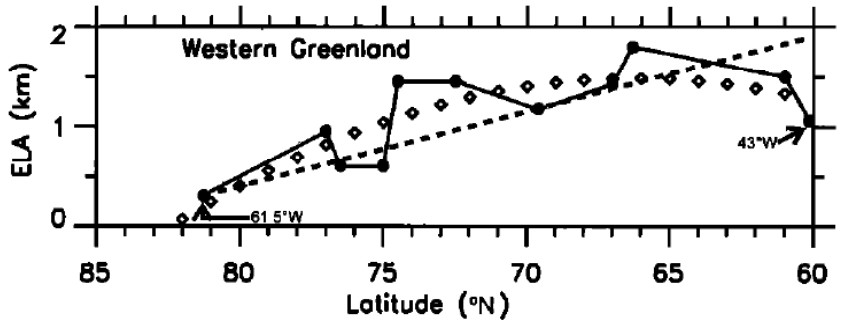

Fig. 2-2: The constantly varying elevation of the ELA. Dark circles are actual station measurements, diamond points are model output of the ELA, and the dashed line is a previous ELA model estimate combining both eastern and western Greenland data (Zwally and Giovinetto, 2001). This study's ELA is notionally at 1250m, based on the study location of ~68.3°N.

Energy Balances

While the model development for this study calculates runoff from changes in the ice sheet surface height (dH) as measured at the AWS sites JAR1 and JAR2, the dH occurs as a result of changes in surface energy balance. To discuss the surface processes in the ablation zone, we must first understand the incoming energy to the area, and then learn how the surface and the atmosphere interact throughout the annual cycle.

Radiative Shortwave and Longwave Fluxes

The sun is the energy input source for the solar system, the earth included. Without the sun, the earth would slowly radiate its stored internal energy and reduce its temperature from 288K (Ahrens, 2007) to that of a deep space body, namely 2.7K (NASA, 2009). For all intents and purposes, the bulk of the radiation from the sun is between 0.15μm and 3.0μm and is called shortwave (SW) radiation as shown in Fig 2-3. The distribution of the Earth's radiation is almost entirely between 3μm and 300μm, and is referred to as longwave (LW) radiation, also shown in Fig. 2-3.

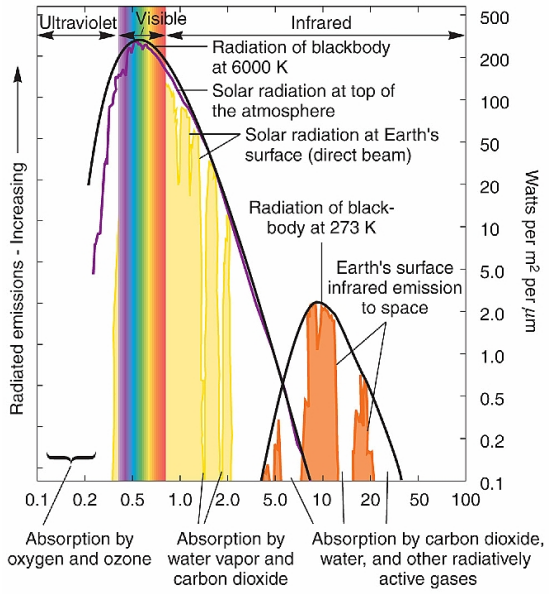

Fig. 2-3: Solar and Terrestrial Radiation. (Christopherson, 2009)

If there was no terrestrial atmosphere on the earth, its emittance as seen from space would appear nearly like a black body at 255K. Because the earth's atmosphere absorbs and reemits thermal radiation back towards the surface, the earth system is approximately 33K degrees warmer, at 288K (Randall, 2007). This results in peak radiation emitted at 10μm, as described by Wien's Law and shown by the nearly similar 273K degree curve in Fig. 2-3.

The incoming solar SW radiation to the earth system is partially reflected back into space by clouds and the earth's surface. The reflected SW radiation has different characteristics depending on what type of surface it impinges; of primary importance is the surface albedo. Albedo is the percentage of incident radiation that is reflected from a surface, and is wavelength dependent. The remaining incoming solar radiation is either absorbed or transmitted further into the atmosphere or the earth's surface. Snow has a high albedo, typically between 0.7 and 0.9; ice has a lower albedo, typically between 0.3

and 0.5 (Hock, 2005). It is this distinction between snow and ice that the dH Model will use to determine the type of the surface composition, and thus the density and meltwater equivalent of the surface height changes. For this study, reflected SW measured by the AWS will be used to calculate the daily surface albedo, which will be a proxy for snow/ice determination.

Over short time spans or regional areas, the earth's net energy balance is not always zero, especially in the polar regions where we have periods of 24-hour sunlight and 24-hour darkness. This implies the storage, movement, and/or usage of energy on different scales, both regionally and temporally. The energy storage function can be of various forms such as increased atmospheric humidity, atmospheric temperature, ice temperature, and the phase changes of water.

Energy Storage

The atmosphere can store and move energy via horizontal advection and vertical turbulence processes. These movements redistribute energy from areas with excess energy to places with relatively less energy. A good example is the re-distribution of energy due to hurricane activity where warm, moist, air is transferred to a cooler region hundreds of kilometers away.

Advection, the horizontal flow of an air parcel, will bring changes in the energy state of a particular area. Advection may bring a warmer or cooler parcel of air, which will be governed by sensible heat exchanges; it may bring moister or drier air that will be governed by latent heat exchanges. The advection process relates to new volumes of air that are continuously brought over the ablation region for interactions with a volume of

the ice surface, and is measured by the AWS through wind speed and wind direction readings.

Humidity is the measure of water vapor content in the atmosphere and can be measured as absolute humidity, or specific humidity. The absolute humidity is defined as the mass of water vapor to a volume of air; specific humidity is defined as the mass of water vapor over the total mass of air (Ahrens, 2007). Automated weather stations in the ablation region measure the specific humidity and, as conditions warrant, will indicate the potential for evaporation, condensation, sublimation, or deposition.

Water is constantly passing between phases between the earth's surface and the atmosphere. If there are more phase changes to a vapor state than to a liquid, then there is net evaporation. If there are more phase changes to a liquid than to a vapor, there is net condensation. The dominant driver in these changes is the water temperature. Increasing water temperature gives more energy to the liquid water, and molecules can therefore escape more easily to vapor; a reduction in temperature will cause fewer molecules to phase change into vapor.

In the ablation region, there are also constant phase changes between snow/ice and vapor. If there are more net changes from snow/ice to vapor, sublimation occurs. If there are more changes from vapor to snow/ice, deposition results.

Snow and ice have unique boundary conditions for the energy balance that are quite different than other materials. Snow and ice appear more volumetric in the SW, whereas other surfaces have a planar surface boundary that merely absorbs or reflects shortwave radiation. This enables SW to be transmitted a certain distance into the snow and ice such that volume scattering takes place (Oke, 1987). The distance is determined

by Beer's Law: $F = F_0 e^{(-kx)}$, where F_0 is the initial intensity of radiation at a particular frequency, *x* is the distance into the volume, *k* is the absorption coefficient, and F is the resultant intensity at distance *x* (Randall, 2007). For practical purposes, for ice the SW can penetrate down to 10 meters, while for snow SW can penetrate to 1 meter (Oke, 1987).

Natural surfaces are at the most 5% reflective in the LW (Geiger et al., 2003); highly absorbent materials will consequently be a high emittance material in the LW. In the LW, snow and ice are near perfect black bodies, with radiated energy described by the Stefan-Boltzmann Law: $E = \varepsilon \cdot \sigma \cdot T^4$ (Oke, 1987), where ε is the emissivity of the body and σ is the Stefan-Boltzmann constant ($5.67 \cdot 10^{-8}$ W/m^{2}K^4). Ice has an emissivity of 0.96; snow has a high but variable emissivity between 0.82 and 0.99, depending on its age and density (Sellers, 1965). This means the snow and ice surfaces will both strongly absorb the re-emitted LW from the atmosphere, and radiate strongly in the LW, since both absorptivity and emissivity are large and reflectivity of LW small.

Sensible, Latent, and Ground Heat Transfers

The translation of energy between two volumes is related to many processes: the thermal conductivity of an object, the sensible and latent heat exchanges, and the conduction of energy. In general, sensible heat transfer is the warming or cooling of a volume (typically a parcel of air) by a process such that a measurable temperature change results. This will, by default, change the density of the air volume, which will physically rise or fall relative to its original position. Sensible heat will result in the atmospheric or turbulent mixing of air parcels within the atmosphere.

Latent heat exchange is defined as the phase change of water between its solid, liquid, or vapor forms. Each phase change carries with it an energy level that is either absorbed or released; the energy amount used is the same for either direction of phase change. The values for each phase change are given in Table 2.1 (Oke, 1987). These phase changes enable the storage and release of energy in the earth system; it is this change in stored energy that enables the earth to regulate its overall energy balance.

Table 2-1: Latent heat exchange values.

Latent heat for ice-liquid exchange	$0.34 \cdot 10^6$ J/kg at 0°C
Latent heat for vapor-liquid exchange	$2.50 \cdot 10^6$ J/kg at 0°C
Latent heat for ice-vapor exchange	$2.84 \cdot 10^6$ J/kg at 0°C

The snow melt process begins with heating at the surface by either the absorption of SW radiation, or by warm air masses passing overhead and enhancing the sensible heat flux towards the surface. Initially this added energy begins to raise the snow temperature both at the surface and internally due to volume scattering. In fact, it has been shown that the warmest part of the snow is below the surface, somewhere within the first 50cm (Oke, 1987). The snow begins to raise its temperature until it gets to 0°C, which is the melting point. As water forms from snow, both on the surface and below the surface, it then percolates deeper into the snowpack. It will then release heat as it re-freezes in the cooler interior of the snowpack. This brings heat deeper into the snow pack, helping to raise its overall temperature.

As this wave of temperature increase continues to move through the snowpack, the snow densifies from $\sim 0.2 g/cm^3$ beginning in the fall, to $\sim 0.4 g/cm^3$ in the late spring (Przybylak, 2003). Eventually the snow becomes firn reaching a density over $0.55 g/cm^3$

(USGS, 2009). This process both increases the size of the snow particles, and decreases the albedo.

The movement of heat will be from a higher concentration of energy to a lower concentration of energy, at a rate defined by the thermal diffusivity, κ. The diffusivity of air, water, and ice are: 20.5, 0.14, and $1.16 \cdot 10^{-6}$ m^2/s, respectively (Oke, 1987). This indicates the speed at which a temperature wave could propagate through a mass. In this case, water is the slowest to pass changes in temperature, air is the quickest, and ice maintains a middle position. If the snowmelt exceeds the sustainable percolation levels, the melt water will begin to run off, and create small ravines on the surface and supraglacial lakes at catchment points.

Water has a large heat capacity, C, which is equal to $4.18 \cdot 10^6$ $J/K \cdot m^3$ (Oke, 1987); this allows for water to be a very good storage medium of energy. The air in the atmosphere has a low heat capacity equal to $0.0012 \cdot 10^6$ $J/K \cdot m^3$ (Oke, 1987), which means air cannot store heat as well as water. The heat capacity of ice is in between at $1.93 \cdot 10^6$ $J/K \cdot m^3$ (Oke, 1987); which indicates it can store heat, but not to the extent of water. Equivocally, water or ice could be described as a body resistant to quick fluctuations of temperature change. They naturally dampen the atmospheric fluctuations brought to the local area via the advection processes. Warmer or cooler air masses can pass across the ablation region and enable evaporation, deposition, and condensation. On the short-term scale, the water's high heat capacity enables an extremely important storage component.

Melt

Heat will conduct downward into the ice cap as determined by the thermal diffusivity of ice. The vapor pressure will be higher in a warm atmosphere than the

surface vapor pressure; this gradient will enable the movement of water from the air to the surface via condensation. The condensation process will release even more heat (at 7.5 times the heat of fusion, or the heat required to melt ice), enabling even more melt. Therefore, any influx of humid, warmer air from the surrounding oceans will further enhance melt.

Radiative processes drive the local climate processes; van den Broeke recently illustrated this in his publication describing surface radiation analysis spanning four years (2003-2007) of the Kangerlussuaq transect (67° N) in the ablation zone (van den Broeke et al., 2008) at three sites: S5 (490m), S6 (1020m), and S9 (1520m). Site S5 is of comparable elevation to JAR2, and site S6 is comparable to JAR1. Monthly measured values of albedo, incoming (positive) SW, incoming (positive) and outgoing (negative) LW, surface temperature, and the temperature at 2m are shown in Fig. 2-4; note the melt season occurs during months 5, 6, 7, and 8. The bottom left panel shows the four-year average surface albedo changes from the highly reflective snow to the less reflective ice, then back to snow over the summer season. This process is what the dH Model is using for calculating the linear runoff.

The incoming LW and SW greatly increases during the melt season as seen in the top two panels of Fig. 2-4. For May, June, and July incoming radiation is above $\sim 220 W/m^2$ for all stations in both the LW and the SW; surface melt ensues. In August the LW continues to provide strong input (at least $\sim 270\ W/m^2$ at all locations), but the solar contribution begins to faulter (below $\sim 210\ W/m^2$) as the sun drops to the horizon. This data show the important contribution of incoming LW to the summer surface melt. The

bottom panel of Fig. 2-4 shows both the surface and 2m temperatures in September are at or below freezing as the surface begins the winter re-freeze at all stations.

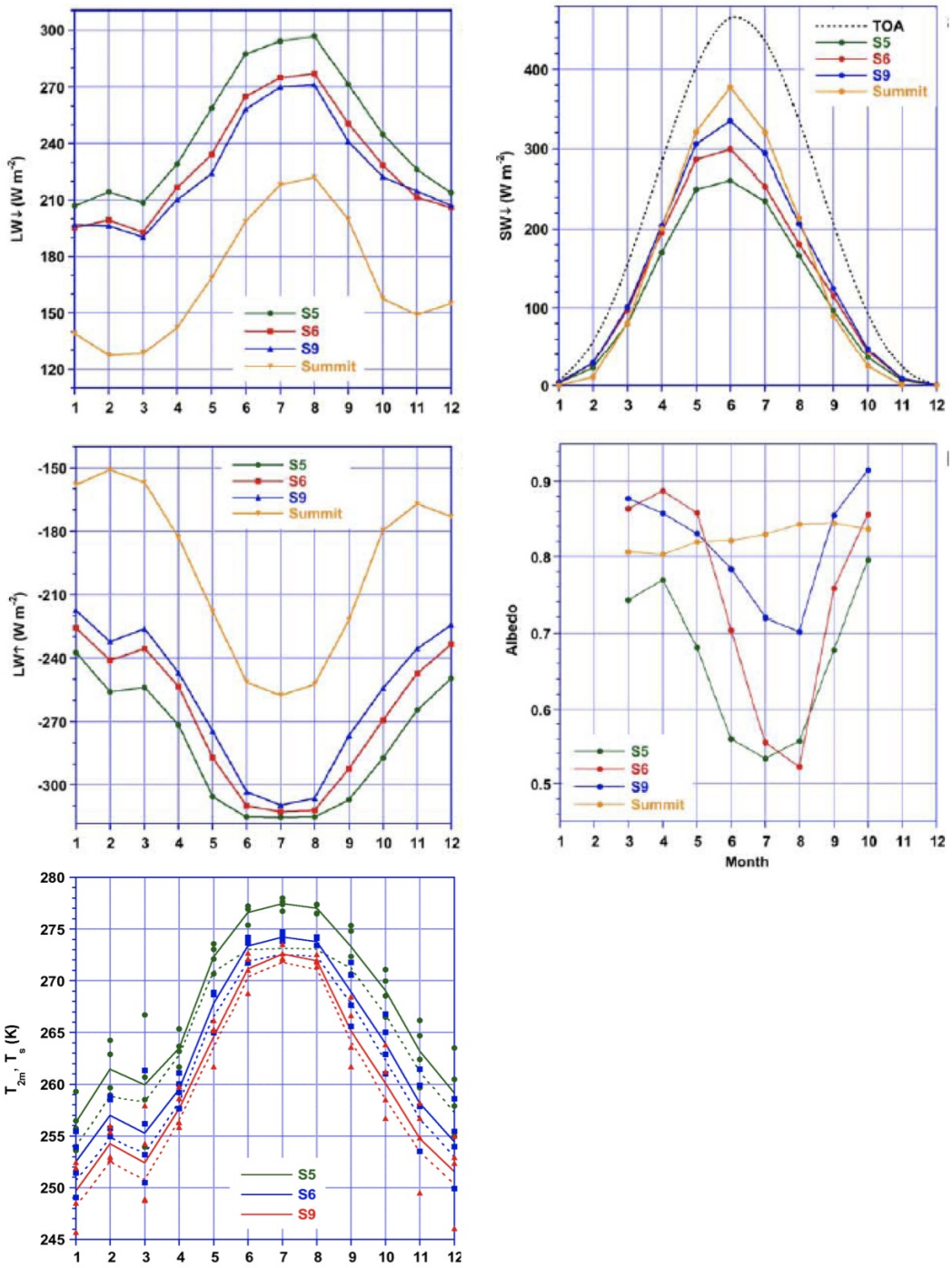

Fig. 2-4: 67° North LW, SW, albedo, surface, and 2m temperatures observed along the Kangerlussuaq transect at observation stations S5, S6, and S9 for 2003-2007. Temperature points are monthly averages for each year. (LW, SW, and albedo: van den Broeke et al., 2008; T (solid lines) and T_s (dotted lines): van den Broeke by personal correspondence).

Summer

The high albedo of snow and ice will reflect most of the incoming SW, but due to its magnitude, the SW that is not reflected enables the snow to begin melting. Increased cloud cover in the summer will bring more incoming LW that should increase melt, but it will also reduce the incoming SW (Van den Broeke et al., 2008). Therefore, the two processes tend to cancel each other in magnitude (Serreze and Barry, 2005).

The ablation region experiences a diurnal cycle as it melts in the late morning through the afternoon, and then refreezes in the evening hours. The snow is constantly emitting LW radiation throughout the 24-hour period, but during the day when the solar zenith angle is lower, there is enough supplement of SW energy to cause melting. Additionally, the air mass over the ablation region will usually have a higher temperature than the snow and ice. Hence surface energy flux will be positive, indicating more energy into the ice sheet, resulting in further melt, which will bring more heat into the ice pack.

The surface temperature should be 0°C during the melt phase; any additional energy to the system will result in continuing melt of deeper snow and ice. Therefore, the magnitude of outgoing LW will remain fixed since the surface temperature should not increase. Once the snow has melted, the less reflective ice is exposed. This will set up a positive feedback, as the lower albedo ice will then be able to absorb the incoming SW at a greater rate, thereby increasing melt.

The resultant melt water will percolate downward until it refreezes; then, any further melt will become runoff, thus establishing englacial or supraglacial streams and melt lakes on the surface of the ice. These lakes will grow in size over the summer, partly due to the lower albedo of water, and partly due to the accumulation of liquid over time.

Chapter Summary

The ablation zone is where most supraglacial melt lakes form; it is where there is more surface mass lost than is gained over the year. The driver for the entire Arctic system is solar input, which is zero in the winter and a maximum during the summer months. The three forms of water (liquid, ice, and vapor) change state to transfer energy between the atmosphere and the surface; the three forms of water can also act as storage mediums for energy. The ice surface absorbs energy from incoming SW and LW radiation during the summer, and re-radiates LW energy back to the atmosphere during the winter. During the summer, the transfer of heat directly into the ice sheet creates liquid water that can flow via riverine structures and collected to form supraglacial lakes. The next chapter presents the physical characteristics of the GIS, including a detailed discussion of the ice sheet's slope in the western region.

Chapter 3: Surveyed Area Characteristics

Geophysical Description of the Greenland Ice Sheet

This project calculates the volume of water present in supraglacial lakes in the Jakobshavn Isbrae region of the Greenland Ice Sheet (GIS), shown in Fig. 3-1. Greenland has the second largest ice mass on the earth, after the Antarctic continent. The ice sheet area is ~ 1.7 x 10^6km^2 (Chapter 4 of IPCC, 2007), or about the size of Alaska. Its average thickness is 1.6km, with a total volume of ice of ~3.0 x 10^6km^3, and could conceivably contribute to ~7.2m of sea level rise (Lubin and Massom, 2006).

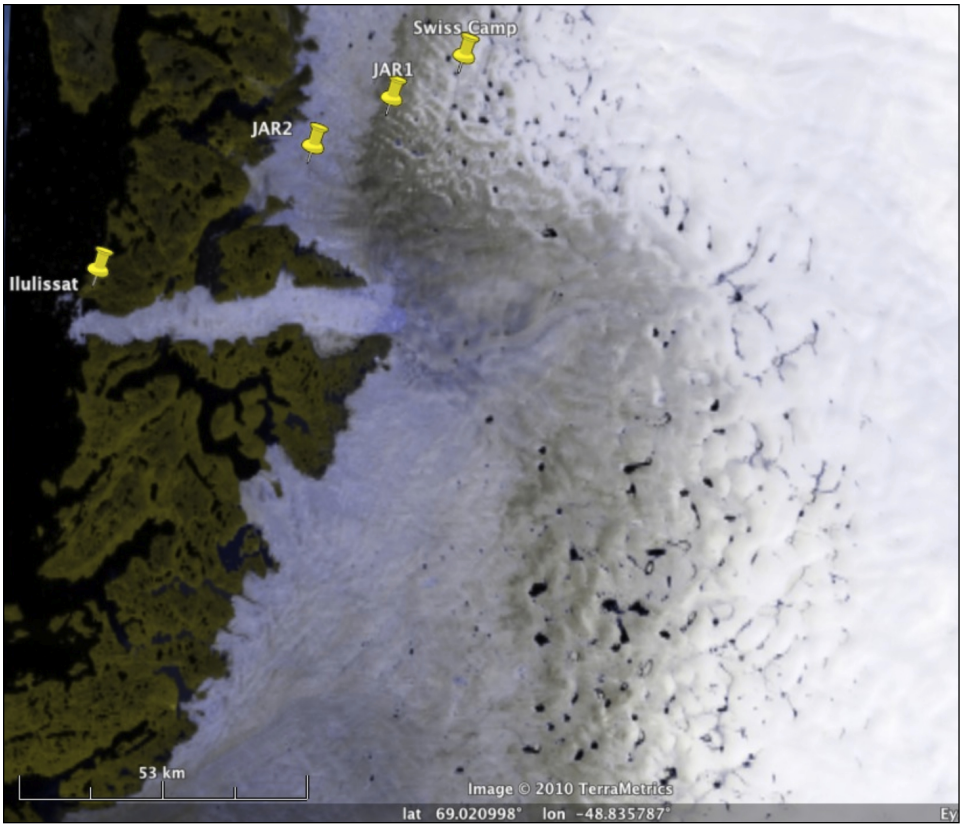

Fig. 3-1: The Jakobshavn study region near Ilulissat, Greenland.
(from NASA MODIS imagery, 17 Jul 2008 at 1440z)

Greenland is partially located in the path of atmospheric low-pressure systems, intercepting moisture from cyclonic activity (Steffen and Box, 2001) due to its high elevations, the highest point being Summit at 3203m (Cullen et al., 2006). Southeastern

Greenland has higher elevations than the southwestern portion as was shown in Fig. 1-4; therefore an eastern front's precipitation falls on the east flank, making the southwest region drier than the southeast region (Hanna et al., 2006). As Arctic air temperatures will likely increase over the next few decades, there will be an increase in atmospheric moisture content, with the potential for an increase of precipitation; indeed, some have observed this at elevations higher than 2000m (Hanna et al., 2008). Increased precipitation could be matched by an increase in runoff in the ablation region, if the precipitation makes it to the lower elevations. The runoff will likely collect in existing supraglacial lake areas, or create new supraglacial lakes at higher elevations since the atmospheric temperature will have increased.

Greenland's climate is quite different than the climate in Antarctica. On the GIS large areas experience considerable melt during the summer (Truffer and Fahnestock, 2007), whereas Antarctica experiences little summer melt. The western part of the GIS has a distinct zone consisting of surface crevasses and melt water retained in supraglacial lakes which store melt water runoff from locally melted snow and ice, or drainage from higher elevations. A supraglacial lake can drain extremely rapidly when there is a breach in the retention along the lake's side or at the bottom of the lake basin; some drain in time spans shorter than one day (Das et al., 2008). These breaches allow the entire water volume to drain via crevasses or moulins (Fig. 3-2), which could eventually reach the base of the ice sheet (Zwally et al., 2002).

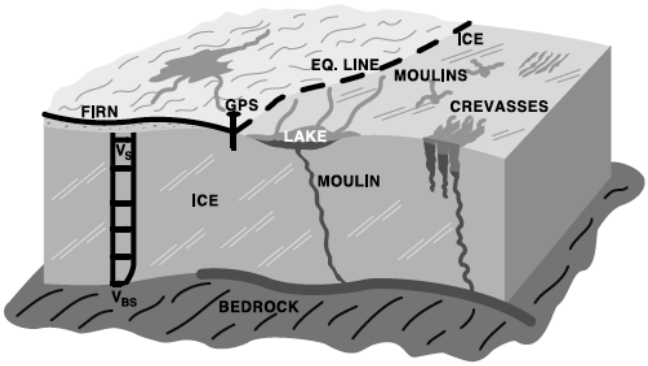

Fig. 3-2: Cut-away view of supraglacial lakes and crevasses contributing to basal water levels (Zwally et al., 2002).

From the high point of Summit, the GIS gently slopes towards the coastline, both eastward and westward, until it begins quickly dropping downward to the sea around the 1500m contour, as shown by the red line in Fig. 3-3. The Equilibrium Line Altitude (ELA) is the approximate elevation where annual accumulation equals ablation, resulting in no net surface elevation change. In the Jakobshavn region, Steffen and Box (2001) locate the ELA at 1150m, slightly different than the 1250m ELA estimate given by Fig. 2-2. Both estimates are lower than the 1500m elevation contour shown, and are very close to the coastline throughout Greenland.

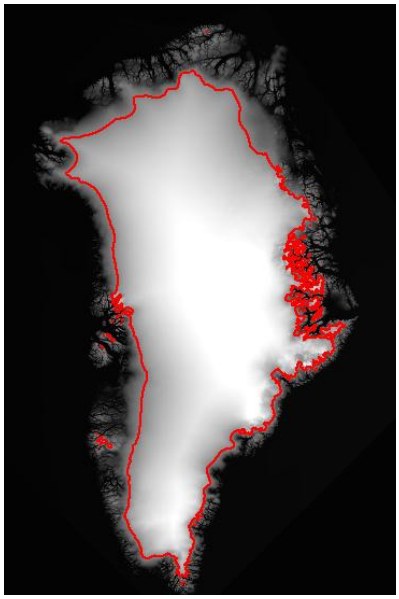

Fig. 3-3: The 1500m elevation contour line (in red) of the Greenland Ice Sheet.

Along the shore, the outlet glaciers can move between 200 and 1200m/yr (Joughlin et al., 2008), bringing large ice flows to the sea. In the ablation region, runoff water from the ice sheet, combined with the calving of icebergs of some of the world's fastest glaciers, contributes to global sea level rise. While runoff from the GIS has been calculated (Hanna et al., 2008), the percentage of melt water retained in the form of supraglacial lakes has not received the same attention.

One important component influencing surface runoff and supraglacial lake formation is the slope of the topography (Greuell, 2000). A transect of the GIS along the 68.73° N line of latitude from the western coast (50°W) inward to the east (44°W) is shown along the red line in Fig. 3-4. This transect was chosen because it bisects the area flown by the UAV (ladder patterns in yellow and purple), then continues upslope through the area that produces runoff. The highest point on the transect is at the eastern edge at 2366m, the lowest point is at the western edge at 693m.

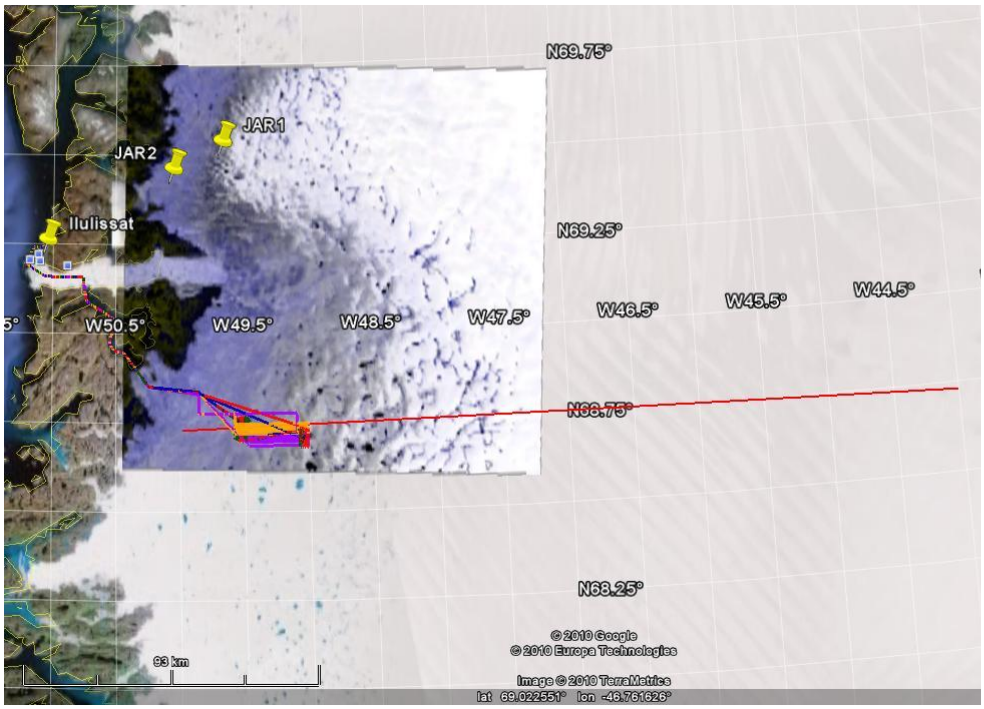

Fig. 3-4: The transect along 68.73°N analyzed for slope change.

Analyzing the 625m DEM reveals a noticeable slope change, as can be seen in Fig. 3-5. The slope decreases as elevation increases along the 68.73°N transect, extending from the western edge of the study region to the east, a distance of 290km.

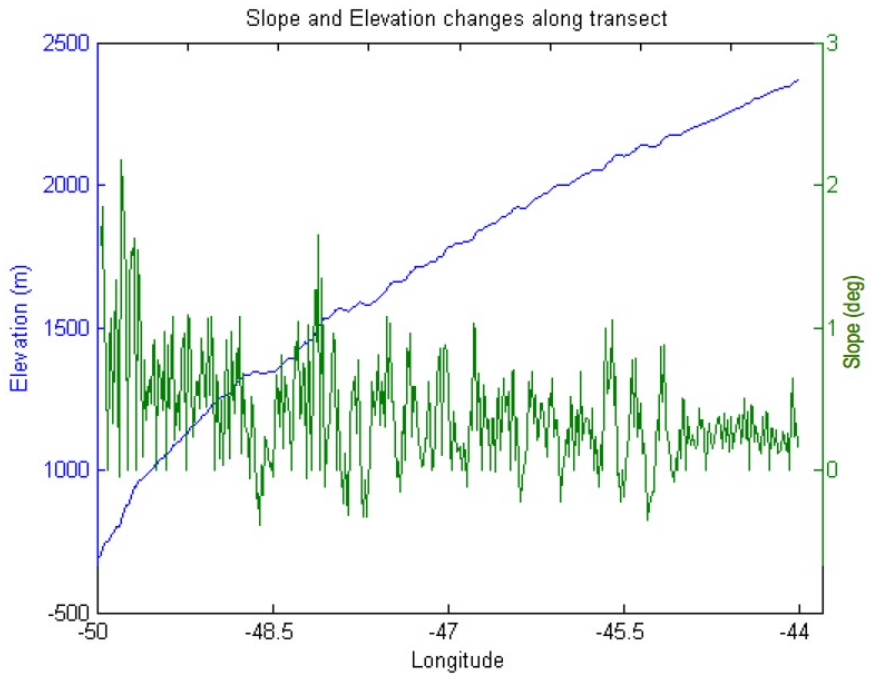

Fig. 3-5: Slope plotted with elevation along the 68.73°N transect. The slope (green) reduces eastward as elevation (blue) increases.

A three bin histogram depicting all slopes along the transect is shown in Fig. 3-6, where 65% of the points have a linear rise-over-run gradient less than 0.0082, 32% of the points have a rise-over-run gradient between 0.0082 and 0.0231, and only 3% of the points have a gradient above 0.00231. Table 3-1 converts these linear slopes to angular slopes for ease of understanding, and shows the mean elevation and slope of each bin. It can be seen the steeper slopes occur at the lower elevations, while the gentler slopes occur at higher elevations.

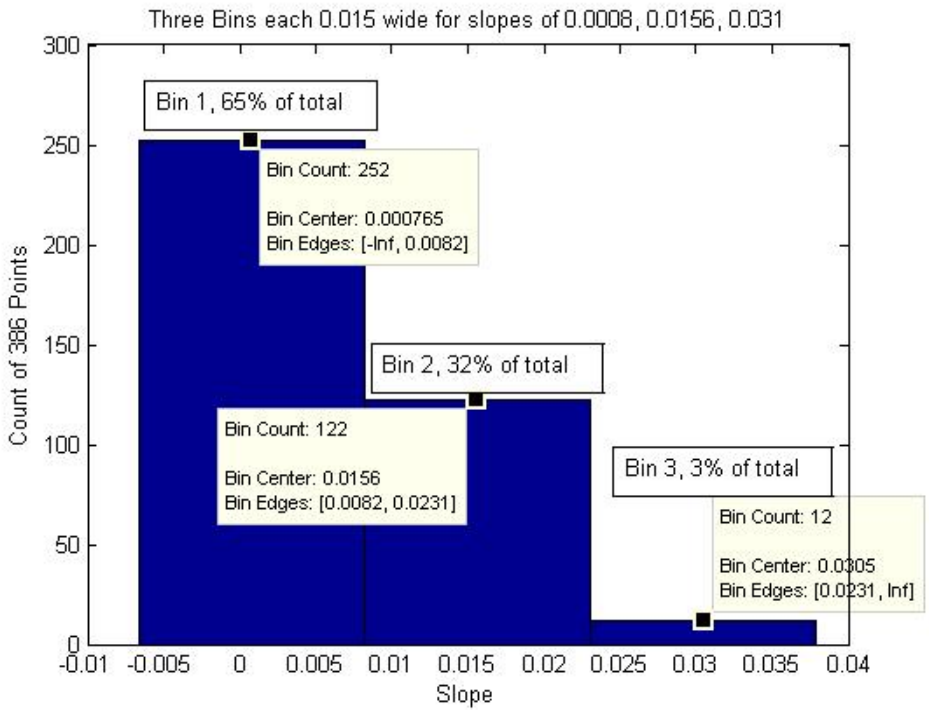

Fig. 3-6: Gradient histogram (rise/run) values along 68.73° North. Each bin is 0.015 wide, centering on 0.0008, 0.0156, and 0.031 rise/run elevation change values, moving from west to east.

Looking again at Fig. 3-5, the slope can be seen decreasing from nearly 1.0° at the coast, to a leveling value of ~0.2° inland. These results compare well with Steffen (1995) who indicates the ice sheet's slope above 1200m elevation to average 0.4°.

Table 3-1: Slope calculations along the 68.73° N transect categorized into 3 bins of varying slopes.

Slope Type	Rise/Run Average	Slope Average	Percentage of Bin points	Mean Elev (m) of each Bin
Shallower	0.0029	0.166°	65%	1845
Moderate	0.0130	0.745°	32%	1527
Steeper	0.0288	1.650°	3%	961

Chapter Summary

Greenland has a moist climate and experiences considerable surface melting during the summer months. From the middle of its plateau at Summit (3203m) the ice sheet gently slopes towards the coasts, where ice then funnels into outlet glaciers at a much steeper slope.

A transect along 68.73°N is analyzed between 50°W and 44°W and the changing slope is classified into three groups, with slopes observed at 0.17° at higher elevations (1845m), 0.75° at moderate elevations (1527m), and 1.65° at lower elevations (961m). If atmospheric warming continues, the shallower slopes at higher elevation, combined with increased melt, could produce supraglacial lakes in areas previously experiencing only refreezing into the snowpack.

Restating from the motivation portion of this study, if atmospheric warming continues, the shallower slopes of higher elevations combined with increased melt, could produce supraglacial lakes in areas previously experiencing only the refreezing of melt water within the snowpack.

In the next chapter, a description of the data types used in this study, and their sources, are presented in addition to the corrections that must be applied to these data.

Chapter 4: Data Types and Sources

Unmanned Flight Operations

The Arctic MUSCOX project was the first scientific use of an unmanned aerial vehicle (UAV) in Greenland; therefore, the mission profiles were kept to a conservative length, with the hope of adding more robust flight lines in following years.

The original project was operationally constrained to two pre-defined regions, as shown in Fig. 4-1, because of the uniqueness of operating a UAV over the ice sheet. Due to various operational issues, flights were only flown in the southern box (Mission A), which involved low-level transits over fjords, followed by a steep ascent into the area defined by the southern box.

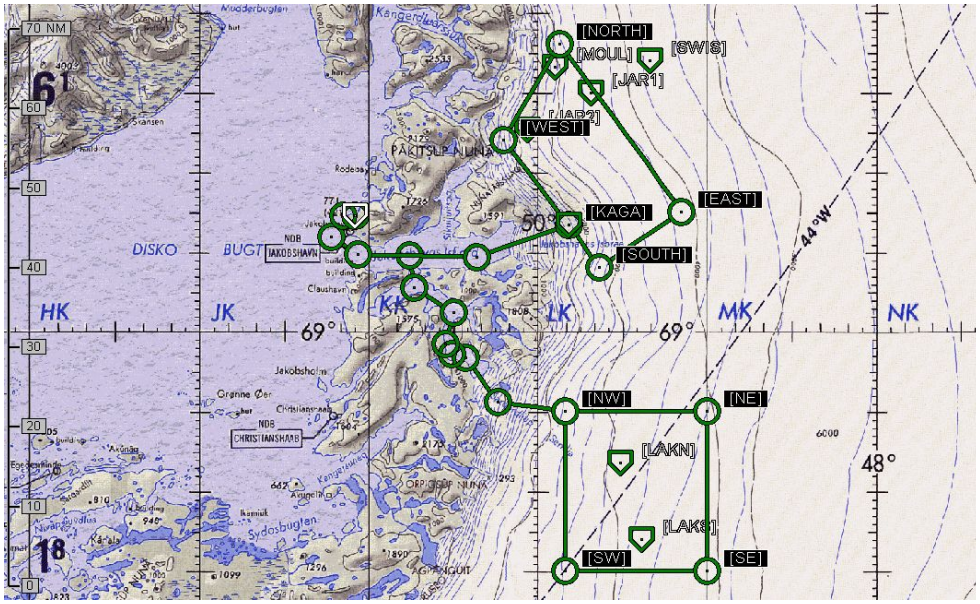

Fig. 4-1: Arctic MUSCOX UAV Operations in Ilulissat, July 2008.
Mission A (actually flown, bottom box indicated by NW, NE, SE & SW)
Mission B (not flown, top box indicated by North, West, South & East)

Between July 16 and July 23, 2008, five mission flights (J, K, L, M, and Q) were flown in the southern box. The tracks of all five UAV mission flights are shown in Fig. 4-2, along with each flight's takeoff date and time. The UAV's flight elevation ranged between the

airfield height of 29m (95 ft) to 1524m (5000 ft) along the eastern part of the southern box. Within this southern box Lakes 1, 2, and 3 were overflown; Lake 4 was to the east at a higher elevation. The aggregated flight tracks are shown in the upper left image of Fig. 4-2.

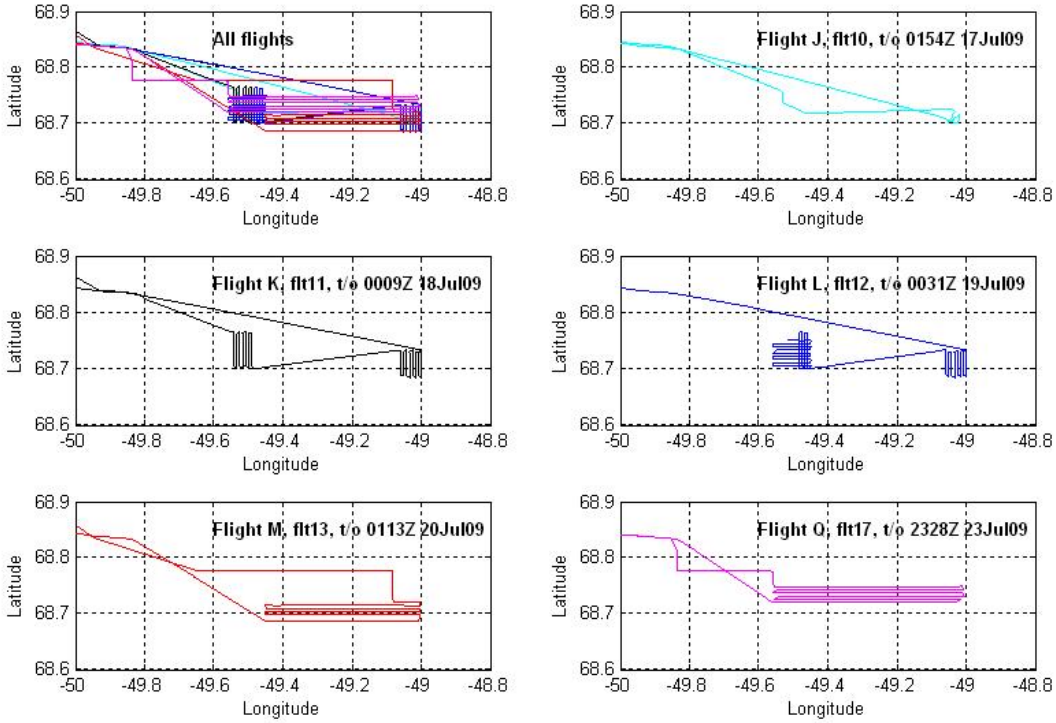

Fig. 4-2: Charts of each Arctic MUSCOX flight path, including date and take off time. An aggregate chart is shown in the upper left graphic.

There was considerable coordination between the Danish and Greenlandic governments to allow the UAV flights, where 17 flights occurred for ~33 total flight hours. Five of the flights were mission flights to the southern box; the other 12 were test and evaluation flights preceding the mission flights. The coordinates for the UAV flights to the southern box are shown in Table 4-1 in the degree/minute format (dd mm.mmm).

Table 4-1: Coordinates of the UAS flights into the study area.

Take Off, near JV/N	N69 14.485	W051 04.342
	N69 14.503	W051 08.690
	N69 11.793	W051 12.799
	N69 09.602	W051 03.418
	N69 09.522	W050 45.082
	N69 05.524	W050 43.466
	N69 02.329	W050 29.688
	N68 58.449	W050 32.631
	N68 57.151	W050 30.226
	N68 56.746	W050 25.432
	N68 51.144	W050 13.805
End transition (NW)	N68 50.000	W049 50.000

The coordinates of the southern box are shown in Table 4-2.

Table 4-2: Coordinates of the southern operational box.

Point Northwest	68° 50' N	049° 50' W
Point Northeast	68° 50' N	049° 00' W
Point Southeast	68° 30' N	049° 00' W
Point Southwest	68° 30' N	049° 50' W

Inside the approved southern box, the actual surveyed area during the missions was ~132km^2. The center of the actual operational area flown was 68.73°N, 49.28°W at an altitude of 1082m. The tracks were typically 22km in length in the east-west direction, and 6km long in the north-south direction. These dimensions were chosen to provide overlap with previous NASA ATM flight paths, ensure repeat coverage over melt lake areas, and maximize collection over the terrain changes within the approved southern box. Fig. 4-3 shows the area surveyed by NASA using the ATM lidar system (at 5km track spacing) with the UAV flight tracks (at 250m track spacing). Note the enhanced data set provided by the 250m flight line spacing of the Arctic MUSCOX project, which enabled the generation of a detailed 90m posting DEM.

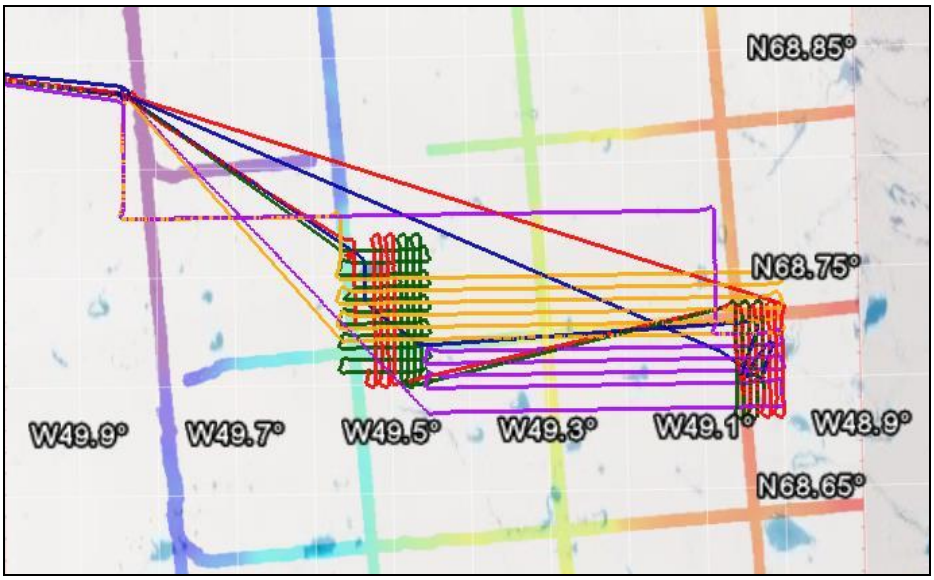

Fig. 4-3: All five UAV mission flights plotted (thin lines) with the ATM flight tracks in the background (thick lines). Note the gridded patterns over two sections. Although not visible, Lakes 1 and 2 are under the left grid pattern, and Lake 3 is under the right. The background image of the supraglacial lakes is a digital collage of unknown dates courtesy of Google Earth.

Lake 1 is of particular interest because in-situ measurements have been taken there during the summer seasons of 2006-2007 (Das et al., 2008). The Arctic MUSCOX Principal Investigator chose to fly grid patterns over this lake in July 2008 (toward the left of Fig. 4-3) so the in-flight lidar and imagery data could be correlated with the in-situ pressure sensor placed by the Das group at 68° 43.736'N, 049° 30.239'W. This sensor captured the rising supraglacial lake height and the lake drainage event on July 10 at 2040Z. From these flight tracks a high resolution DEM of the drained lakebed was created.

In-Situ Data

The Greenland Climate Network (GC-Net) typically provides 26 climate data variables throughout the entire year at each AWS site; for this study the temperature,

humidity, wind speed, wind direction, surface height, and incoming and reflected solar radiation are used. The AWS logs data at hourly intervals each day on an annual basis; the full explanation and architecture can be found in Steffen and Box (2001). GC-Net data from stations JAR1 and JAR2 between September 1, 2005 through August 31, 2008 were used in this study, providing three years of seasonal melt data, including the extreme melt year of 2007. While the melt season defined for this study is from May 13 - August 31 each year, the 2005 data were needed to initialize the energy balance model (SnowModel), which runs internally on an annual cycle. Additionally, it is noted that 2008 was a leap year, which required all algorithms to be modified to ensure the date values were congruent with 2006 and 2007.

Much time was needed to process the raw JAR1 and JAR2 GC-Net data to ensure the validity of the data, including extrapolating portions of the data to cover missing data periods. Specifically, the JAR1 tower fell over in July 2007, requiring data extrapolation through the end of the melt season. Additionally, while JAR2's 26 environmental variables were recorded correctly, the time and date logger did not increment for 3 months in 2007, requiring additional analysis to correct the date and time. Lastly, JAR2 did not record any data for the 2008 melt season, requiring the comparison of JAR2's two previous years' Melt Water Equivalent (MWE) routines with respect to JAR1 to determine the 2008 JAR2 runoff values. Descriptions of the data smoothing routines for the GC-Net data follow in Chapter 5. Each of the following sub-sections provides an overview of each data type, and the analysis done, before the final linear runoff and supraglacial lake volume analysis could be accomplished and presented.

Albedo and Density

Daily solar flux measurements made by the GC-Net stations include incoming and reflected shortwave radiation. The ratio of the reflected to the incoming shortwave gives the albedo of the surface. For JAR1 at 962m elevation, there is usually a thick layer of snow (~0.5m) on the surface in early May, which will have a high albedo (> 0.7). JAR2, at a lower elevation of 568m, does not typically have a thick snow layer and will not employ albedo as a discriminator between ice and snow.

During annual AWS tower servicing at JAR1, manual observations of the depth and density of snow are routinely taken each year. The May 11, 2008 JAR1 manual measurement of snow density was 358 kg/m^3, with a snow depth of 0.81 meters. Snow depth for JAR1 was manually observed in 2006 and 2007, but there were no manual snow density measurements at JAR1 for 2006 and 2007. We find the 2008 snow depth and density of the dH Model compares well with the observed values, as indicated in Table 4-3; within 15% and 04%, respectively.

Table 4-3: JAR1 snow depth and densities
observed and calculated at the beginning of the melt season.

	2006	2007	2008
Observed Snow Depth (m)	0.77	0.38	0.81
Calculated Snow Depth (m)	0.65	0.24	0.69
Calc Percentage (Calc/Obs)	84.4%	63.2%	85.2%
Observed Snow Density (kg/m^3)	not obs	not obs	358
Calculated Snow Density (kg/m^3)	320	381	373
Calc Percentage (Calc/Obs)	--	--	104.2%

JAR2 is almost half the elevation of JAR1, and has a different melt regime. The two stations are separated linearly by only ~18km, but the lower elevation and steeper slope of the ice sheet at JAR2 places it into a warmer temperature environment. However, due

to the two stations' proximity, it is assumed the daily incoming solar radiation and cloud obscuration rates are similar at each site.

MODIS

Three years of images from Band 1 and Band 2 of MODIS at 250m resolution were reviewed for each day of the melt season in 2006, 2007, and 2008. Of the 330 possible imagery days, 129 relatively cloud-free day images were chosen to be downloaded and used in this study from the NASA MODIS LAADS (Level 1 and Atmosphere Archive and Distribution System), located at: http://ladsweb.nascom.nasa.gov/data/search.html. The images were individually reviewed and cropped to slightly larger than the SnowModel study region size of 12,500km^2; the boundaries were 69° 45'N, 68° 35'N, 050° 25'W, and 47° 15'W as shown in Fig. 4-4. This created MODIS images of 16,475km^2, which were converted into matrixes of 504 rows by 523 columns for subsequent analysis using Matlab. The images were used to create a digital mask outlining the ice sheet from the land mass. This area was also used to calculate daily runoff over the entire Jakobshavn region.

A subset of 42 completely cloud-free images over the 13km x 91km inset strip shown by the red rectangle in Fig. 4-4 were cropped to provide data for volumetric analysis of the four supraglacial lakes. This inset strip completely overlaid the Arctic MUSCOX flight profiles, and allowed for calculations of melt water production that could drain into the study lakes, including upslope areas.

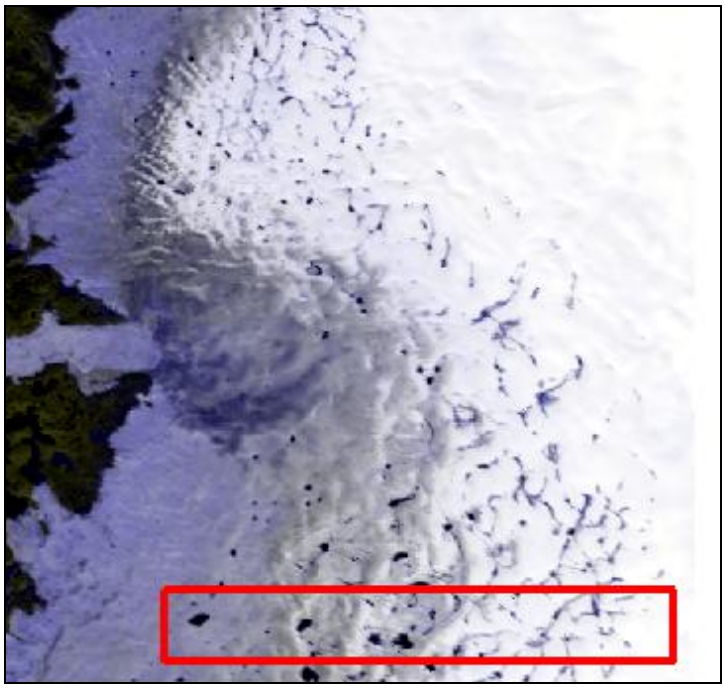

Fig. 4-4: The full Jakobshavn study region, with the inset strip highlighted. The inset strip was used to calculate daily runoff and supraglacial lake volumes (July 29th 2006 MODIS images).

Digital Elevation Models in the Region near the Jakobshavn Isbrae

The area of study is southeast of Ilulissat, Greenland in the ablation zone, as was shown in Fig. 1-2. Four DEM's were used in this study: two small scale, optically-based DEM's, and two large scale lidar-based DEM's. The DEM's are necessary to determine both the daily elevation-dependent runoff amounts, and the supraglacial lake volumes.

The two non-optically based DEM's used in the study originated from airborne laser altimeters. One lidar system was the NASA ATM, the other was the Universal Laser Sensor (ULS) from the University of Colorado Aeronautical Department and flown on the Arctic MUSCOX UAS. NASA's ATM is a conical scanning lidar that provides surface elevation information as a swath; the ULS is a profiling sounder that provides elevation information as a point.

The term DEM could be interpreted as a misnomer for the NASA project that has been monitoring the Greenland ice sheet using regular flight patterns since 1991 (Krabill et al., 2002). The flight tracks were widely spaced and designed to emphasize changing ice sheet elevations; there was no intent to create a DEM of Greenland due to lack of resources (time and money). The focus of the ATM flights was on the outlet glaciers and other areas of interest and not the entire ice sheet, revisiting the same flight track every few years to determine changes in elevation, and therefore mass (Krabill et al., 1995). However, the ATM elevations provide a reference for direct comparison with the UAV's ULS lidar. The term DEM will be used to describe the ATM data in this study, as many swaths were taken in the study area.

The first optically-based DEM was the image enhanced DEM of Greenland by Scambos and Haran (2002). This DEM is based on the 1km Greenland DEM (Bamber et al., 2001), but augmented with 44 Advanced Very High Resolution Radiometer (AVHRR) satellite images. Photoclinometry was used to improve elevation accuracy, and the horizontal resolution was increased to approximately 625m, from 1km, in both X and Y directions. While many areas showed increased accuracy due to this process, it is noted that over the gentle sloping interior ice sheet region, the accuracy actually decreased (Scambos and Haran, 2002), as validated by airborne laser altimetry profiles. However, as this study focuses on the ablation region, the Scambos and Haran DEM was chosen as the primary DEM for runoff calculations. The Scambos and Haran EASE-Grid North projection was obtained from the National Snow and Ice Data Center (NSIDC) Distributed Active Archive Center (DAAC) on June 30, 2009.

A second reason for using the Scambos and Haran DEM was its implementation by Mernild in the SnowModel energy balance computer simulations to generate runoff estimates for the years 2006, 2007, and 2008 (Mernild et al., 2010). It must be noted that the Scambos and Haran DEM was modified by Mernild et al., reposted to 500m resolution in both directions, presumably to make calculations easier. In this study the original Scambos and Haran DEM was also reposted to a 500m grid size so results were more easily compared between the calculated dH Model runoff and the simulated Mernild runoff calculations. These conversions also enabled the overlay of MODIS 250m images on the 500m Scambos and Haran DEM. In all cases, images and DEM's were converted into a UTM Zone 22N projection.

A second optically-based DEM was used for the lake volumetric analysis, because the newly released (June 29, 2009) ASTER Global DEM in an EASE-Grid North projection promised to have much better horizontal resolution, notionally at 30m by 30m. ASTER is a joint effort between NASA and Japan's Ministry of Economy Trade and Industry (METI); it provides 14 visible to thermal imaging bands with resolutions from 15m to 90m, including one reverse looking imager that provides the stereo imagery (http://asterweb.jpl.nasa.gov).

The spaceborne ASTER sensor has a 60km swath width, with one nadir pointing imager and one aft facing imager canted at an angle of ~28 degrees, both in the near-IR portion of the spectrum. The DEM's created over glacial regions have been shown to have an accuracy of +/-60m in mountainous regions, and +/-18m in moderately mountainous areas (Kaab, 2002). Using the two image sensors, a stereo image can be generated, and from this a DEM created.

After obtaining the ASTER global DEM dataset from the Land Processes DAAC (http://asterweb.jpl.nasa.gov/gdem-wist.asp), it was quickly apparent that the data had errors in the vertical dimension. Perhaps in non-ice sheet areas the ASTER elevation is more reliable, however it was found to be of varying quality at distances ~60km from the Greenlandic coastline. The lack of contrast on the ice sheet provides poor capacity for determining elevation data optically. Indeed, at the elevations of ~1800m where the ice sheet is sloping at a fairly shallow angle (see Fig. 1-4), the ASTER DEM was highly anomalous over an 11km distance with readings that vary from below –300m to above 3000m. Fig. 4-5 shows the middle of the ice sheet near the Jakobshavn region with the black contours indicating below sea level elevations.

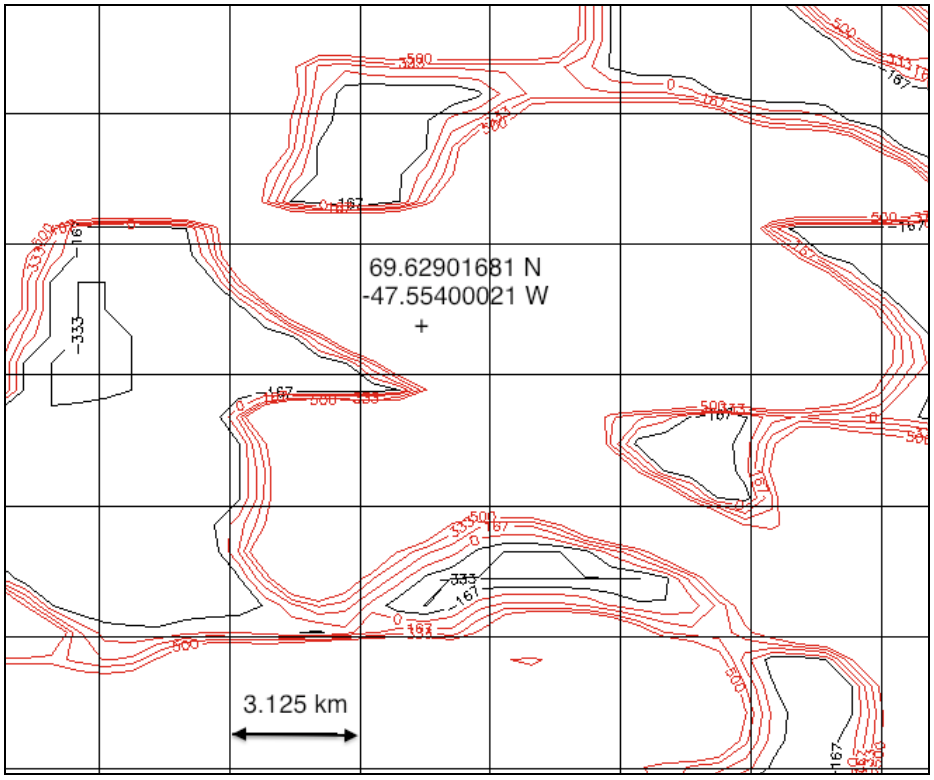

Fig. 4.5: Areas falsely indicating below sea level shown in black of the ASTER Global data in areas of 1800m elevation near the Jakobshavn region of the GIS.

Even after manually reducing and smoothing the ASTER posting size from 30m to 500m in the X and Y directions, the anomalous readings were still present. While the erroneous elevations were at the eastern edge of the study area, these errors provided a strong incentive to continue using the Scambos and Haran DEM for runoff calculations, which were already reposted to 500m without peaks or sinks in the elevation values.

In calculating volumes of supraglacial lakes, however, the lakes' relatively small size (10km^2 or less) preclude the use of the Scambos and Haran DEM. In one case, the calculation of water volume for Lake 4 in 2008 resulted in no volume, because the lake size of 0.31km^2 was smaller than the size of one DEM pixel; thus no elevation change was calculated and the volume was 0.0km^3. Therefore volume calculations required the use of the higher resolution ASTER DEM with some type of correction algorithm.

The volume of Lake 1 could be considered a known value by using the two previously mentioned techniques: the UAV lidar survey taken after Lake 1 drained, and by the in-situ pressure sensor. Therefore a volume calculated using the ASTER DEM could be corrected to this known volume, and the correction factor used for the other three lakes.

Lake 1's volume was calculated using ASTER and the masking technique outlined in Chapter 6, resulting in an ASTER estimated volume of 0.103km^3. Lake 1's volume was also calculated using a UAV lidar survey, described below, resulting in an estimate of 0.043km^3. Using the assumption that the ASTER elevation errors are fairly similar over the 13km by 91km inset strip study region while the lake's surface area remains the same in both the ASTER and lidar regimes, all ASTER volume estimates were modified using a

correction factor of 0.42 (0.043 km^3/0.103 km^3) to the ASTER derived lake depth calculations.

Utilizing Lapse Rate Extrapolations to Determine the Zero Runoff Elevation

Using lapse rates is a standard practice to predict temperature changes beyond the point of an actual in situ measurement.

Table 4-4 shows the monthly temperature lapse rates calculated for this region by Huff (2006). Averaging the lapse rates for July and August (the months with maximum observed monthly temperatures), a change of 5.0°C/1000m is calculated for elevations below 1150m; a change of 6.1°C/1000m is calculated for elevations between 1150m and 2000m, and a change of 5.0°C/1000m is calculated for elevations between 2000m and 3300m. This will place a limit on runoff at higher elevations, where the maximum average temperature is below 0°C.

Table 4-4: Temperature lapse rates upslope from JAR1 going to the East (Huff, 2006)

Month	Lapse Rate from 3300m to 2000m (°C / 1000m)	Lapse Rate from 2000m to 1150m (°C / 1000m)	Lapse Rate Below 1150m (°C / 1000m)
April	8.60	7.20	7.28
May	7.04	6.54	5.41
June	5.63	6.52	4.78
July	4.49	6.41	4.54
August	5.60	5.80	5.39
September	7.02	8.16	7.44
October	8.50	8.82	6.40

JAR1 is located at 962m, so two calculated lapse rates will be needed to determine the elevation where there is no runoff. Between 962m and 1150m, the lapse rate was calculated for 188m at a rate of 0.005°C/m, giving a temperature drop of 0.94°C. As stated

above, the known average maximum temperature is 4.3°C at JAR1, correcting to 1150m implies a maximum temperature of 3.36°C.

The highest daily averaged temperatures at JAR1 were 4.8°C, 4.7°C, and 3.3°C on Aug 15, 2006; July 11, 2007; and July 5, 2008; respectively. Averaging these maximum temperatures over the three years gives 4.3°C for a representative maximum average summer day at JAR1 over the study period. Using lapse rates and converting this temperature to a higher elevation should give the maximum elevation where runoff could be expected, and an upper limit on supraglacial lake formation. This elevation is described as the "zero runoff elevation."

To find the 0°C elevation, the lapse rate of 0.0061°C/m is employed over 3.36°C yielding an elevation change of 551m. Therefore a DEM mask for no runoff was created at 551m + 1150m = 1701m, or ~1700m. Of note, Sundal et al. (2009) also used 1700m for their elevation limit when calculating supraglacial lake areas. They described 1700m as the upper limit for supraglacial lake formations in the southwestern GIS. A zero runoff elevation of 1700m will be used for all runoff calculations from 2006 to 2008; future projections of the zero runoff elevation changes will be presented in Chapter 5.

Using a DEM to Program the UAV

To program the autonomous UAV's to fly above the ablation region, apriori knowledge of elevation data is required to ensure enough altitude is maintained for safety of flight, while ensuring the UAV is low enough to detect returned lidar pulses. The 625m Scambos and Haran DEM from NSIDC was consulted to program safe flight passage. The first flight was deliberately programmed to fly between 300m to 500m over the ice sheet surface elevation. Comparing the observed lidar returns to the expected ice

elevation values showed adequate terrain coverage and no loss of return lidar signal, hence confidence was built for programming the following flights at various altitudes. The resultant flights yielded raw ice surface height data, which after various corrections detailed below, yielded the ice surface height.

The laser range finder deployed on the UAV internally averages 10 consecutive pulse returns to produce one laser range data sample which is stored in ASCII format in the onboard Gumstix computer. These data were analyzed using Matlab, and outliers (any returns equal to zero or greater than 2500m) were removed. The resulting number of data points is the equivalent of one laser shot every 6.25cm (calculated at a nominal aircraft flight velocity of 25m/sec). The resulting laser elevation profile is shown in Fig. 4-6. The maximum ice sheet elevation detected by the UAV's lidar system throughout the study region was 1241m on the eastern edge of Flight Q, while the minimum elevation was 884m detected during Flight J as it exited to the west.

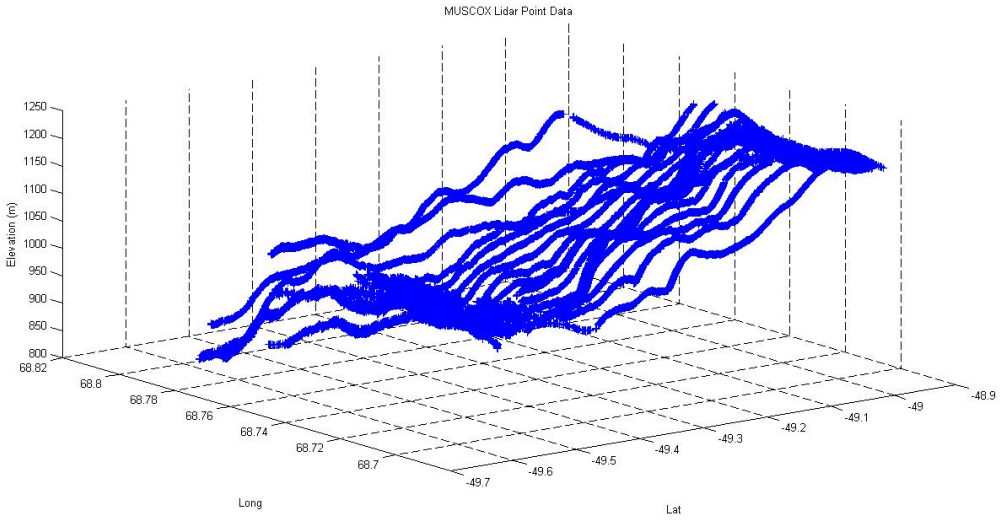

Fig. 4-6: Laser height profiles showing the sloping terrain of the supraglacial lake study area.

Corrections and Calibrations to Airborne Lidar Data

The raw data collected by the UAV included: accelerations, roll, pitch, yaw, binary GPS differential data, IR surface temperature, meteorological data, pressure, laser range, time, and other pertinent information. Ian Crocker, a fellow Ph.D. student from the Aeronautical Engineering Department and team member of Arctic MUSCOX, converted all raw data into usable Matlab matrixes. Working together, the ground station GPS files, in addition to the UAV GPS files, were processed to produce a corrected UAV platform position.

The first correction was post-processing the UAV's raw GPS positional data using the Novatel Waypoint 8.10 software package as shown in Fig. 4-7.

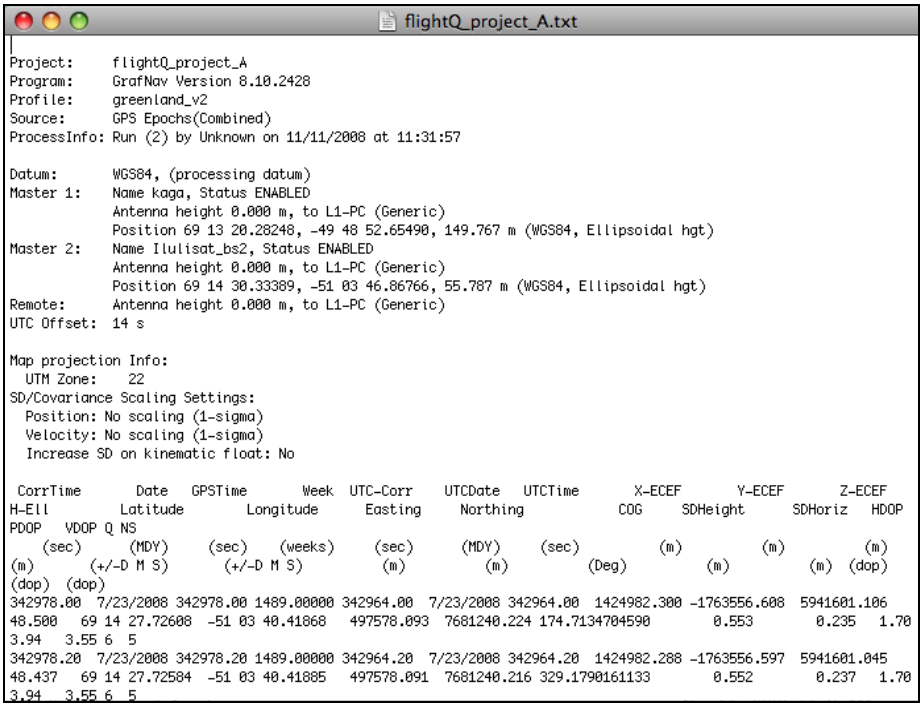
flightQ_project_A.txt

```
Project:     flightQ_project_A
Program:     GrafNav Version 8.10.2428
Profile:     greenland_v2
Source:      GPS Epochs(Combined)
ProcessInfo: Run (2) by Unknown on 11/11/2008 at 11:31:57

Datum:       WGS84, (processing datum)
Master 1:    Name kaga, Status ENABLED
             Antenna height 0.000 m, to L1-PC (Generic)
             Position 69 13 20.28248, -49 48 52.65490, 149.767 m (WGS84, Ellipsoidal hgt)
Master 2:    Name Ilulisat_bs2, Status ENABLED
             Antenna height 0.000 m, to L1-PC (Generic)
             Position 69 14 30.33389, -51 03 46.86766, 55.787 m (WGS84, Ellipsoidal hgt)
Remote:      Antenna height 0.000 m, to L1-PC (Generic)
UTC Offset:  14 s

Map projection Info:
  UTM Zone:    22
SD/Covariance Scaling Settings:
  Position: No scaling (1-sigma)
  Velocity: No scaling (1-sigma)
  Increase SD on kinematic float: No

 CorrTime       Date   GPSTime       Week  UTC-Corr    UTCDate   UTCTime       X-ECEF       Y-ECEF       Z-ECEF
H-Ell         Latitude        Longitude      Easting     Northing            COG     SDHeight      SDHoriz   HDOP
PDOP   VDOP Q NS
    (sec)      (MDY)     (sec)    (weeks)     (sec)      (MDY)     (sec)          (m)          (m)          (m)
(m)       (+/-D M S)       (+/-D M S)          (m)          (m)          (Deg)          (m)          (m)  (dop)
(dop)  (dop)
342978.00  7/23/2008 342978.00 1489.00000 342964.00  7/23/2008 342964.00  1424982.300 -1763556.608  5941601.106
48.500   69 14 27.72608  -51 03 40.41868   497578.093  7681240.224 174.7134704590        0.553        0.235   1.70
3.94   3.55 6  5
342978.20  7/23/2008 342978.20 1489.00000 342964.20  7/23/2008 342964.20  1424982.288 -1763556.597  5941601.045
48.437   69 14 27.72584  -51 03 40.41885   497578.091  7681240.216 329.1790161133        0.552        0.237   1.70
3.94   3.55 6  5
```

Fig. 4-7: A typical post-processed log from Waypoint.

The post-processing corrects for ionospheric errors, satellite vehicle problems, UAV antenna orientation issues, and other general signal degradation factors. Post-processing used two ground reference stations: one permanent station (KAGA),

maintained by the University NAVSTAR Consortium (UNAVCO); and one local reference station set up and calibrated at the Ilulissat airfield by the Arctic MUSCOX team. The final corrected product near the airfield placed the UAV to within 10cm in the vertical, and well under 10cm in the horizontal. However, due to the flight area's geometry with respect to the two ground stations, the cumulative errors in three dimensions out near the four supraglacial lakes of interest could be as high as 5m, as shown in Fig. 4-8.

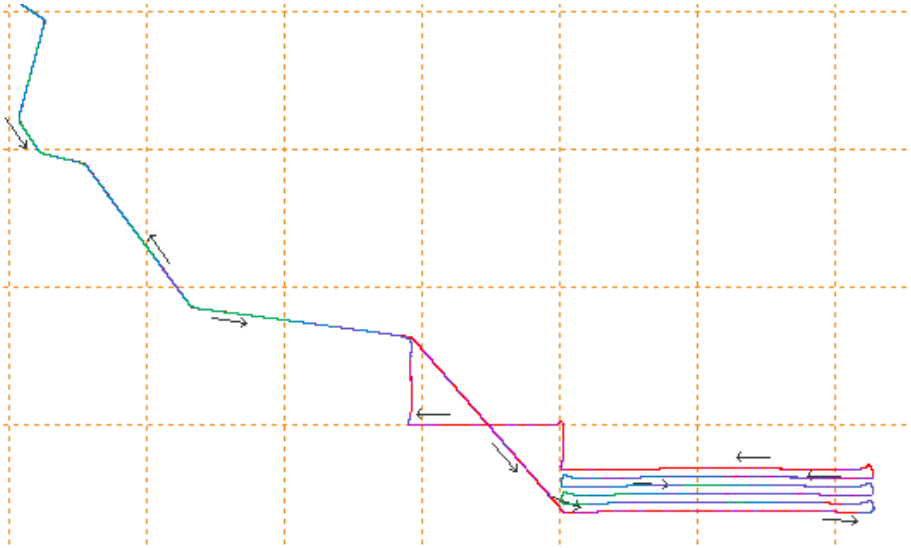

Fig. 4-8: Flight Q after post-processing of the raw GPS signal data. The greens and blues indicate locations with higher accuracy, while the orange and red tones indicate reduced accuracies. Each grid cell is 10km by 10km, north is page up.

The exact breakdown of the error colors is shown in Table 4-5 with the quality of the GPS signals shown using a color scheme. In consultation with the Waypoint Software vendor, these are spherical errors; meaning differences could be in any direction.

Table 4-5: Error color bar chart for post-processed GPS positions in three dimensions, using the Waypoint software.

Color	3-D Error (m)
Green	0.00 – 0.15
Cyan	0.05 – 0.40
Blue	0.20 – 1.00
Purple	0.50 – 2.00
Magenta	1.00 – 5.00
Red	2.00 10.00

The Manta UAV naturally adjusts its course, altitude, and orientation throughout the flight to ensure it remains on its pre-determined course. These movements are all conducted autonomously using an autopilot and logged by the Gumstix computer as roll, pitch, and yaw (RPY) data coming from three-axis gyros and accelerometers. The RPY data were analyzed for biases and angular outlier data; a threshold of +/- 3 degrees was set for roll, and +2 to +8 degrees was set for the pitch (the plane flies with a 5° pitch up attitude). Yaw data did not require additional filtering. All turn-point data were also filtered at the end of each track; this filter ensured all range data were truly nadir and not off-axis shots, which would produce an erroneous DEM as shown in Fig 4-9.

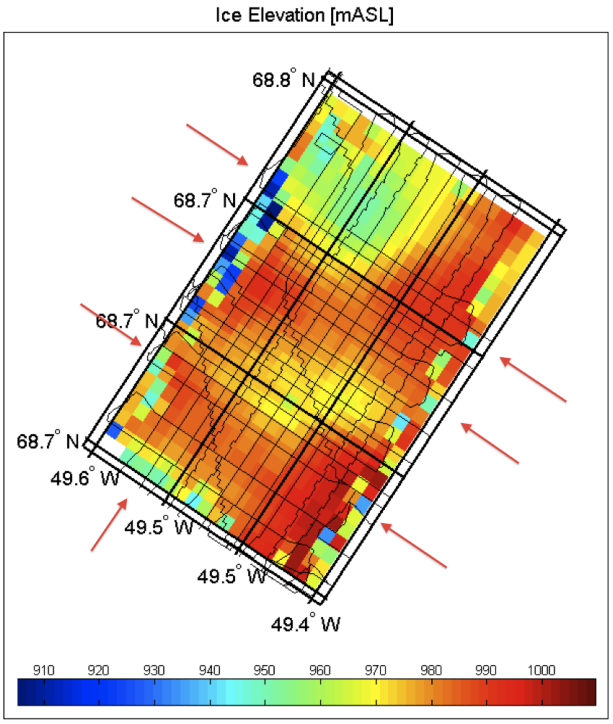

Fig. 4-9: Initial DEM in meters generated from the Arctic MUSCOX lidar without RPY corrections for the turns made by the UAV. Note all the "deeper" measurements at the turn-points, some indicated by the red arrows.

The resulting set of X, Y points that contained corrected airborne platform data is shown in Fig. 4-10, and became what is called a data 'cloud', and is not registered in space or time. Using Matlab, the 'cloud' was smoothed in time to allow for registration between the various data sets collected during the missions: imagery, video, and altimetry data. In the event there were missing data, an average value between the two nearest valid data points would be calculated and stored.

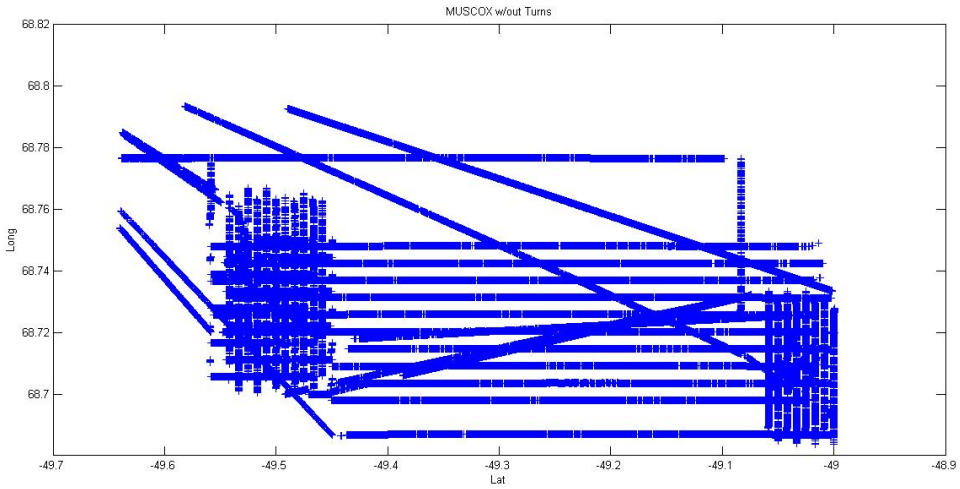

Fig. 4-10: All flight tracks post-processed with turn data removed.

Spatially, the time-smoothed data series could now have subtle offsets in either latitude or longitude due to winds blowing the UAV slightly off course, or other factors. The temporally corrected data were then gridded in both latitude and longitude directions to enable spatial corrections. The final gridded data set was now ready for analysis. The National Geospatial Intelligence Agency distance calculator was used to determine the length of one meter at the survey region's central point of latitude and longitude. One degree of latitude is 111,545m; one degree of longitude is 40,501m (http://www.nga.mil/

MSISiteContent/StaticFiles/Calculators/degree.html). The aggregated data sets for each of the five flights was placed into one file, and re-posted as a 90m by 90m grid pattern over the entire flight region. The resulting DEM spanning the area of Lakes 1, 2, and 3 is viewable in 3-D using the Matlab software, as shown in Fig. 4-11.

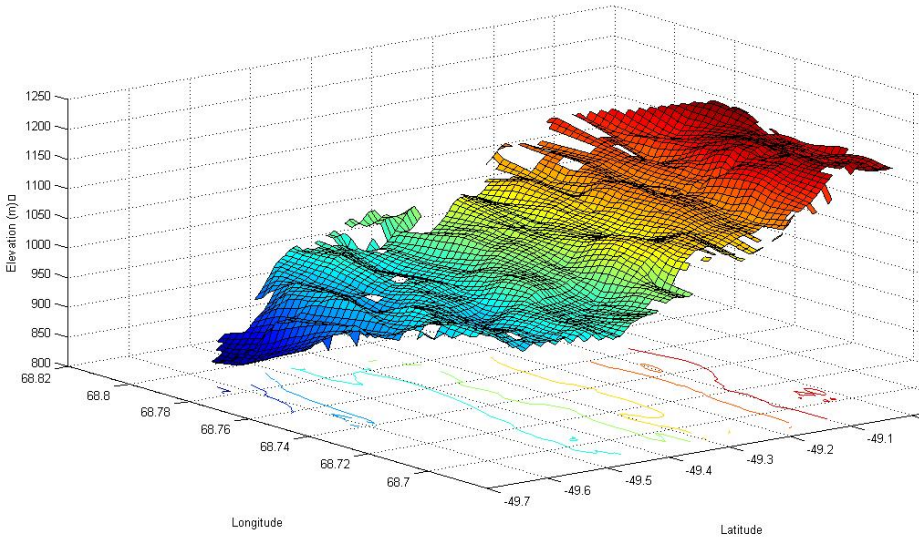

Fig. 4-11: The ablation region high resolution 90m DEM showing actual supraglacial lake depressions, and potential supraglacial lake locations.

NASA ATM Elevation Information

The NASA ATM laser profiling system has had many repeat track observations over the Jakobshavn region. It is a conical scanning system, as shown in Fig. 4-12, that produces enormous data sets which need to be reduced and concatenated before comparing to the Arctic MUSCOX lidar profiling system. As the manned aircraft flies along its track, the NASA ATM scans in a circular mode; the result is overlapping lidar returns that appear as ovals.

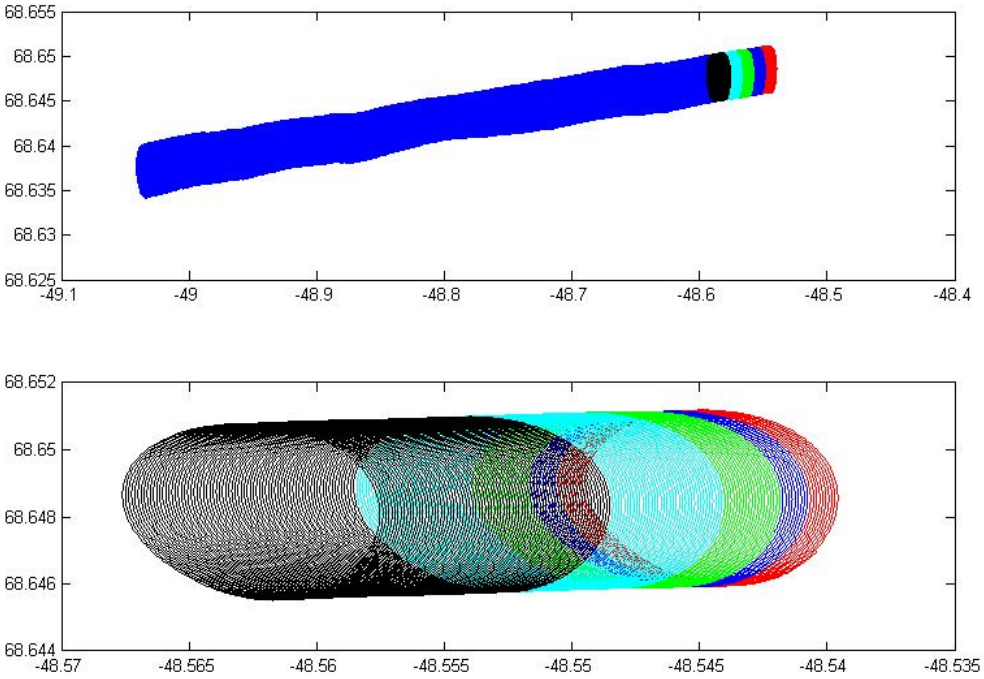

Fig. 4-12: NASA ATM scanning laser profiler before data reduction. Top image shows an east-west track, bottom image is a zoomed-in detail plot of the far eastern section. The colors add a visual 3D effect for ease of understanding the conical scanning mechanism of the ATM.

The data from the June and July 2008 ATM flights were used in comparison with the high resolution point measurement laser transects taken during the Arctic MUSCOX 2008 campaign. The wider ATM swaths were reduced to a narrower point path, as shown in Fig. 4-13. The ATM and UAV lidar returns could then be analyzed together.

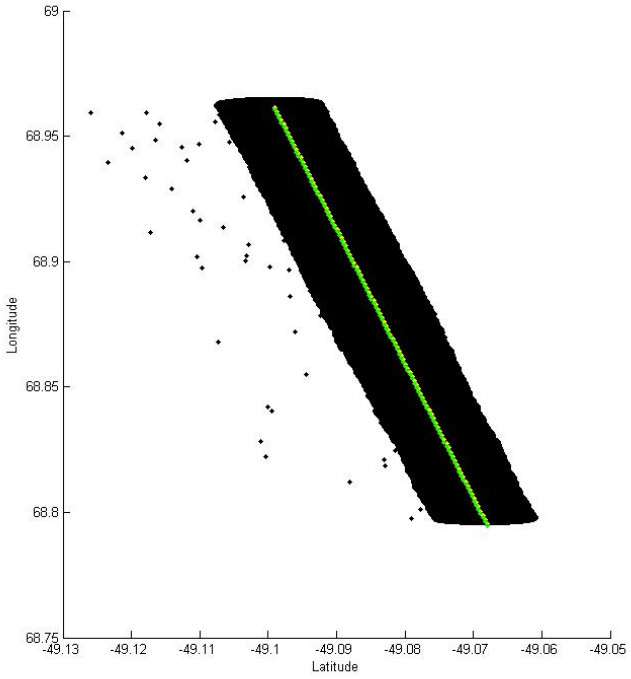

Fig. 4-13: NASA ATM Scanning laser profiler after data reduction. A single (green) path length inside the conical scanning track of the original ATM data (black).

The results showed errors of up to 4m between the ATM range data and the MUSCOX range data as shown in Fig. 4-14. The errors were both in the positive and negative 'z' directions, indicating no general bias. All errors are under the 5m maximum error reported by the ground processing software and are not attributable to a single source. This comparison does give strong confidence in the unmanned system overall, as the small craft can produce a DEM within the tolerances imposed by the GPS processing software. Future testing using properly oriented ground stations would enable a more robust error analysis; for this study the UAV-derived elevations will be used to directly calculate the actual volume of Lake 1.

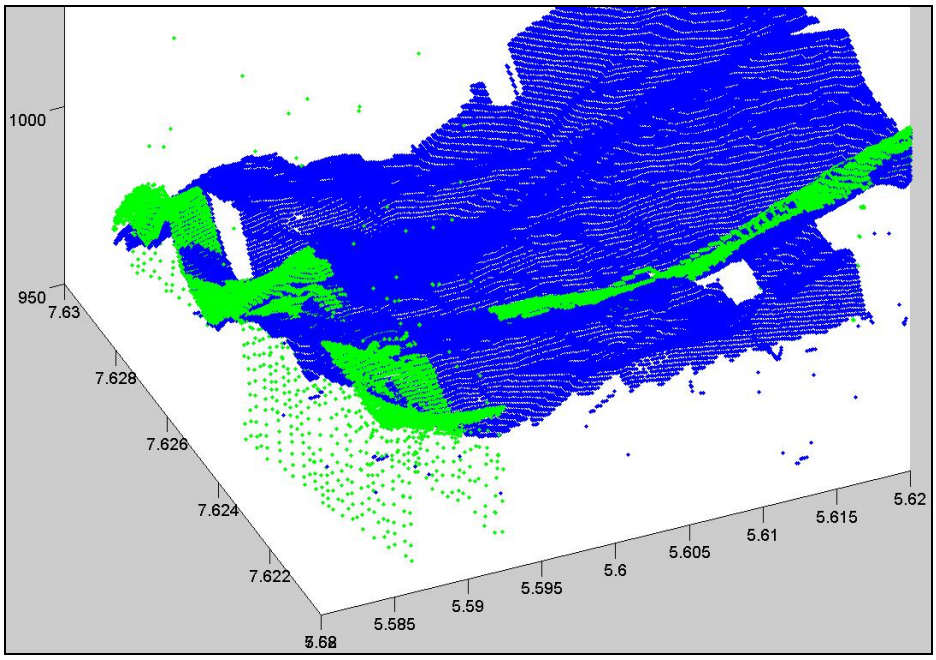

Fig. 4-14: Overlay of the ATM flight track (green) on the MUSCOX DEM (blue). The x- and y- axes are UTM 22N coordinates; the z-axis is in meters.

All five UAV flights were flown within two weeks of the Lake 1's drainage event. It is assumed in the creation of this DEM that the ice did not change its elevation profile, and the five sets of lidar returns are measuring the same ice surface. Therefore the aggregated points of all five flights will produce the high resolution DEM.

Chapter Summary

The first civil unmanned flight operations in Greenland were carried out in the summer of 2008 by the Arctic MUSCOX project team. A high resolution DEM was created from an airborne lidar survey over a recently drained supraglacial lake, providing accurate volume information at 90m postings. Ground processing was required for both the reference station and onboard GPS data.

In-situ measurements from the GC-Net were obtained over the three-year study period, 2006-2008, indicating the actual surface height changes and meteorological data

at two automated weather station locations. The AWS data drove two runoff models, an energy balance model (SnowModel) and a surface height change model (dH Model). After comparing modeled runoff output to measured readings at the AWS sites, the dH Model was chosen to determine runoff for the region.

MODIS imagery was used to determine areal lake sizing throughout the summer; a corrected ASTER Global DEM was employed to calculate four supraglacial lake volumes along an inset strip.

Temperature lapse rate and runoff data from previous studies were used to calculate the elevation where runoff is not expected to occur. In the next chapter, algorithms are presented for determining the ablation zone's total surface runoff, as well as future projections of the zero runoff elevation line (as a function of increased atmospheric temperature).

Chapter 5: Melt Water Runoff Calculations and Future Positions of the Zero Runoff Elevation

Overview

Surface melt water which forms runoff can collect in local catchment areas to form supraglacial lakes. The calculation of how much water is stored in these lakes is described below using in-situ surface height change measurements, then converted to a melt water equivalent for the snow/ice and adjusted for different elevations using a linear transformation model. After accounting for sublimation, a linear runoff height is computed in meters. The linear runoff (m) can be multiplied by the area of each pixel (m^2) to get the true runoff (m^3 or km^3) of the Jakobshavn Isbrae and its surrounding region.

Earlier, Chapter 4 described the present 1700m elevation limit for supraglacial lake formation. If the Arctic atmosphere warms by a few degrees over the next several decades, it is expected that more supraglacial lakes will form on the GIS, including higher elevations. This chapter outlines the process of calculating these parameters in and around the Jakobshavn region.

Snow and Ice Density

The density of snow and ice vary dramatically, ~70 kg/m^3 to ~150 kg/m^3 for very fresh snow, ~480 kg/m^3 for old snow, and ~910 kg/m^3 for ice (Oke, 1987; American Meteorological Society, 2009). Once the snow or ice has melted, the density of the water increases; at 4°C it is 1,000 kg/m^3 (Oke, 1987). Therefore, in order to accurately determine the calculation of melt water equivalent (MWE) of snow or ice, it is important to know the type and density of the melting surface.

Measurements at the GC-Net AWS do not include snow grain size, a key determinate in snow density (Warren, 1982); therefore an alternate snow density method using the available observations was developed. Since surface albedo can be calculated using the incoming and reflected SW, it was determined to use albedo as an indicator of surface type and density. Albedo ranges previously mentioned of 0.7 to 0.9 for snow surfaces, and 0.3 to 0.5 for ice structures is well accepted. It is also logical to believe there is not a discontinuity in density between these two ranges of albedo, as snow transitions into ice. Therefore Table 5-1 was created as a best estimate for the translation between the domains of albedo and density; it is a useful tool in the calculations of MWE.

Table 5-1: Albedo-Density lookup table used in Matlab routines.

Albedo	**Density (kg/m^3)**	**Albedo**	**Density (kg/m^3)**
1.000	50.0	0.675	425.0
0.975	87.5	0.650	450.0
0.950	125.0	0.625	475.0
0.925	162.0	0.600	500.0
0.900	200.0	0.575	600.0
0.875	225.0	0.550	700.0
0.850	250.0	0.525	800.0
0.825	275.0	0.500	900.0
0.800	300.0	0.475	902.5
0.775	325.0	0.450	905.0
0.750	350.0	0.425	907.5
0.725	375.0	0.400	910.0
0.700	400.0	<.400	910.0

The dH Model's algorithm calculates JAR1's snow density daily based upon reflected SW, before calculating the total melt water equivalent. When the measured albedo at JAR1 dropped below 0.60, it is assumed all snow has melted, leaving firn and ice available for melt. The dates for each year's occurrence of an albedo less than 0.60 are:

July 21, 2006; June 21, 2007; and June 26, 2008. Note the order of appearance of surface ice by year at JAR1 is 2007, then 2008, and finally 2006 towards the end of July; likely due to temperature changes unique to each melt season.

This study's algorithms began each year on May 13th and continued through the melt season until August 31st. Comparing the dH Model output with observed values at JAR1 in 2008, we see the modeled snow depth was 0.69m vs. the observed depth of 0.81m; the calculated snow density was 373kg/m^3 vs. an observed density of 358kg/m^3 (Table 5-2). The calculated density was within 4% of the observed measurement, while the snow depth routine was within 15% of the measured value. There were no density measurements for 2006 or 2007.

Table 5-2: Observed and calculated JAR1 snow depth and density.

	2006	2007	2008
Observed snow height (m)	0.77	0.38	0.81
Observed snow density (kg/m^3)	-	-	358
Calculated snow height (m)	0.59	0.24	0.69
Calculated density (kg/m^3)	320	381	373

Runoff

As snow melts, the melted water trickles into the snowpack, where it can refreeze in the firn or snow, or begin to runoff. Once the snow melts completely, the melted water becomes runoff that follows the topography downslope via crevassed riverine structures. The runoff can also enter into the ice sheet directly via moulins, deep well-like structures that enable water to penetrate internally to the ice sheet as shown in Fig. 5-1. After the snow at the surface of the ice sheet melts, the lower albedo ice remains, which will also

begin to melt. Therefore, by tracking albedo changes, one can tell when there is snow or ice on the surface, and apply the proper density to infer MWE.

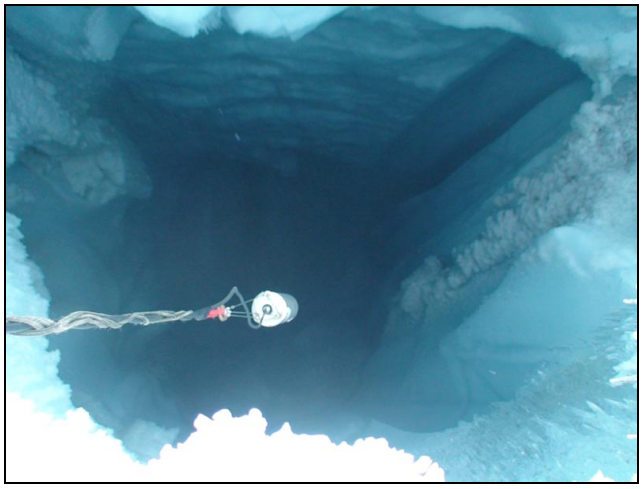

Fig. 5-1: A moulin near JAR1 with a camera and lidar system being lowering to the bottom (courtesy of NASA/JPL).

The conversion to MWE is done using the formula given by the National Snow and Ice Data Center (NSIDC) for Snow Water Equivalent (SWE):

$$\text{SWE (m)} = \text{depth (m)} \times \text{density (kg/m}^3\text{)} \,/\, \text{density of water (kg/m}^3\text{)} \quad \text{Eq. 1}$$

where depth and density are for the snowpack in question, and the density of water is at the assumed local temperature near 0°C. The CRC Handbook states water density at 273.4K (~0°C) to be 999.84kg/m^3 (CRC, 2008).

Sublimation

Sublimation values for the local study region were taken from Box and Steffen (2001), which reported average monthly sublimation values over a five-year period for many of the GC-Net sites, including JAR1 and JAR2 (Table 5-3).

Table 5-3: Monthly latent heat fluxes for sublimation throughout Greenland from 1995-2000 (Box and Steffen, 2001), edited for brevity.

Site	W m^{-2}	Jan.	Feb.	Mar.	Apr.	May	June	July	Aug.	Sept.	Oct.	Nov.	Dec.	Net, mm	Year
Swiss Camp	mean	0.5	-1.6	4.1	0.5	15.5	17.0	7.7	7.7	6.9	0.5	7.3	9.0	-74	1997
	sd	7.4	2.0	5.4	10.4	20.5	13.2	10.5	9.8	8.8	5.2	11.3	13.7		
							⋮								
JAR1	mean	11.6	3.1	10.1	4.3	10.4	5.0	1.6	4.0	5.6	4.8	14.3	11.1	-82	1997
	sd	29.9	8.3	19.0	9.2	10.5	5.7	3.0	6.7	12.3	10.2	25.3	23.1		
JAR1	mean	15.5	2.1	3.5	16.7	8.7	5.3	4.5	1.0	9.1	3.1	11.2	10.1	-87	1998
	sd	30.1	6.9	6.9	21.5	10.5	5.7	9.2	6.5	13.1	10.7	18.6	18.2		
							⋮								
JAR2	mean	1.7	1.5	1.5	4.1	3.4	23.0	3.2	6.8	7.3	4.3	1.4	3.2	-61	1999.8-2000.7
	sd	4.7	6.8	6.4	10.4	8.3	21.4	5.7	9.3	12.3	8.7	6.7	8.7		

The May/June/July/August (MJJA) monthly latent heat values for the two JAR1 observed years were averaged together to produce single monthly MJJA latent heat values for JAR1. These latent heat values were then converted to monthly mm of sublimation using the calculations described by Box and Steffen (2001); the monthly mm of sublimation were then converted to daily mm of sublimation for use in the daily dH Model.

JAR1's total melt season's sublimation was 19.6mm. For reference, the annual one and two level profile method calculations (1LM and 2LM, respectively) of sublimation in mm are shown for each AWS site in Table 5-4 (Box and Steffen, 2001).

Table 5-4: Net annual sublimation amounts in mm of water equivalent, for 1995-2000 based on all available data (Box and Steffen, 2001).

Site	1LM (mm w e yr^{-1})	2LM (mm w e yr^{-1})
Swiss Camp	-89 ±36	-64 ±20
CP1	-48 ±19	-60 ±19
NASA-U	-35 ±14	-29 ±9
GITS	-29 ±12	-59 ±18
Humboldt	-18 ±7	5 ±2
Summit	-10 ±4	18 ±6
Tunu-N	-21 ±8	28 ±9
DYE-2	-63 ±25	-186 ±58
JAR1	-138 ±55	-114 ±35
Saddle	-28 ±11	-31 ±10
South Dome	-35 ±14	*
NASA-E	-16 ±6	5 ±2
CP2	-75 ±30	38 ±12
NGRIP	-8 ±3	8 ±2
NASA-SE	-30 ±12	9 ±3
JAR2	-166 ±66	-50 ±16

Using the values in Table 5-3, the latent fluxes for the months MJJA were summed and compared between JAR1 and JAR2, giving 20.25 W/m^2 and 36.4 W/m^2, respectively. Due to the extremely large standard deviation found in the JAR2 flux measurement for June (23 +/- 21.4 W/m^2), the ratio of JAR2/JAR1 of 1.8 was used to calculate the JAR2 sublimation rate in mm/day from the JAR1 mm/day rate. See Table 5-5 for the daily sublimation values used in this study.

Table 5-5: Sublimation rates at JAR1 and JAR2 in mm/day for the months of May, June, July and August.

	JAR1 (mm/day)	JAR2 (mm/day)
May	0.2905	0.5229
June	0.1619	0.2914
July	0.0928	0.1670
August	0.0760	0.1369

The resulting daily sublimation rates were subtracted from the daily observed surface height change values, as sublimation will not contribute to runoff. The resulting surface height changes were then aggregated throughout the melt season, giving a cumulative total of the linear runoff.

Positive Degree Days

The Positive Degree Day (PDD) is a convenient number to understand melt over a seasonal period. Zwally et al. (2002) define the PDD as the sum of hourly averaged temperatures above 0°C, divided by 24. For instance, two hours of +5°C taken at the 2m level would yield a PDD of (5+5)/24= 0.42. The PDD could also be thought of as the portion of a day when the temperature was above freezing, with each additional daily averaged degree increase of temperature over zero being counted as another degree day. The year 2007 had a much higher number of degree days than either 2006 or 2008 as shown in Table 5-6. The rank order of JAR1's total PPD's (from high to low) is 2007, 2008, and 2006; this is the same order of appearance of the ice sheet after the surface snow had melted (discussed previously in the Snow and Ice Density section).

Table 5-6: JAR1 Positive Degree Days.

Year	JAR1 PDD's
2006	108.9
2007	149.7
2008	118.0

Melt Water Equivalent (MWE) Corrections and Runoff Calculations

Since no observational measurements of surface height changes were recorded at JAR2 in 2008, a reasonable approach must be taken to generate surrogate data for the MWE. Using PDD's at JAR1 for the previous two years, we can infer the 2008 MWE at

JAR2. For JAR1 we know the 2008 number of PDD's is much closer to 2006 than 2007 as shown in Table 5-6; Table 5-2 shows the 2008 snow depth was more similar to 2006 than 2007. JAR1 experienced an increase of 40.8 PDD's in 2007, and only 9.1 PDD's in 2008, as compared to 2006. The ratio of MWE increase between JAR1 and JAR2 was 1.167 for 2006, and 1.450 for 2007. A linear fit of $f(x) = 0.0069x + 0.41$ is found for PDD vs. MWE, resulting in a ratio of 1.22 to increase the 2008 MWE from JAR1 in applying to JAR2. The increase is applied to the daily 2008 JAR2 calculations of MWE.

The end of each melt season's summary data for the point locations of JAR1 and JAR2 are presented in Table 5-7 for total observed surface height loss, observed density, snow depth, dH Model calculated runoff, and simulated runoff from the SnowModel system.

Table 5-7: Summary data for JAR1 and JAR2, observed and calculated.

	2006	2007	2008
JAR1 at 962m			
Observed (snow + ice) (m)	2.10	2.39	2.48
Observed snow height (m)	0.77	0.38	0.81
Observed snow density (kg/m^3)	-	-	358
dH Calculated snow height (m)	0.59	0.24	0.69
dH Calculated density (kg/m^3)	320	381	373
dH Calculated Runoff (m)	1.79	1.99	1.96
Simulated Runoff (m)	0.95	1.09	0.85
JAR2 at 568m			
Observed (snow + ice) (m)	2.18	2.59	2.63
dH Calculated Runoff (m)	2.11	2.86	2.40
Simulated Runoff (m)	2.11	2.93	2.37

An earlier study by Reeh (1991) near the Jakobshavn region documented linear runoff as shown in Fig. 5-2; to get the total runoff one needs to multiply the linear runoff

by the surface area of concern. Of note, the x-axis shows surface runoff as a negative number, in this study surface runoff is indicated as a positive number. Reeh's negative numbers will be converted to positive numbers for comparisons.

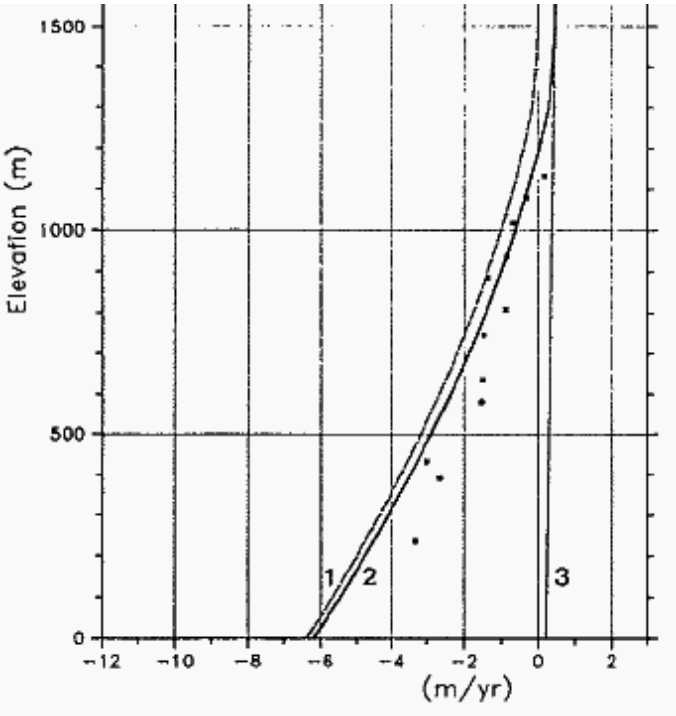

Fig. 5-2: The annual point runoff (x-axis) by elevation (y-axis) for locations in the ablation region of Greenland near 69° 30' N. Observations (dots) and calculated annual runoff (Line 1) developed by Reeh, 1991. Accumulation is indicated by line 3, to the right of the origin.

Reeh observed and calculated linear runoff based upon elevation, at 69° 30' N. The graph shows a calculated runoff rate (line 1) and observed values (dots) between -1m/yr to -5m/yr (1m/yr to 5m/yr) in the elevation range of the study region. It is noted in Fig. 5-2 the 1991 observed and calculated runoff values disappear above 1340 meters elevation, forming the zero runoff elevation.

Future years could have a positive gain in the zero runoff elevation due to increased atmospheric temperatures. The NASA Goddard Institute for Space Studies

(GISS) provides many global surface temperature products, including decadal temperature trends over three-month intervals. Looking at the June, July, and August anomalies from the base years of 1951-1980 (NASA GISS, 2010), it is found that Jakobshavn region experienced ~1°C increase in average temperature since the 1990's. Using the lapse rate of 0.0061°C/m for elevations between 1150m and 2000m from Chapter 4, an elevation change of +164m is calculated, resulting in an expected zero runoff elevation to be at 1504m (based Fig. 5-2). This study uses 1700m (calculated in Chapter 4) for the limit of zero runoff and supraglacial lake formation between 2006 and 2008.

The dH Model's calculations of linear runoff for 2006-2008 are higher for JAR1 and JAR2 than the 1991 predicted linear runoff values (taken from Fig. 5-2). JAR2's calculated linear runoff is very close, or slightly lower than the predicted values, and are tabulated in Table 5-8. This comparison also gives confidence of the dH Model output for linear runoff determination.

Table 5-8: Calculated annual runoff and Reeh's predicted runoff.

Runoff (m)	JAR1 @ 962m	JAR2 @ 568m
2006	1.54	2.31
2007	1.93	2.95
2008	1.72	2.59
Reeh Prediction	1.30	2.90

Future Changes to the Zero Runoff Elevation

To calculate future scenarios for supraglacial lake formations, an assumption was made to analyze sequential increments of atmospheric temperatures by half-degree increments. This forced an expanded regional area of analysis because increased temperatures would bring warmth to higher ice sheet elevations, which encloses more of

the ice sheet towards the summit. A new snow and ice reference area is extended eastward to 44°W. The new area is 28,399 km^2, and its linear extension eastward from Lake 4 is ~150km.

The Fourth Assessment Report from the IPCC (IPCC 2007) has six future atmospheric temperature projections based on SRES (Special Report on Emissions Scenarios). The six are known as the A1B, A1F1, A1T, A2, B1, and B2 scenarios. They indicate a range of future surface temperature changes, from +1.8°C to +4.0°C between the years of 2090 to 2099 as determined by 1) a simple climate model, 2) several Earth Models of Intermediate Complexity (EMICs), and 3) a large number of Atmosphere-Ocean Global Circulation Models (AOGCMs). Averaging these six temperature range scenarios, one could reasonably assume an increase of +2.8°C by 2099.

Using projected temperature increases of 0.5°C increments over the GIS near Jakobshavn; calculations can be made to show where melt, runoff, and supraglacial lake formation could occur above the current observed limit of 1700m. Calculating the increased zero runoff elevation using the 0.0061°C/m lapse rate from Chapter 4 for temperature change scenarios between 1150m and 2000m, and using 0.005°C/m for elevations above 2000m, the new expected limits of supraglacial lake formation can be determined, as shown in Table 5-9.

Table 5-9: The new zero runoff elevations due to increased atmospheric temperatures.

Additional Temperature (°C)	Additional Zero Elevation Height (m) above 1700m	Maximum Zero Runoff Elevation (m)
0.5	83	1783
1.0	165	1865
1.5	247	1947
2.0	335	2035
2.5	435	2135
3.0	535	2235

This large potential increase in area of supraglacial lake formation, and supraglacial lakes' subsequent drainage patterns, could considerably change the ice sheet's response to seasonal patterns. A decreased surface albedo, coupled with larger amounts of liquid water present on the ice sheet's surface, will have impacts that are currently unknown. Aggregating the areal extent of these new potential lake formations, it can be seen a very large area could be affected as shown in Table 5-10. For a 3°C temperature increase, the potential new lake formation area is expanded by 12,297km^2, and increase of 43.3% over the base reference area.

Table 5-10: Increased area of potential supraglacial lake formations as a function of 0.5°C incremental increases of average atmospheric temperature. The increases are shown both incrementally and cumulatively by percentages over the 28,399 km^2 snow and ice reference area.

Incrementally increased Temperature °C	Incremental Increase in Area (km^2)	Incremental increase in area of potential supraglacial lake locations	Cumulative increase in area of potential supraglacial lake locations
0.5	1,424	5.0%	5.0%
1.0	1,643	5.8%	10.8%
1.5	1,945	6.8%	17.6%
2.0	2,129	7.5%	25.1%
2.5	2,478	8.7%	33.9%
3.0	2,677	9.4%	43.3%

Figure 5-3 is a MODIS image from July 29th, 2006 showing how the zero runoff elevation would extend over the new larger reference area under a +0.5°C to a +3.0°C increase in atmospheric temperatures.

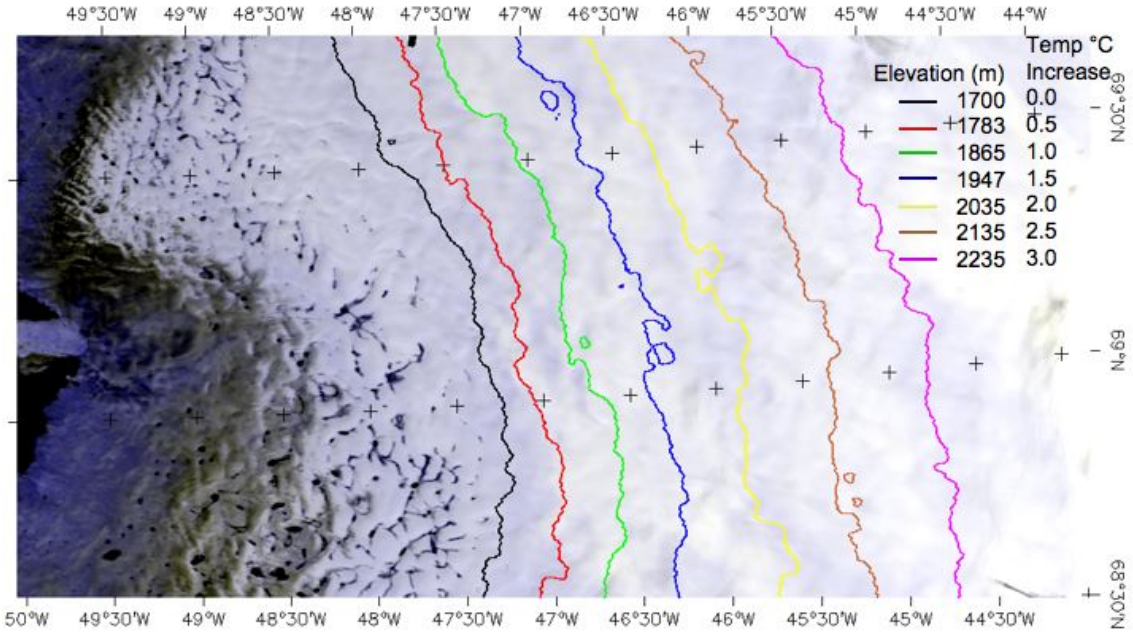

Fig. 5-3: Potential future elevation expansion of supraglacial lakes due to increases in the average atmospheric temperature and the flattening of the ice sheet.

Chapter Summary

Matlab code was developed to combine various data sources to calculate daily runoff estimates and lake volume information for the four study lakes in the Jakobshavn region. A snow and ice density algorithm was developed based on reflected SW radiation. Further calculations of surface height changes were translated into MWE. Sublimation corrections were then made using charts from previous studies. The PDD concept was discussed, and used only for comparison with runoff calculations. The next chapter presents the final fusing of the various data sources, and displays the results of the study.

Chapter 6: The Synthesis of In-Situ and Remotely Sensed Data near the Jakobshavn Isbrae

Overview

This chapter describes the synthesis of data from overhead satellite imagery, UAS lidar information, and in-situ readings from the AWS; components fused together to describe the areal size and volume of supraglacial lakes, and the runoff of the surrounding region near the Jakobshavn Isbrae.

Lidar Returns from an Unmanned Aerial Vehicle

The processed return laser signals from the UAV's Flight M are shown in Fig. 6-1, a typical mission flight profile. Actual ice sheet elevation in meters is shown on the y-axis, and mission time in hours is displayed on the x-axis. From left to right the figure portrays the UAV flight up the fjord towards the 1227m high point of the survey area, then two round trip legs (downslope and upslope) before returning to Ilulissat.

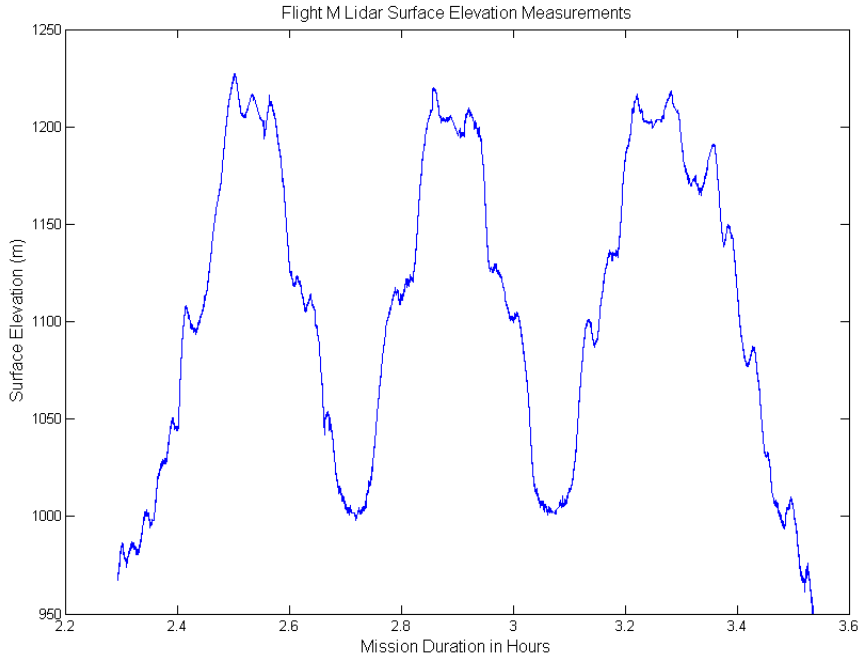

Fig. 6-1: A typical mission flight showing actual surface elevation in meters on the y-axis, and mission flight time in hours on the x-axis.

A plot of the measured distance between the UAV and the surface is shown in Fig. 6-2. The figure is from Flight Q and shows the benefit of using the Scambos and Haran DEM as a preflight tool to program the UAV flight altitudes. The relative distances between the UAV and the ice sheet surface were always above 210m yet less than 750m during the last 175 minutes of Flight Q. Note the wave-off at the landing (far right side of the figure) producing two trips of very close-to-the-surface returns. This shows the one occasion where the UAV had to wave-off a landing attempt due to severe crosswinds and circle the airfield for a second attempt at landing, which was successful.

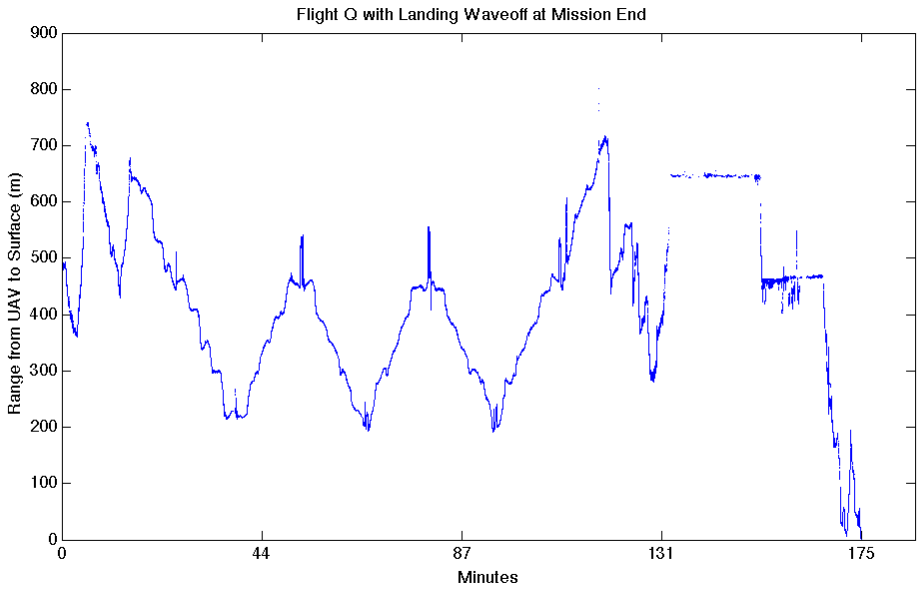

Fig. 6-2: Relative distance in meters between the UAV and the ice surface on the y-axis, with flight time in minutes on the x-axis.

Satellite Observations of Supraglacial Lakes

Supraglacial lake existences are quite variable. Some lakebeds do not fill at all during a season; others are full for short periods of time before draining, such as Lake 1 and Lake 4 during 2007. Still other lakes remain intact the entire season, such as Lake 3 during 2008.

During the 2008 Arctic MUSCOX campaign, Dr. Sarah Das was stationed at Lake 1, a lake surveyed with the UAS lidar system soon after it drained. In 2007 Dr. Das had placed a pressure sensor where the lake was likely to form during the melt season. She was able to retrieve the device in 2008, and determined the lake's maximum depth to be 7.9m at the device's location (personal correspondence); this compares well with the 2008 MUSCOX lidar survey depth of 7.1m at the same location.

Figures 6-3, 6-4, and 6-5 display overview matrixes of times when lakes were present and observed during 2006, 2007, and 2008 in MODIS imagery for each of the four study lakes of the inset strip (described in Chapter 4 and shown in Fig. 4-4). A red circle indicates a day (x axis) of clear MODIS imagery taken; a blue cross indicates the presence of one of the four supraglacial lakes on the inset strip (y axis is Lake number).

During 2006 (Fig. 6-3), all four lakes filled over time, and one drainage event occurred on Lake 1. The timing when lakes fill appears to be elevation dependent, with the higher elevation lake (Lake 4) filling later in time compared to the lower elevation lakes (Lakes 1, 2, and 3). Lake 3 might have formed after Lake 1 and Lake 2, but due to lack of clear sky MODIS imagery, this was not confirmed.

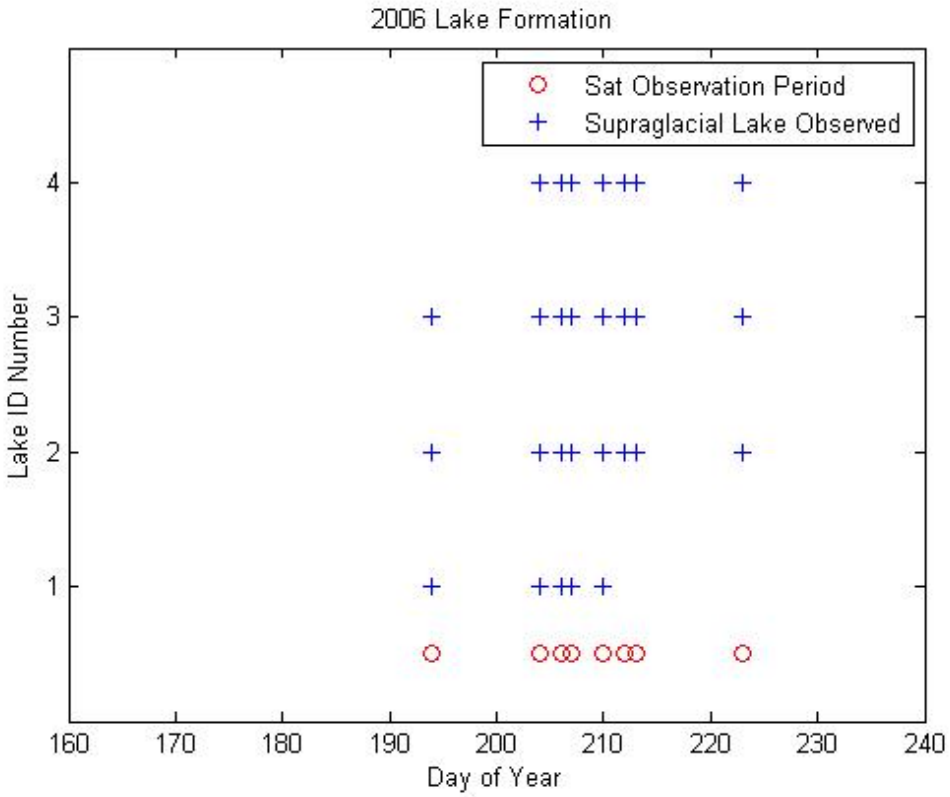

Fig. 6-3: Clear sky 2006 MODIS imagery dates vs. lake presence. MODIS satellite (sat) imagery (red circles) and supraglacial lake presence (blue crosses) are shown for each of the four study lakes (1-4) in the inset strip region. Note lake formation at lower elevations occurs before lake formation at higher regions. Lake 1 drained sometime before day 212.

Since higher elevation lake regions do not experience temperatures above 0°C until later in the summer, it is likely that higher elevation regions do not produce early runoff that flows to lakes at a lower elevation, as occurs in non-polar regions that have hills. Additionally, the travel distance of runoff appears to have a maximum distance of 12km in the western portion of the GIS (Rick, 2008). Later in the melt season, higher elevation runoff may be a more important factor, to include englacial conduits that can move water without visual observation.

In 2007 (Fig. 6-4), lakes are apparent at all four locations on the first day of available MODIS imagery, day 165. Therefore no elevation-dependent lake filling was observed. During this melt year, we see that Lake 1, Lake 3, and Lake 4 all drain, while Lake 2 never drains. Lake 4 was unique in that it refilled later in the melt season after it had initially drained.

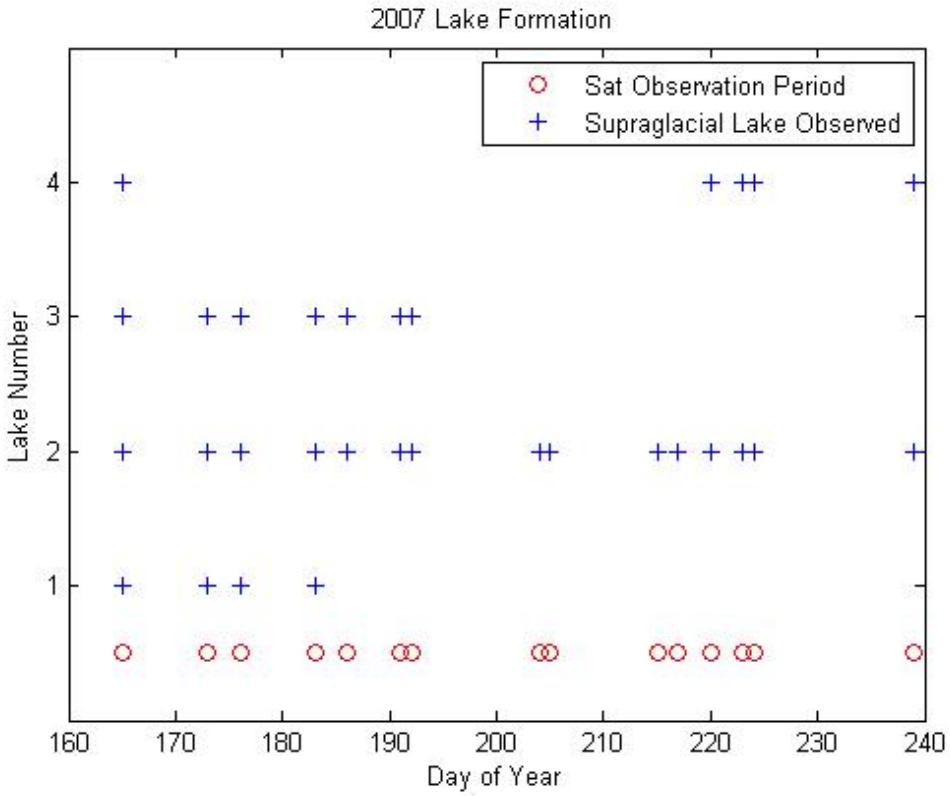

Fig. 6-4: Clear sky 2007 MODIS imagery dates vs. lake presence. MODIS satellite (sat) imagery (red circles) and supraglacial lake presence (blue crosses) are shown for each of the four study lakes (1-4) in the inset strip region. Lake 4 drains and refills during this season, while Lakes 1 and 3 drain without refilling.

The largest number of usable MODIS images (19) were found during the 2008 summer season (Fig. 6-5), enabling closer monitoring of the evolution of supraglacial lakes during that year. The elevation-dependent lake formation timeline appears similar to that of 2006, with Lake 3 and Lake 4 forming after Lake 1 and Lake 2. The drainage of

Lake 1 and Lake 2 was observed midway through the season, while Lake 3 and Lake 4 did not appear to drain during this season.

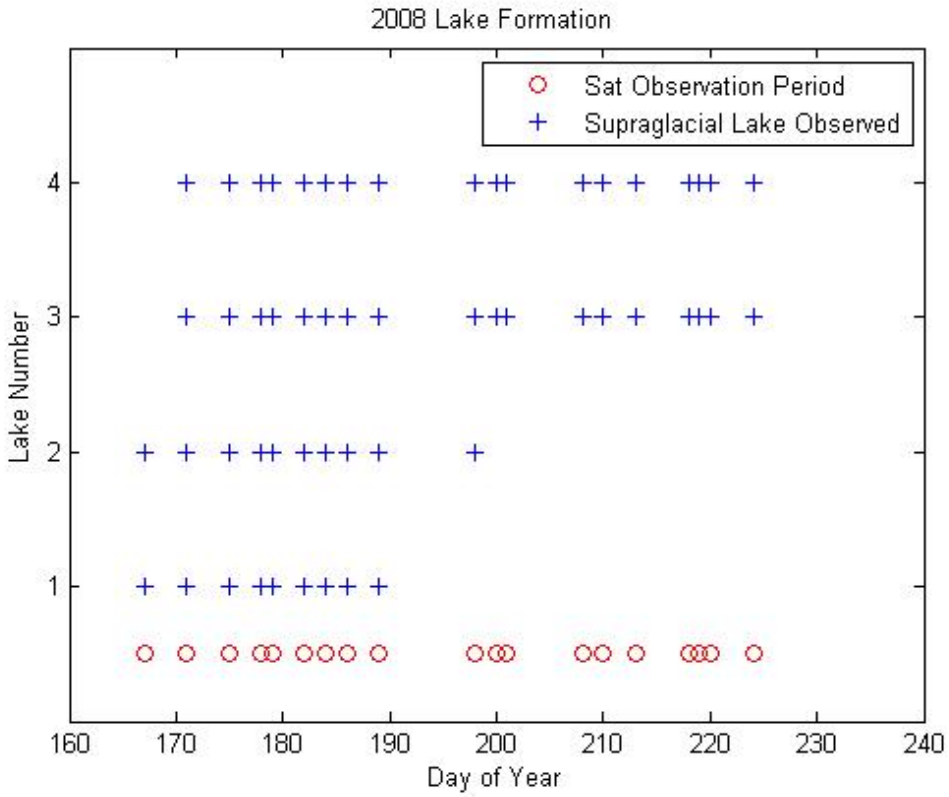

Fig. 6-5: Clear sky 2008 MODIS imagery dates vs. lake presence. MODIS satellite (sat) imagery (red circles) and supraglacial lake presence (blue crosses) are shown for each of the four study lakes (1-4) in the inset strip region. Note lake formation at lower elevations occurs before lake formation at higher regions. 2008 has more than twice the observable days than 2006.

In comparing volumes, it could be argued that higher mean temperatures would result in larger melt lakes, but surface topography also plays a role in lake formation. If a lake becomes too large it could spill over a low saddle threshold, and continue to flow downslope.

Alternatively, a lake could become large enough to force a severe crevasse in the ice sheet due to intensified pressure on the bottom of the lake. A rapid fracturing could

ensue, followed by a drainage event that propagates to the bedrock (Das et al. 2008). Supraglacial lakes therefore appear to have at least two regulatory processes that moderate their size.

The dH Model

The dH Model was designed to calculate Melt Water Equivalent (MWE) near the Jakobshavn region using surface height change measurements, and the values converted to runoff estimates for volumetric analysis. Observations from the AWS were used to obtain the height changes of the snow/ice surface during the melt seasons of 2006, 2007, and 2008. JAR1 normally has considerable snow in May, while JAR2's surface is thinly covered by snow. Therefore at JAR1 atmospheric temperature, in addition to the incoming solar energy, must first melt the snow cover before the ice can melt. The incoming solar energy and warmer temperatures at JAR2 can begin to melt the ice almost immediately. Sublimation occurs throughout the melt season at both locations, and while not considerable, it is taken into account using the rates determined by Box and Steffen (2001) and shown previously in Tables 5-3 and 5-4.

Using valid AWS temperature, humidity, and surface height data (previously described), a running mean of 30 samples was carried forward for all hourly interval readings throughout the three-year study period. Each individual sensor reading was then compared to +/- 10% of this running mean, with outliers removed. All readings were then averaged for each day by sensor, then each day was averaged by sensor type. If only one of the twin sensors was diagnosed as valid, only one measurement was used; a null value was used if both sensors were determined to be erroneous. For the surface height change measurements (dH), a relative height was created by subtracting the

surface height on May 13th of each year. Subsequently an incremental dH was calculated for each day.

The hourly interval readings for incoming and reflected SW were analyzed in the same manner; after calculating the daily SW fluxes, daily albedo was calculated by taking the ratio of reflected SW to incoming SW. The albedo measurements determined if the surface was snow, ice, or something in between. Using Table 5.1, this daily albedo was then converted into a surface density for each incremental day.

Daily sublimation rates were calculated using Table 5-4, and corrections applied to the daily dH measurements. Daily linear runoff values (in meters) were thus determined at each AWS station in the study area. JAR1 and JAR2's daily linear runoff calculations for each year are shown in Figs. 6-6 and 6-7.

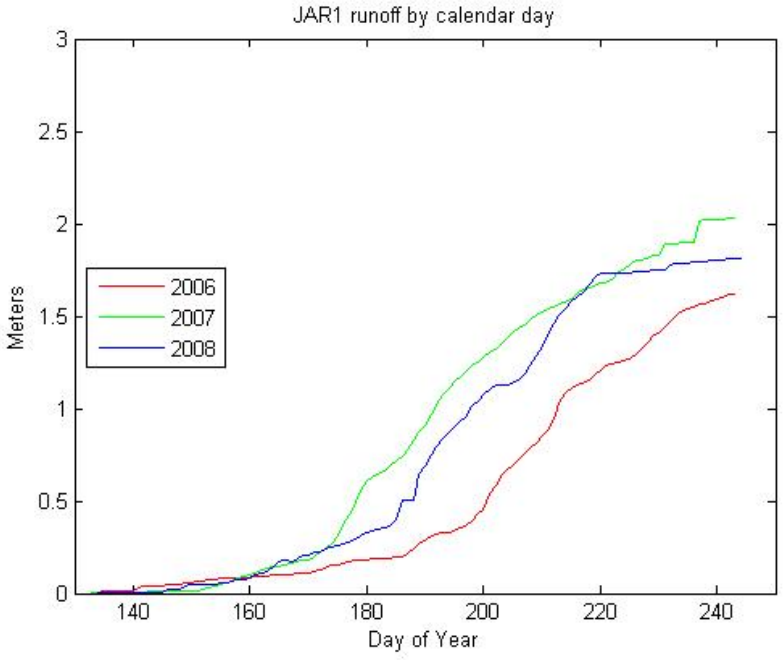

Fig. 6-6: JAR1 cumulative linear daily runoff from the dH Model.

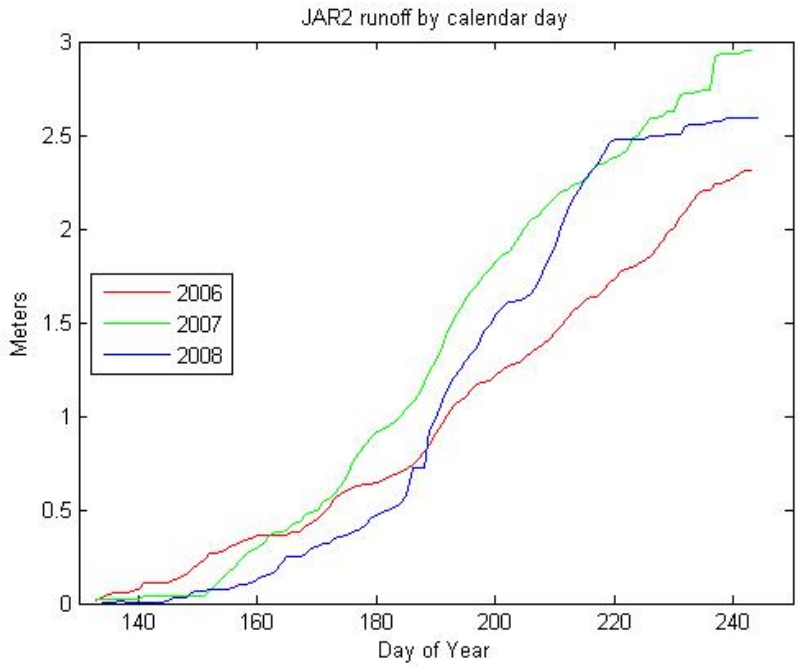

Fig. 6-7: JAR2 cumulative linear daily runoff from the dH Model.

Digital Elevation Models

At this point three DEM's were employed to best represent the hydrologically active icy terrain. It has been shown that melt water calculations are very sensitive to the DEM used, and variations in results can be attributed to accuracy problems and resolution issues of the DEM employed (Bamber et al., 2001). Using daily linear runoff calculations at JAR1, JAR2, and the upper linear runoff limit of zero runoff at 1700m, a model was developed to calculate runoff by elevation changes throughout the study region. Matlab code from Dr. Peter Blanken was modified to perform a three-point linear fit on a daily basis. While similar to the monthly linear models used for temperature and sublimation rates based on elevation changes (Huff, 2006; Box and Steffen, 2001), this model employs a daily changing rate for finer analysis based on observed surface height lowering.

The runoff results by design are therefore sensitive to changes dependent upon the daily inputs of the AWS measurements. The dH changes dictated a changing linear equation during each day of the three year's summer seasons. Fig. 6-8 shows graphically the daily dH Model outputs of slope and intercept for the linearization function to calculate runoff from JAR1, JAR2, and the zero runoff elevation of 1700m.

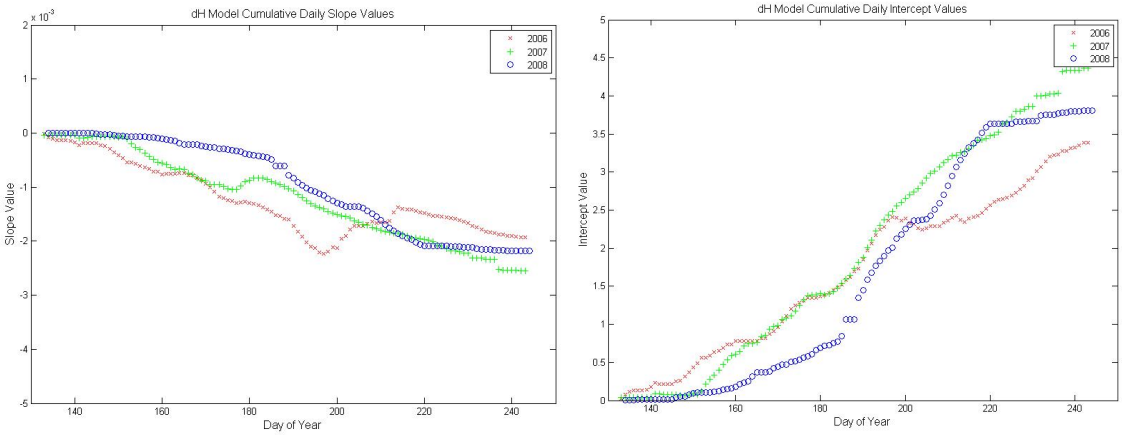

Fig. 6-8: dH Model cumulative daily slope and intercept linearizations based on the JAR1, JAR2, and the zero runoff elevation of 1700m.

Applying the daily changing linear function to the regional elevation profile, the total expected linear runoff was calculated for each point in the region, and each point of the inset strip. Figures 6-9, 6-10, and 6-11 show a typical day's linear runoff profile; in particular they are for August 31st of 2006, 2007, and 2008, respectively. The calculated linear runoff for JAR1, JAR2, and the zero runoff elevation of 1700m is shown for reference by blue circles on each graph. The linearization is then applied to each DEM datum point of the study region.

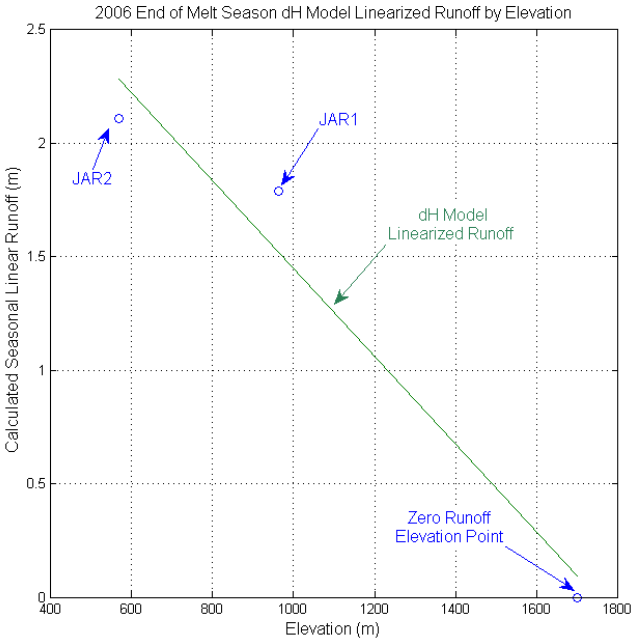

Fig. 6-9: The dH Model's linear runoff by elevation for August 31st, 2006. The calculated end of melt season runoff values from JAR1 and JAR2 are shown in Blue. The linear calculation to be applied to all elevations on that day is shown in Green

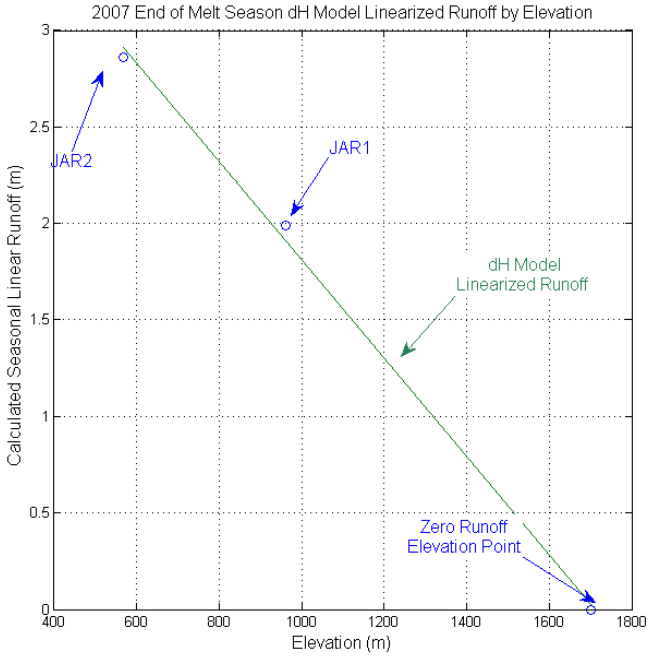

Fig. 6-10: The dH Model's linear runoff by elevation for August 31st, 2007. The calculated end of melt season runoff values from JAR1 and JAR2 are shown in Blue. The linear calculation to be applied to all elevations on that day is shown in Green

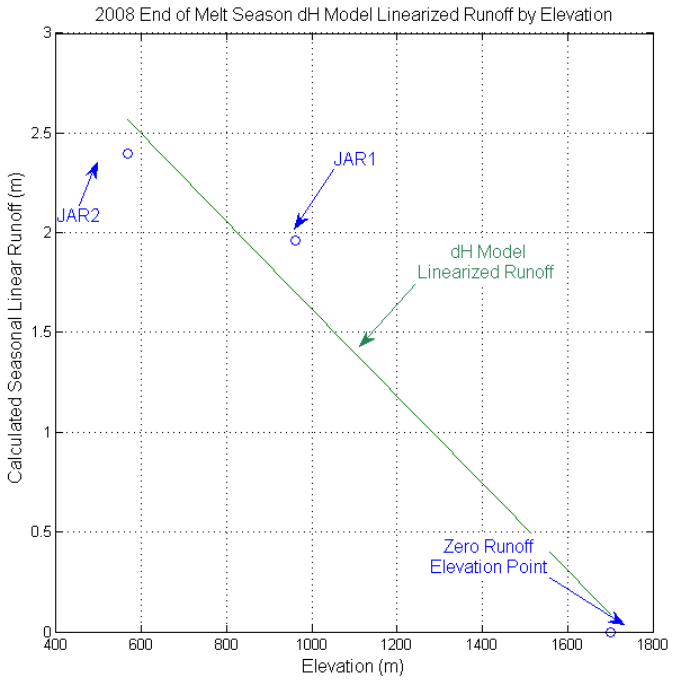

Fig. 6-11: The dH Model's linear runoff by elevation for August 31st, 2008. The calculated end of melt season runoff values from JAR1 and JAR2 are shown in Blue. The linear calculation to be applied to all elevations on that day is shown in Green

Table 6-1 tabulates the seasonal average slope and intercept of all daily linearizations describing surface height loss as a function of elevation for each year. The highest intercept (runoff) year is 2007, followed by 2008 and 2006; this is corroborated by the observations taken at JAR1 and JAR2 over the same timeframe. Of note, the sequence of years is the same order as the first appearance of the ice sheet (as measured by albedo), and the total number of Positive Degree Days per annum.

Table 6-1: Average slope and intercept values to determine runoff based on elevation in the Jakobshavn Isbrae region.

Year	Slope	Intercept
2006	-0.0012	1.678
2007	-0.0012	1.978
2008	-0.0010	1.687

The cumulative linear runoff calculations are performed on each datum point of the study area, producing daily linear runoff maps. Total runoff can then be calculated by multiplying each datum point's linear runoff by the physical area of each datum point. The end of the melt season's cumulative runoff values for the study region are shown in Figures 6-12, 6-13, and 6-14, and show the total runoff for 2006, 2007, and 2008, respectively. Contour lines for JAR1, JAR2, and the zero runoff elevation are also shown; the white areas are masked from runoff calculations.

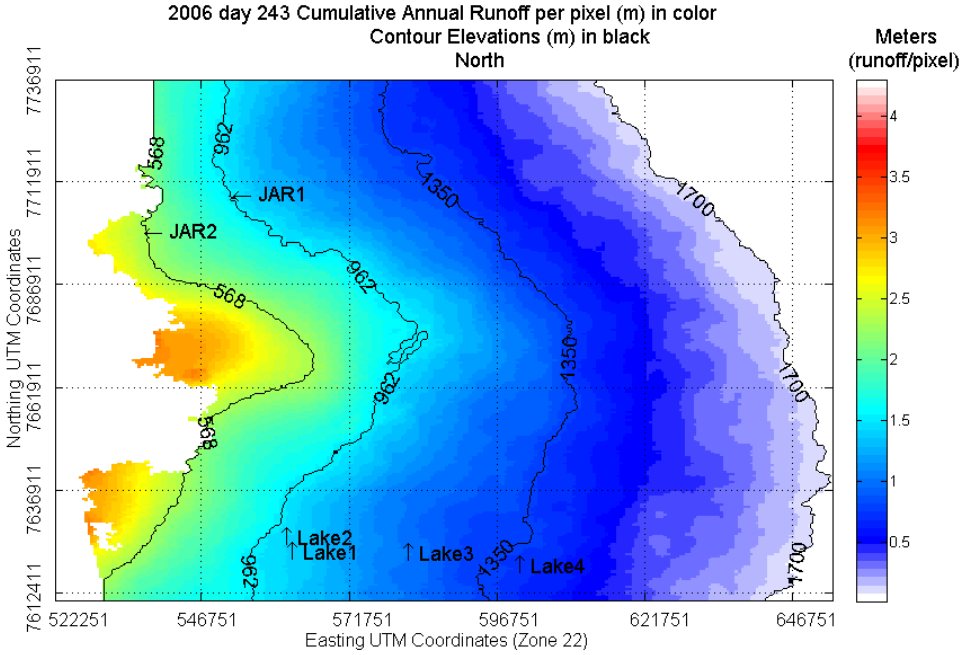

Fig. 6-12: Cumulative 2006 linear runoff values from the dH Model. Contour lines are shown for the elevations of JAR1, JAR2, a midpoint at 1350m, and at the 1700m upper limit of calculated runoff.

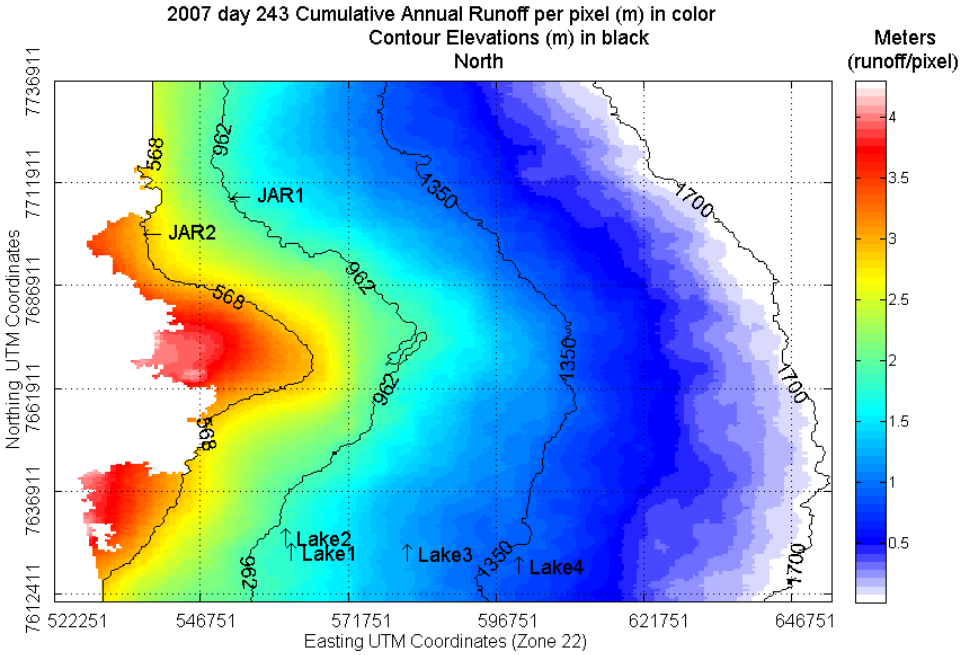

Fig. 6-13: Cumulative 2007 linear runoff values from the dH Model. Contour lines are shown for the elevations of JAR1, JAR2, a midpoint at 1350m, and at the 1700m upper limit of calculated runoff.

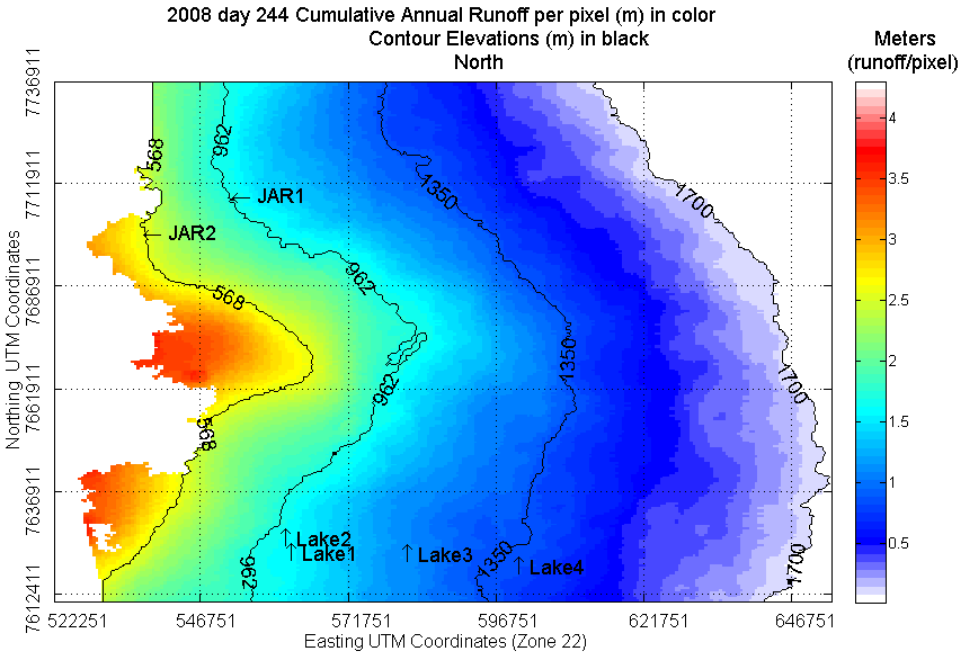

Fig. 6-14: Cumulative 2008 linear runoff values from the dH Model. Contour lines are shown for the elevations of JAR1, JAR2, a midpoint at 1350m, and at the 1700m upper limit of calculated runoff.

A comparison of the surface height change dH-derived runoff model to an existing energy balance model (SnowModel) was made over the entire study area to characterize the performance of the dH-derived runoff model. SnowModel was initialized by Dr. Sebastian Mernild with the same daily AWS input data source (GC-Net) for temperature, humidity, wind speed and wind direction. The tabulated results are shown in Table 6-2. SnowModel shows 2007 as the high melt year, but reverses 2006 and 2008 as the minimal melt year.

Table 6-2: SnowModel compared to JAR1 and JAR2 dH measurements.
[#] Years requiring extrapolation due to errors at the AWS site, as discussed in Chapter 4.

	2006	2007	2008
SnowModel surface height change (m) (cumulative, with mask)	3.00×10^4	3.38×10^4	2.75×10^4
SnowModel Masked Maximum surface height change per Pixel (m)	3.31	4.24	3.70
SnowModel Cumulative Masked Runoff Volume (m^3) (pixels masked = 6,592)	7.49×10^9	8.44×10^9	6.87×10^9
SnowModel JAR1 linear runoff (m)	0.95	1.09	0.85
SnowModel JAR2 linear runoff (m)	2.11	2.93	2.37
Measured JAR1 dH loss (m)	2.10	2.39[#]	2.48
Measured JAR2 dH loss (m)	2.18	2.59	2.63[#]

The energy balance model runoff calculations were not as representative of the observations as would be hoped. At JAR1, simulated runoff was below surface height by 55% for 2006, 54% for 2007, and 66% for 2008; even accounting for the measured snow

heights from Table 4-3 the runoff still appears low. However, JAR2's simulated runoff did appear to reflect the observations.

The dH Model retains the annual order shown by other indices, with 2007 having the highest runoff, followed by 2008 and then 2006. The dH Model calculations for both JAR1 and JAR2 are close to the actual observations, as shown in Table 6-3.

Table 6-3: The dH Model compared to JAR1 and JAR2 measurements.
[#] Years requiring extrapolation due to errors at the AWS site, as discussed in Chapter 4.

	2006	2007	2008
dH Model surface height change (m) (cumulative, with dual mask)	4.80×10^4	5.92×10^4	5.35×10^4
dH Model Masked Maximum surface height change per Pixel (m)	3.28	4.22	3.70
dH Model Cumulative Masked Runoff Volume (m^3) (pixels masked = 9,014)	1.20×10^{10}	1.48×10^{10}	1.34×10^{10}
dH Model JAR1 linear runoff (m)	1.79	1.99	1.96
dH Model JAR2 linear runoff (m)	2.11	2.86	2.40
Measured JAR1 dH loss (m)	2.10	2.39[#]	2.48
Measured JAR2 dH loss (m)	2.18	2.59	2.63[#]

Efforts at identifying reasons for the energy balance model's discrepancy at JAR1 did not highlight any particular error source. Therefore, in the comparison of both models' outputs vs. measured surface height change, the dH Model performed well in characterizing the runoff levels; it will be used to calculate runoff for the inset strip, previously shown in Fig. 4-4. The SnowModel results were not used further in this study.

Supraglacial Lake Sizes

To determine lake areal extent, only 250m MODIS overhead imagery was used; other MODIS imagery has 500m resolution and will not determine lake edge boundary conditions as accurately. There are two 250m channels, Band 1 at 858nm, and Band 2 at 645nm; and both are used exclusively in this study. To create visual RGB (Red, Green, Blue) images, Band 1 was placed into both Red and Green channels, while Band 2 was placed in the Blue channel.

The usable (cloud-free) MODIS imagery over the inset strip location resulted in 42 days of observations encompassing the four lakes, as shown in Table 6-4.

Table 6-4: The number of usable MODIS days for the inset strip in addition to the year, day of year, and UTC for each image.

2006 (8)	2007 (15)	2008 (19)
2006_194_1425	2007_165_1425	2008_167_1520
2006_204_1505	2007_173_1515	2008_171_1500
2006_206_1450	2007_176_1545	2008_175_1610
2006_207_1355	2007_183_1415	2008_178_1505
2006_210_1605	2007_186_1445	2008_179_1545
2006_212_1415	2007_191_1505	2008_182_1615
2006_213_1455	2007_192_1410	2008_184_1605
2006_223_1355	2007_204_1435	2008_186_1555
	2007_205_1515	2008_189_1625
	2007_215_1415	2008_198_1440
	2007_217_1540	2008_200_1605
	2007_220_1435	2008_201_1510
	2007_223_1505	2008_208_1515
	2007_224_1410	2008_210_1505
	2007_239_1505	2008_213_1535
		2008_218_1415
		2008_219_1635
		2008_220_1540
		2008_224_1515

Each entry gives the image's year, day of year, and time in Coordinated Universal Time (UTC). There were 8 dates in 2006, 15 dates in 2007, and 19 dates in 2008.

Histograms of each MODIS image were inspected for the distribution of surface reflectance, also known as DN's (digital numbers). Different days exhibit different reflectances due to factors such as the satellite used, and its positioning relative to the Jakobshavn Isbrae; thus darker or lighter scenes can appear over time. In order to determine supraglacial lake vs. ice, different DN cutoff thresholds for each Band were chosen for each image.

The histograms show why it is imperative to adjust each image on an individual basis. Typical DN threshold values were 120 for the Blue channel, and 105 for the Red/Green channel. An example of a histogram for both the Blue and the Red/Green channels, and the resulting false color images for Lake 1, are shown in Figures 6-15, 6-16, 6-17, and 6-18.

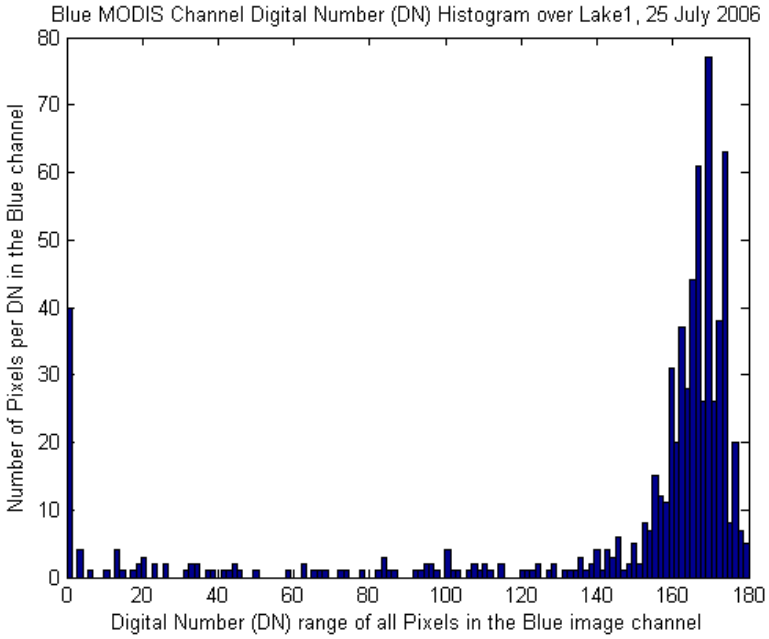

Fig. 6-15: Histogram of DN's of Lake 1 in the Blue channel. Higher numbers indicate the reflective ice and snow; the lower numbers indicate the darker water areas.

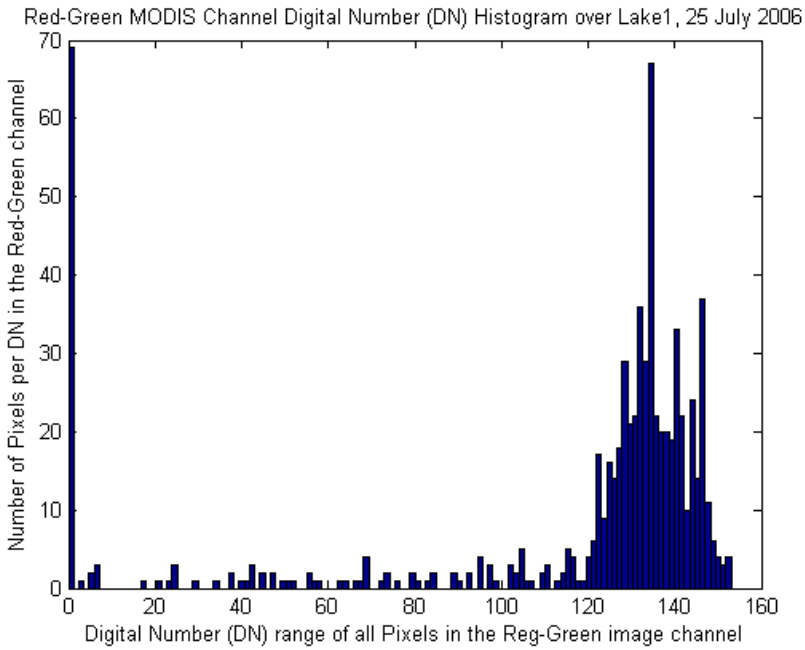

Fig. 6-16: Histogram of DN's of Lake 1 in the Red/Green channel. Higher numbers indicate the reflective ice and snow; the lower numbers indicate the darker water areas.

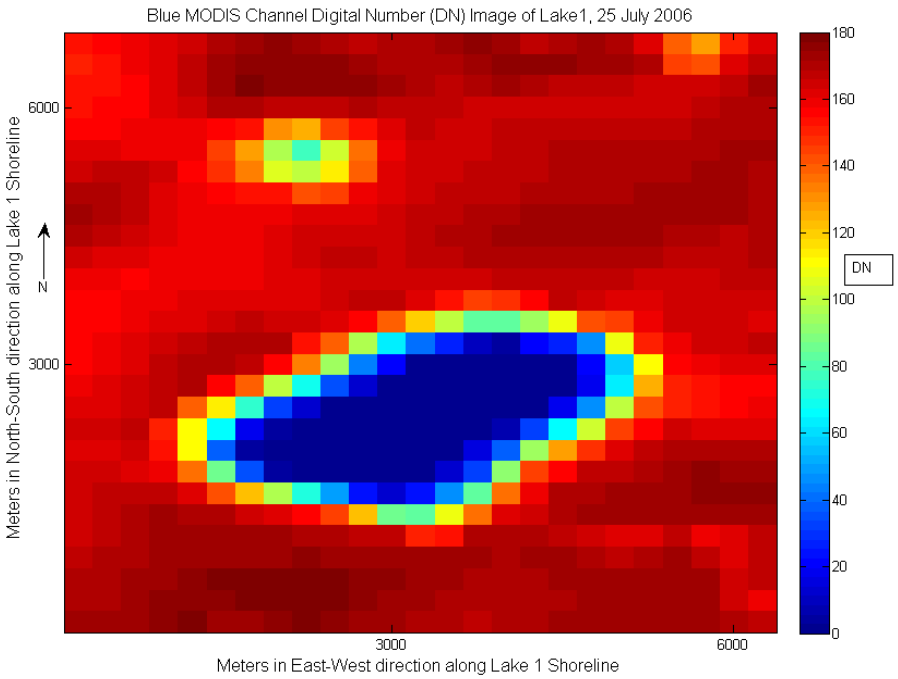

Fig. 6-17: Lake 1 (large) and Lake 2 (small) in the Blue Channel. The color bar indicates the DN of each 250m pixel.

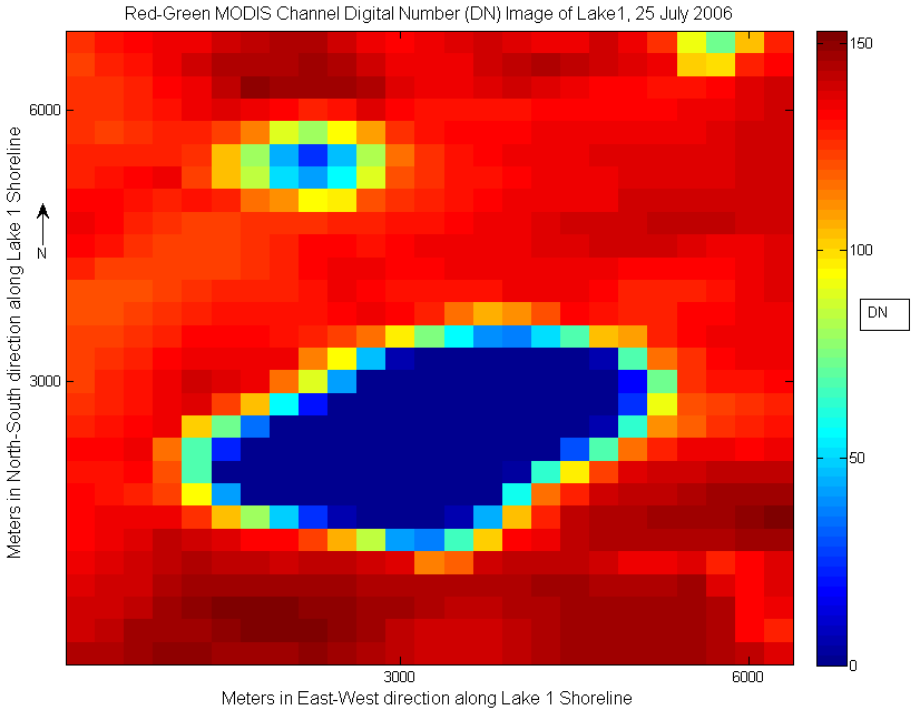

Fig. 6-18: Lake 1 (large) and Lake 2 (small) in the Red/Green Channel. The color bar indicates the DN of each 250m pixel.

A binary mask was produced for each lake with all non-lake pixels masked to zero (0) and all lake pixels masked to one (1); the mask for Lake 1 on July 25th, 2006 is shown in Fig. 6-19. Multiplying these masks over a particular dataset (imagery or elevation data) will remove all non-Lake pixels from subsequent analysis.

Fig. 6-19: Lake 1 Binary Mask of 250m MODIS imagery from 25 July, 2006. The x- and y- axes indicate the size of the lake in meters.

These masked lake images enabled two important techniques in determining lake volume. First, the masked lake images had to be converted from 250m resolution to the ASTER DEM resolution of 30m as shown in Fig. 6-20. This would allow for the lake's masked area to drape over the 30m DEM, identifying the pixels that would be used for daily depth calculations. Each pixel's depth range in meters would then be summed to provide the daily volume of the lake.

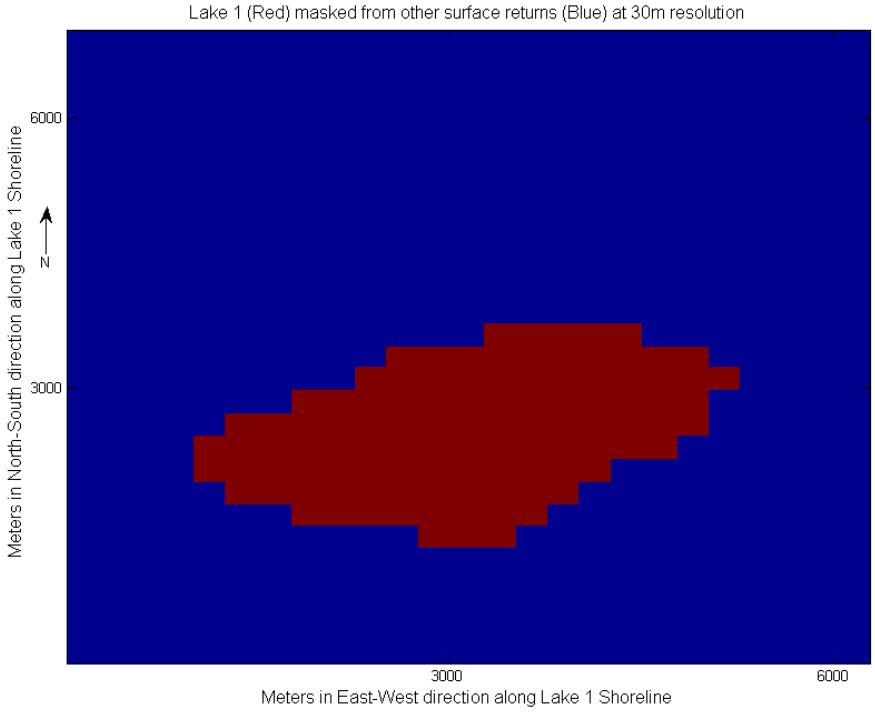

Fig. 6-20: Lake 1 Binary Mask converted to 30m ASTER DEM resolution, from the 250m resolution MODIS mask of 25 July, 2006.

Secondly, the masked lake images had to be converted to 500m resolution to be compatible with the dH Model runoff estimates for the inset strip. The strip's rectangular shape was chosen vs. a water basin approach for two reasons. Since water follows the gradient of gravity, it is much more probable a lake's source will be from upslope vice another direction. The narrow shape of the strip allows for westerly water flow along the sloping ice sheet to lower elevations. Secondly, it is known that unseen englacial conduits exist that can move large quantities of water to other parts of the ice sheet. Therefore, a local basin might not be the only source or sink of liquid water for a given lake. It is hoped that a spatially defined rectangle could help identify such unknown sources or sinks, as melt and runoff calculations can be balanced against the observed standing water.

The date of maximum lake size is tabulated in Table 6-5. This date does not imply a lake drainage event subsequently follows; it could be there was no available imagery to observe an actual drainage event.

Table 6-5: Dates and times of maximum observed lake size.

Lake number	2006 day time	2007 day time	2008 day time
1	207_1355	176_1545	186_1555
2	206_1450	183_1415	186_1555
3	223_1355	192_1410	218_1415
4	212_1415	165_1425	198_1440

The date of a lake's last observation is tabulated in Table 6-6, in many cases this was also the last day of available imagery (indicated by an *). Of note, Lake 4 drained and refilled in 2007, the only time an event of this type was observed. The actual daily lake volumes and areal sizes follow towards the end of this chapter.

Table 6-6: Last supraglacial lake observation date and time.
* indicates the lake was observed in the last MODIS image available for the year.
+ indicates the supraglacial lake drained, then reformed later in the melt season.

Lake number	2006 day time	2007 day time	2008 day time
1	210_1605	183_1415	189_1625
2	223_1355*	239_1505*	198_1540
3	223_1355*	192_1410	224_1515*
4	223_1355*	239_1505*+	224_1515*

Potential Runoff Sources

The inset strip's size is 13km by 91km, or 1,183km^2, as shown in Fig. 6-21; the elevation changes of interest range from 926m to 1700m. The inset strip size was then

masked for each Lake to exclude runoff from lower elevations being counted as a potential runoff source, as shown for each Lake in Figures 6-22, 6-23, 6-24, and 6-25.

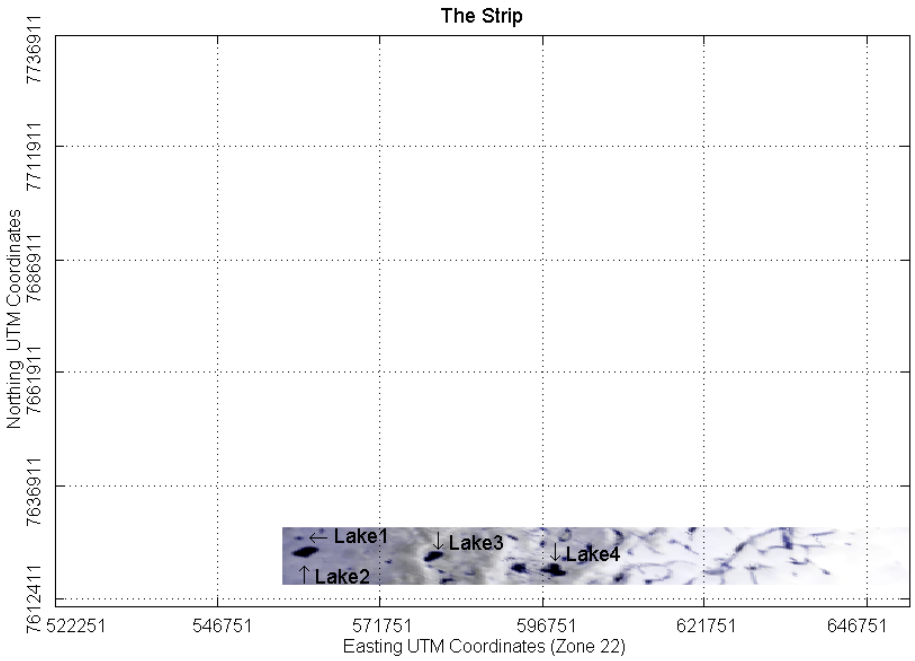

Fig. 6-21: The inset strip containing all four supraglacial lakes.

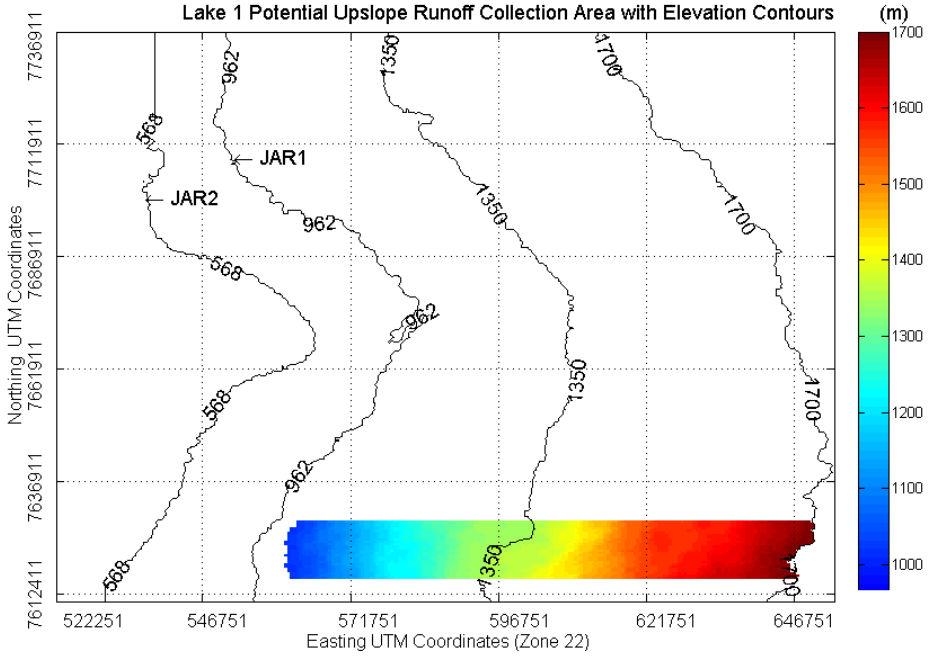

Fig. 6-22: Lake 1's maximum potential runoff sources.

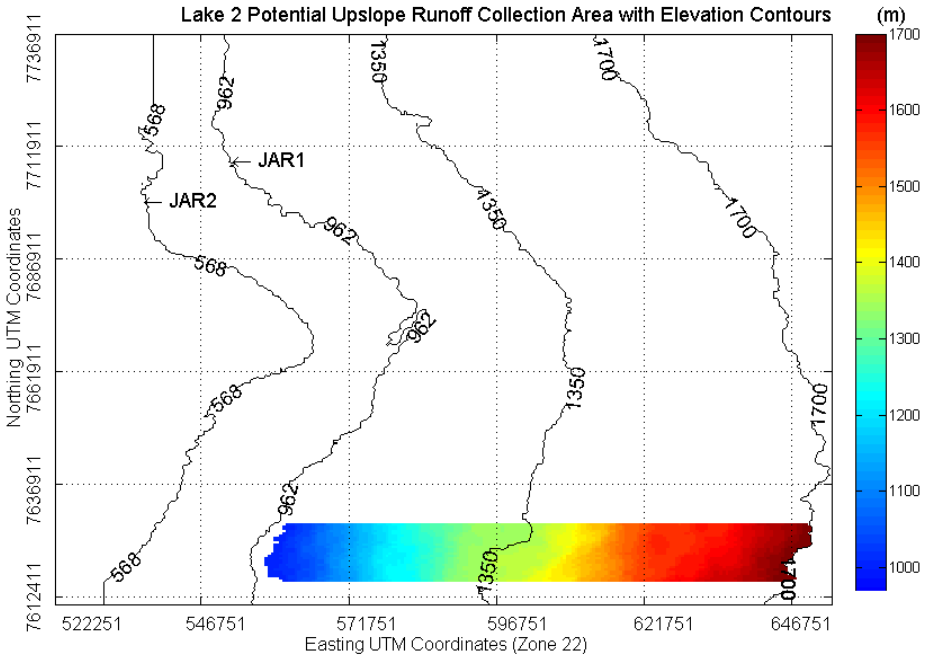

Fig. 6-23: Lake 2's maximum potential runoff sources.

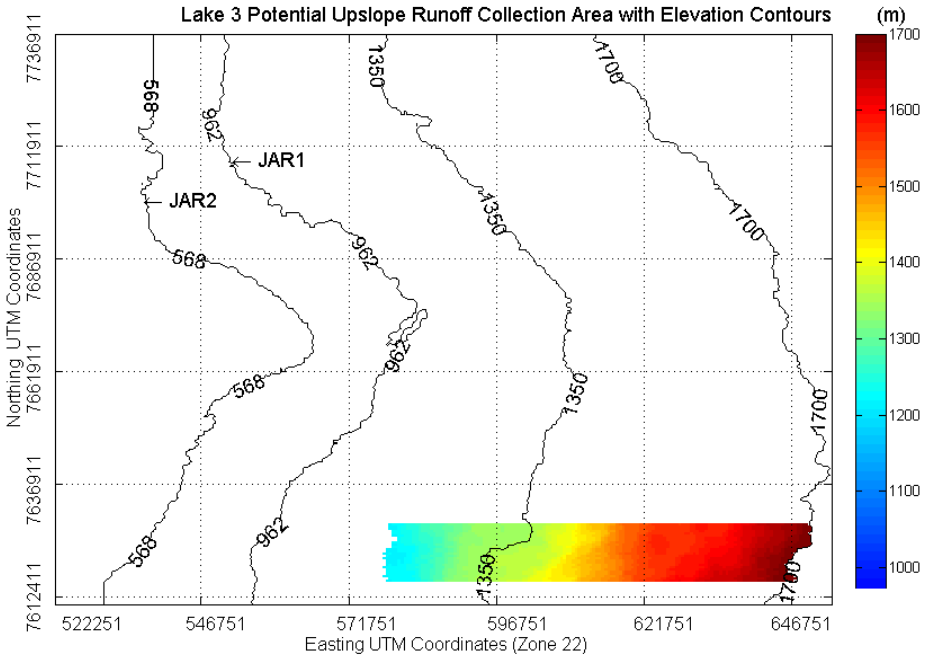

Fig. 6-24: Lake 3's maximum potential runoff sources.

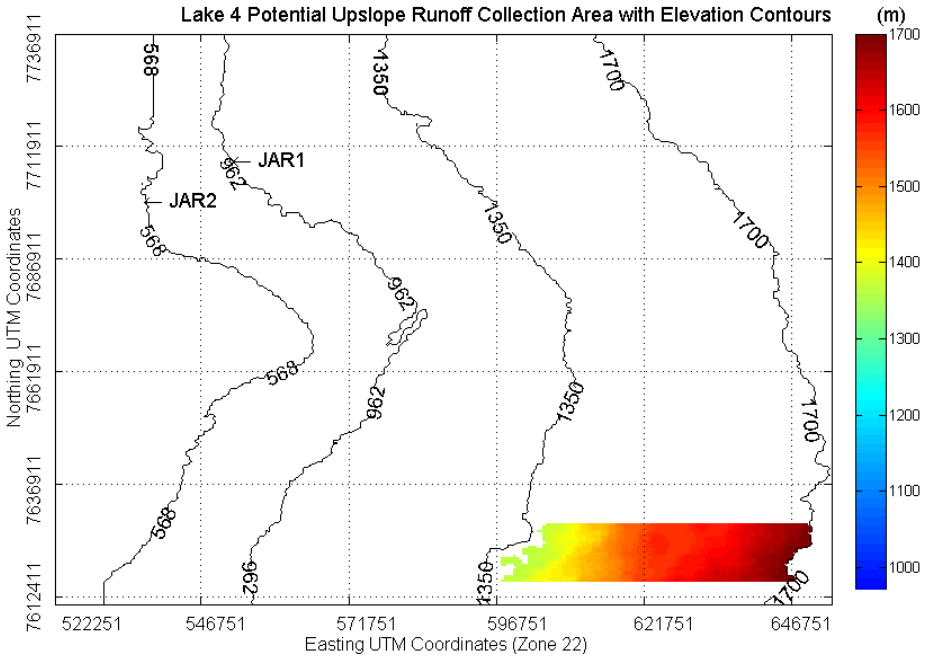

Fig. 6-25: Lake 4's maximum potential runoff sources.

The total potential runoff into each lake was calculated by area; Lake 1 above 1014m (consisting of 1129km^2), Lake 2 above 997m (consisting of 1157km^2), Lake 3 above 1215m (consisting of 905km^2), and Lake 4 could be supplied by elevations above 1363m (consisting of 604km^2).

Aggregated Runoff and Lake Volume Calculations

Daily volumetric runoff for the inset strip was calculated using the dH Model, while masking all areas not within the inset strip. The PDD's, 2m surface temperatures, and combined 4 lake volumes are shown for ease of comparison in Figures 6-26, 6-27, and 6-28; each figure is for one study year. The volume of all four study lakes are aggregated in the top panel, JAR1's daily averaged temperature is shown in the second panel when

temperatures went above 0°C, the daily PDD's are displayed for reference in the third panel, and the cumulative runoff throughout the inset strip is calculated in the final panel.

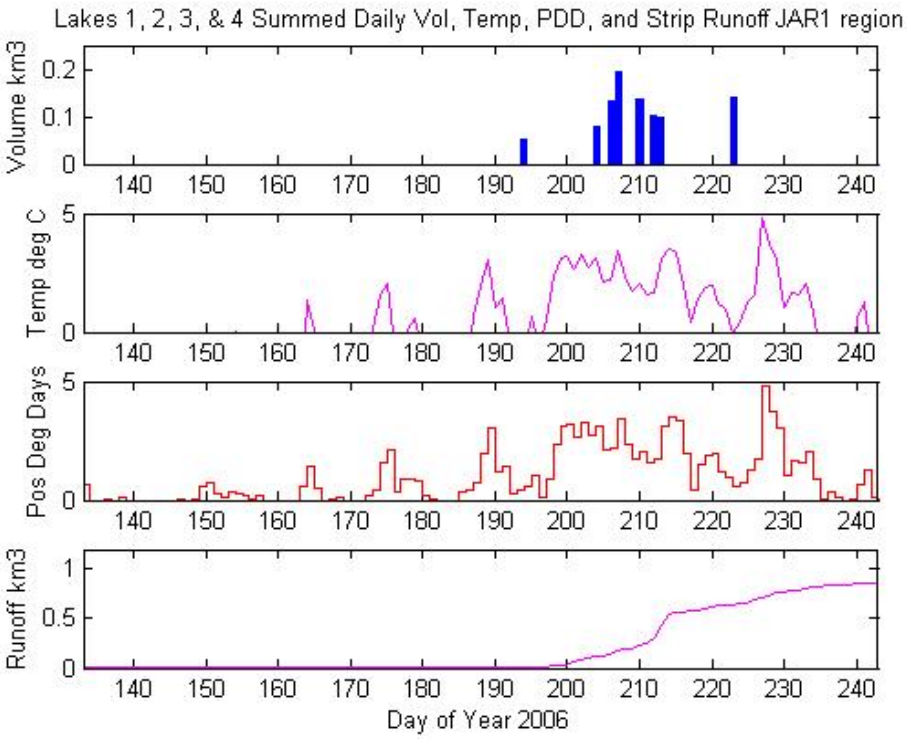

Fig. 6-26: Summary graphic of combined Lake volumes for 2006. Lake volumes appear in conjunction with increasing runoff.

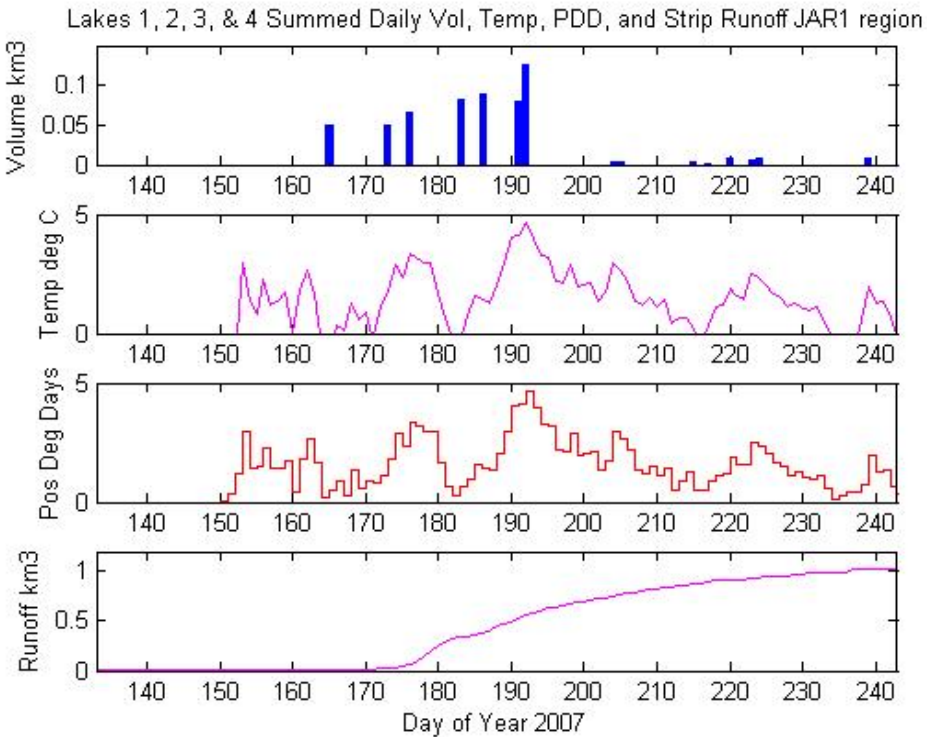

Fig. 6-27: Summary graphic of combined Lake volumes for 2007
Lake volumes appear before increasing runoff.

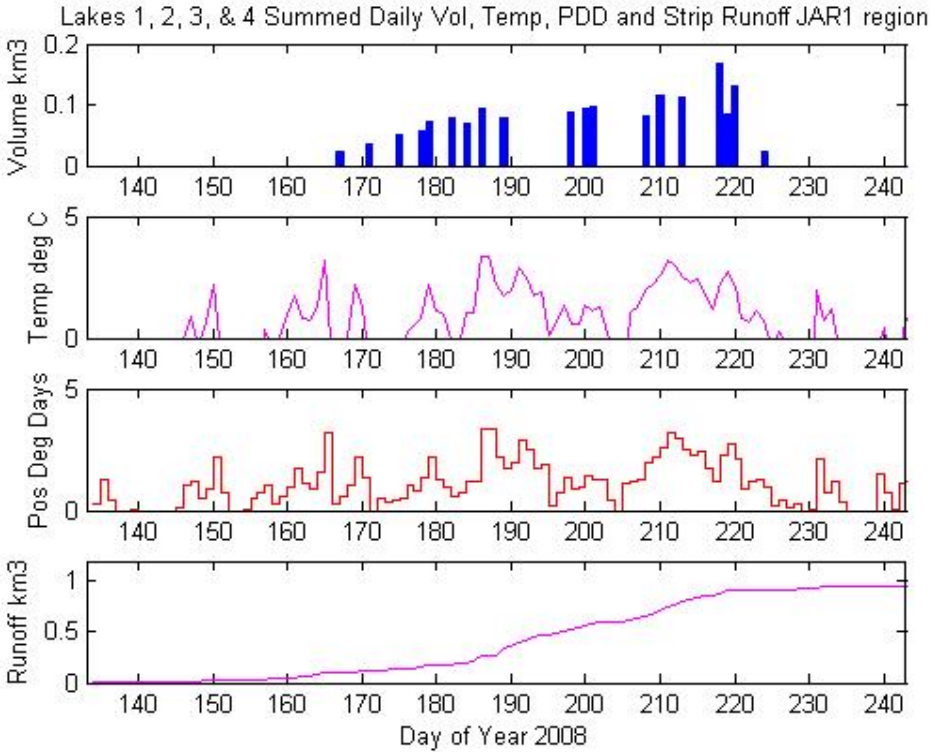

Fig. 6-28: Summary graphic of combined Lake volumes for 2008.
Lake volumes appear in conjunction with increasing runoff.

Figure 6-29 shows the three years of runoff calculations of the inset strip for interannual comparison. Runoff for 2007 begins much earlier than 2006, as expected due to the early number of PDD's. However, 2008 indicates runoff even earlier than 2007, although it had fewer PDD's. This could be possible if decreasing high altitude cloud-cover enabled more incoming SW to heat the surface throughout the Jakobshavn region. As shown in Table 6-4, there was a 25% increase in the number of usable clear sky MODIS images for 2008 than 2007, and greater than 100% more usable days than 2006.

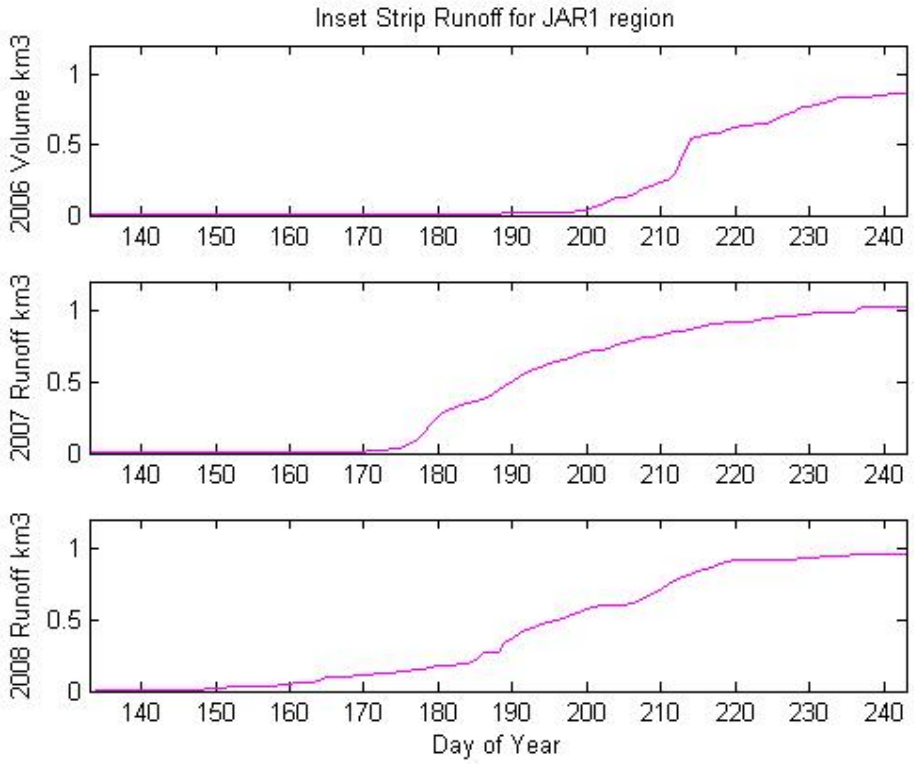

Fig. 6-29: Runoff for the inset strip for 2006, 2007 and 2008.

On a daily basis the calculated lake volumes were then compared to the calculated runoff volumes of the inset strip; the results show a high variability of supraglacial lake formation and size during this three-year study. The diverse time sequence of the

percentage of lake volume over runoff volume is shown in Fig. 6-30. One evident feature common for all years is the reduction in percentage as the melt season progresses.

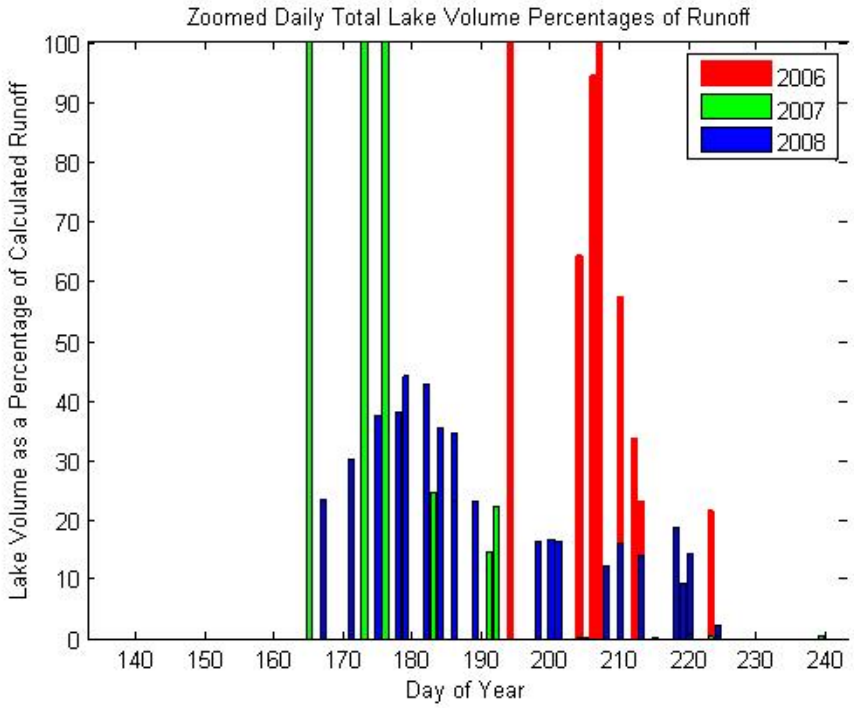

Fig. 6-30: Supraglacial lake presence over all years observed. Note 2007 lake volumes appear earlier in the melt season, while 2006 melt volumes are seen later in the melt season. 2008 has a lake presence throughout the melt season.

During 2006 and 2007 lake volumes appear greater than the inset strip's runoff production, as shown by the taller red and green segments of Fig. 6-30. These occurrences likely indicate water sources from beyond the inset strip's width finding pathways to form the four supraglacial lakes. The water could be loosely following riverine structures closely paralleling contour lines as opposed to a direct downslope movement; thereby lake volumes would increase relative to the inset strip runoff production calculations. This scenario would also match observation that melting occurs at lower elevations earlier in the season; a contour-following flow would then create

supraglacial lakes at these lower elevations. Water flow would then be followed by upslope meltwater from later in the season.

Additionally, as indicated by Rick (2008) water flow movements across the ice sheet would most likely not exceed 12km, therefore, upslope production (which was accounted for) is not the likely origin for the more distant lakes. The width of the inset strip was initially chosen to be 13km, with the assumption most water would come from upslope. It appears earlier in the melt season the water could be originating from beyond the 6.5km centerline of the inset strip along a similar elevation contour.

The higher ratios of lake volume to runoff production early in the season could indicate a structural problem with the dH Model. However, each year does fall below a 100% ratio over time, and 2008 never experiences ratios greater than 50%. It is likely the dH Model for calculating runoff is sound, but the size and shape of the inset strip needs to be reviewed. These facts demonstrate the need for continued analysis of localized runoff production in addition to continuing the calculation of individual supraglacial lake volumes.

One other possibility is a lake's surface freezing at the end of the melt season, leaving the meltwater of the lake intact for the next year. Once the ice on the lake's surface melted at the beginning of the next melt season, the remaining lake water is exposed (but is not a product of that year's melt). This could produce an observed lake without observed runoff.

For completeness, Figure 6-31 shows the runoff calculated for the entire Jakobshavn region over the three year study period. This data was used to compare with the SnowModel simulated runoff figures, specifically at the JAR1 and JAR2 locations.

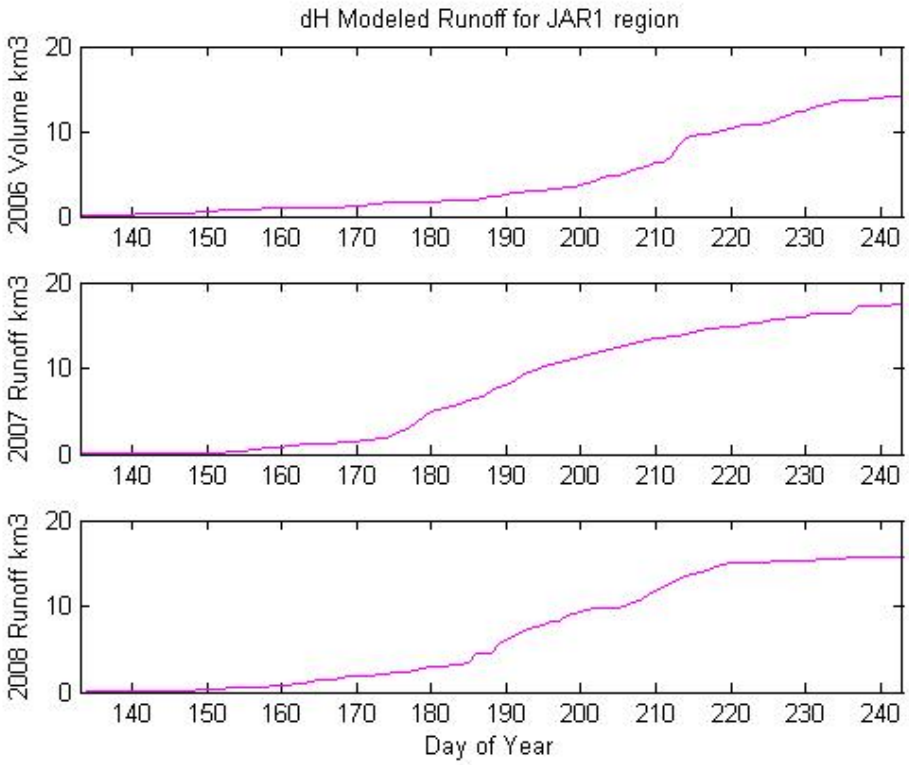

Fig. 6-31: The runoff for the entire study area.
Note the steady increases made during 2006 and 2008,
while 2007 had more rapid slope.

The observed daily volume (km^3) of each supraglacial lake of the inset strip is tabularized by year and shown in Tables 6-7, 6-8, and 6-9. One notable point in this study is that supraglacial lake volumes never exceeds ~0.15km^3 for any lake.

Table 6-7: 2006 supraglacial lake volumes (km^3) by day.

Year/Date/Time	Lake 1	Lake 2	Lake 3	Lake 4
2006_194_1425	0.039	0.011	0.001	0.000
2006_204_1505	0.041	0.016	0.011	0.010
2006_206_1450	0.042	0.016	0.044	0.030
2006_207_1355	0.067	0.012	0.067	0.050
2006_210_1605	0.053	0.002	0.052	0.030
2006_212_1415	0.000	0.000	0.056	0.045
2006_213_1455	0.000	0.001	0.050	0.048
2006_223_1355	0.000	0.000	0.088	0.050

Table 6-8: 2007 supraglacial lake volumes (km^3) by day.

Year/Date/Time	Lake 1	Lake 2	Lake 3	Lake 4
2007_165_1425	0.022	0.006	0.002	0.020
2007_173_1515	0.029	0.009	0.012	0.000
2007_176_1545	0.036	0.008	0.022	0.000
2007_183_1415	0.000	0.014	0.069	0.000
2007_186_1445	0.000	0.013	0.076	0.000
2007_191_1505	0.000	0.004	0.075	0.000
2007_192_1410	0.000	0.001	0.124	0.000
2007_204_1435	0.000	0.002	0.000	0.000
2007_205_1515	0.000	0.003	0.000	0.000
2007_215_1415	0.000	0.004	0.000	0.000
2007_217_1540	0.000	0.001	0.000	0.000
2007_220_1435	0.000	0.003	0.000	0.006
2007_223_1505	0.000	0.001	0.000	0.005
2007_224_1410	0.000	0.000	0.000	0.008
2007_239_1505	0.000	0.001	0.000	0.007

Table 6-9: 2008 supraglacial lake volumes (km^3) by day.

Year/Date/Time	Lake 1	Lake 2	Lake 3	Lake 4
2008_167_1520	0.018	0.003	0.000	0.000
2008_171_1500	0.027	0.004	0.005	0.000
2008_175_1610	0.032	0.009	0.009	0.001
2008_178_1505	0.029	0.004	0.021	0.003
2008_179_1545	0.042	0.008	0.017	0.007
2008_182_1615	0.046	0.009	0.017	0.006
2008_184_1605	0.043	0.005	0.015	0.006
2008_186_1555	0.050	0.009	0.021	0.013
2008_189_1625	0.043	0.004	0.019	0.013
2008_198_1440	0.000	0.001	0.061	0.026
2008_200_1605	0.000	0.000	0.075	0.020
2008_201_1510	0.000	0.000	0.070	0.026
2008_208_1515	0.000	0.000	0.067	0.014
2008_210_1505	0.000	0.000	0.093	0.022
2008_213_1535	0.000	0.000	0.093	0.019
2008_218_1415	0.000	0.000	0.147	0.020
2008_219_1635	0.000	0.000	0.073	0.012
2008_220_1540	0.000	0.000	0.115	0.017
2008_224_1515	0.000	0.000	0.001	0.022

Figures 6-32, 6-33, 6-34, and 6-35 show the interannual volume characteristics of each lake as it fills and drains on a daily basis. The lack of available clear sky satellite imagery is evident, and is a major limitation in space-based observations of supraglacial lakes. Small unmanned aircraft could provide more detailed and timely information on the ice sheet.

These four particular lakes exhibit a slowly filling mode, and a rapid draining profile. They appear to have a natural size limit, but further research would need to be done to see if the 0.15km^3 is a prevalent feature.

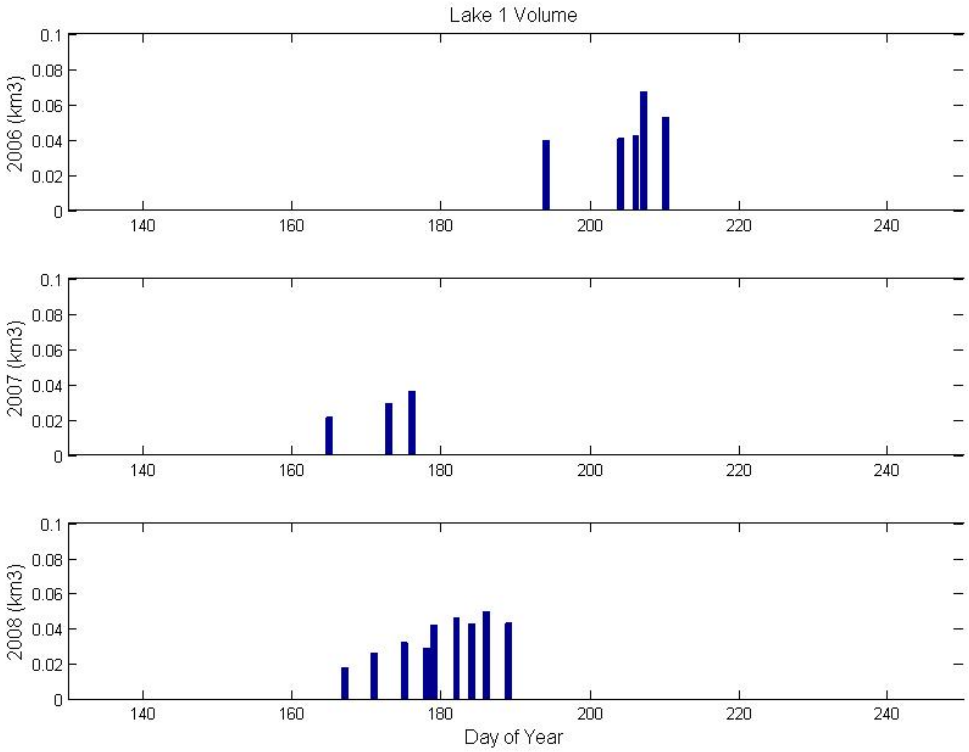

Fig. 6-32: Lake 1's volume changes over the melt season.

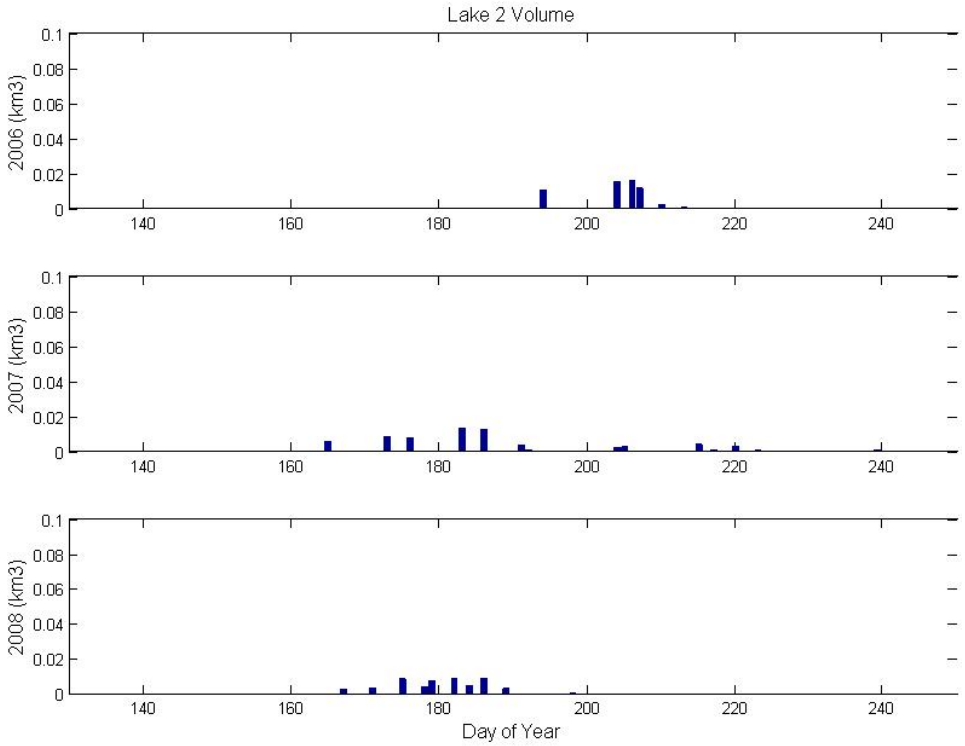

Fig. 6-33: Lake 2's volume changes over the melt season.

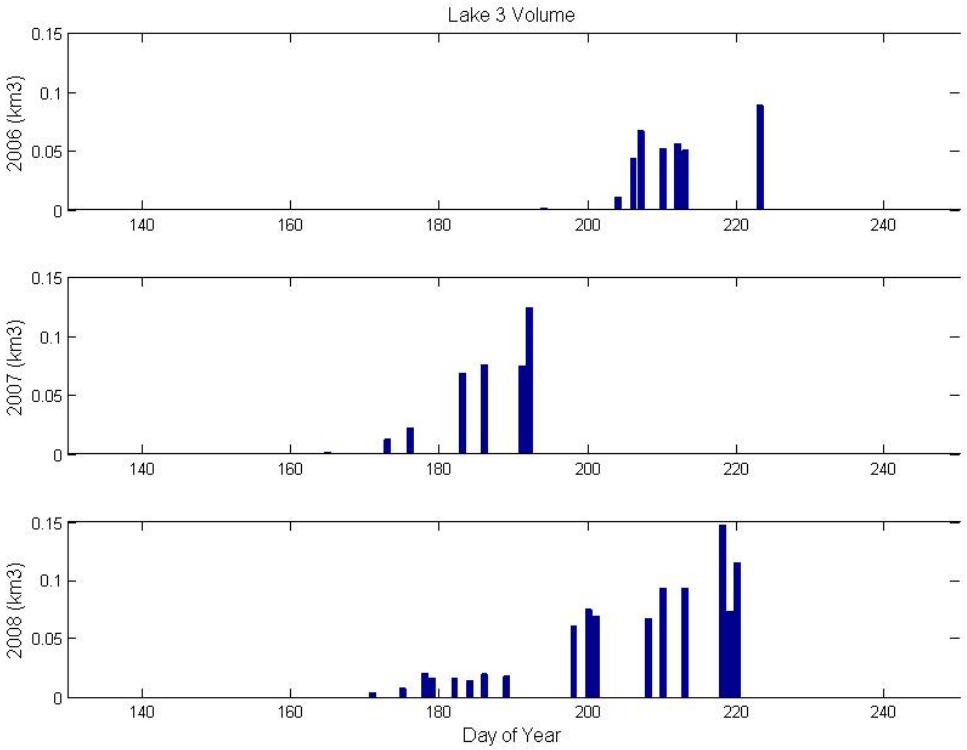

Fig. 6-34: Lake 3's volume changes over the melt season.

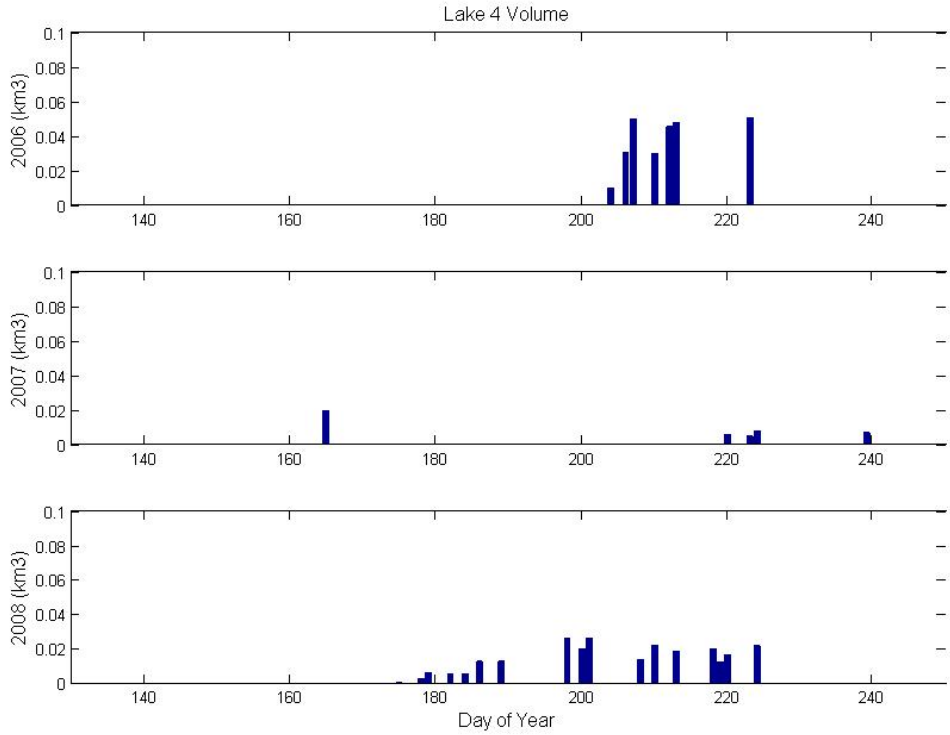

Fig. 6-35: Lake 4's volume changes over the melt season.

Chapter Summary

Many data sources were used to obtain supraglacial lake volumes and calculate the local area runoff, including in-situ surface height measurements from the GC-Net, daily satellite images from MODIS, and digital elevation models from ASTER, NSIDC, and the Arctic MUSCOX program. Two computational models were used to predict runoff over the Jakobshavn region, an energy balance model and a surface height change model; the latter was selected for continued use in the study since its calculations more closely matched the observations.

Supraglacial lake volumes were calculated for four lakes appearing along a 13km by 91km area of interest along a transect at 68.73°N. Daily volumes for all lakes were presented for each day of available MODIS imagery; a maximum lake area of 10.4km^2 and

a maximum lake volume of 0.147km^3 was seen over the three years. The dH Model was used to calculate runoff for the region and the inset strip.

The observations in this study suggest a dynamic system with many ways to fill or drain supraglacial lakes; the runoff calculations imply that earlier in the melt season hydrologic linkages could extend beyond the 6.5km centerline imposed by the study. These water sources could be from a more lateral portion of the ice sheet flowing along the contour lines, rather than in a downslope direction. A more detailed study to include the identification and quantification of all surface and subsurface water transport should be conducted to verify this possibility.

The individual lake characteristics are highly dynamic; lakes can form during one melt season and not the next, remain intact throughout the season or drain part way through the summer, and some can even drain and refill within the same melt season. Towards the end of the melt season supraglacial lakes in this region appear to contain between 10-30% of the area's calculated runoff.

Limitations to this portion of the study include: availability of daily MODIS imagery due to cloud cover, a lack of a high resolution DEM that spans the entire Jakobshavn region, and paucity of ground truth observations for comparisons.

The next chapter discusses the benefits of implementing unmanned aircraft for scientific data collection in the Arctic, one possible solution to alleviate the large observational gaps of certain key Arctic parameters.

Chapter 7: Why Science & Technology Policy Matter in Arctic Observations

Introduction

This study outlines the importance of making routine, repeatable, and reliable scientific observations using small Unmanned Aircraft Systems (UAS) in the Arctic region, the area expected to have the most significant response to climate change (IPCC, 1997). While this study focuses on the Jakobshavn region, it is just one place where small autonomous craft can be used in the oceanic and atmospheric regions of the Arctic for scientific observations. Earlier pathfinders employing UAS in Arctic research include Drs. James Maslanik and Judy Curry who have documented over 1,000 hours in small (Curry et al., 2004) Unmanned Aerial Vehicle (UAV) operations based mainly in Barrow, Alaska.

The actual collection of baseline earth observation data throughout the Arctic by UAS in particular will be obtainable in the near future only through the backing of the United Nations (UN) and the International Civil Aviation Organization (ICAO). It is recommended that future scientific UAS flights occur under a special use category (outlined below) allocated to a limited set of specific UAV models, on specific routes, collecting specific scientific information. This recommendation is narrowly worded to ensure acceptance by the international community, and is intended only as an interim measure until full integration of UAS into international airspace is completed worldwide. Since full compliance of UAS with worldwide ICAO standards could take over a decade to complete, it is necessary now to draft and implement an interim policy for scientific observations in the Arctic.

Earth Observations in International Regions

Currently, the international community makes thousands of earth observations daily for weather forecasts, land use change, climate and resource monitoring, etc. The importance of earth observations is manifest by the number of international organizations set up to ensure the accuracy and sustainability of these observations. The United Nations (UN) has many earth observation entities under its auspices, such as the World Meteorological Organization (WMO), the Global Climate Observing System (GCOS), the Global Ocean Observation System (GOOS), and the Global Terrestrial Observing System (GTOS). Part of the WMO charter is "To facilitate worldwide cooperation in the establishment of networks of stations for the making of meteorological observations as well as hydrological and other geophysical observations related to meteorology, and to promote the establishment and maintenance of centers charged with the provision of meteorological and related services" (www.wmo.int/pages/themes/observations/index_en.html).

To this end, countries such as the United States (US) make measurements within their borders, which can be shared worldwide. Currently the US launches over 200 weather balloons per day to measure upper-air atmospheric properties for NOAA and other organizations (www.wrh.noaa.gov/rev/tour/UA/introduction.php). Throughout the world other countries are also obtaining readings to help their societies lead safe and productive lives, supporting, for example, farming, industry, maritime, and other needs. While these airborne measurements have been collected for 100 years in populated areas, (www.history.noaa.gov/legacy/noaahistory_6.html), the remote areas of the world have sparse data sets. Advances in computation technology has allowed for the

development of Global Climate Models (GCM's), which provide considerable help in forecasting; but it is only by initializing these models with real data points that we can actually harness the power of the computer models. Otherwise stated, sparse input data sets lead to more ambiguous results.

These national efforts have been functioning well for decades within the borders of participating nations, but there are large gaps in coverage over remote non-national regions, and in the Arctic in particular, as noted by the Integrated Global Observing Strategy (IGOS) in 2007.

The United States, under Section H of the Presidential Directive NSPD-66/HSPD-25 (White House, 2009) states, "Despite a growing body of research, the Arctic environment remains poorly understood. Arctic environmental research, monitoring, and vulnerability assessments are top priorities."

Over the world's oceans, data have also been historically sparse. However, in the last nine years over 3,000 Argo buoys have been fielded by nations worldwide in a cooperative international program that is now providing the ocean community with in-situ measurements. One key reason for the success of obtaining scientific data in remote international oceanic waters is the fact that the profiling floats are *autonomous*. Could one imagine what the expense would be to obtain the same measurements via human-operated vessels? Not to mention the safety problems of data acquisition as the weather degrades; or even worse, during a cyclone. Instead, if a few of these autonomous buoys are lost over time to such disastrous events it is not a tragedy, but a "non-event" that is labeled as attrition and solved by replacing the lost buoys. Potential human catastrophes

are avoided, and more robust scientific data sets are obtained. It is suggested that these ocean buoys serve as a prequel to Arctic observations via UAS.

International Governance

Beyond the lack of scientific observations, even the governance of the Arctic Oceanic region is problematic. The Arctic does not have an all-encompassing legal system binding nations towards compliance or resolution in areas of disagreement. This is quite different from the Antarctic continent, where the Antarctic Treaty System (www.ats.aq) ratified by 47 countries, oversees international behavior (Proelss, 2009). To reconcile this, the Arctic Council was established in 1996 as a "high level intergovernmental forum to provide a means for promoting cooperation, coordination and interaction among the Arctic States" (www.arctic-council.org). Globally, its membership is limited to nations with an actual Arctic presence, and consists of Canada, Denmark (including Greenland and the Faeroe Islands), Finland, Iceland, Norway, Sweden, the Russian Federation, and the United States of America, as illustrated in Fig. 7-1. There are also Arctic Council Observer Status entities that include non-Arctic nations, inter-governmental, and non-governmental organizations (NGO's).

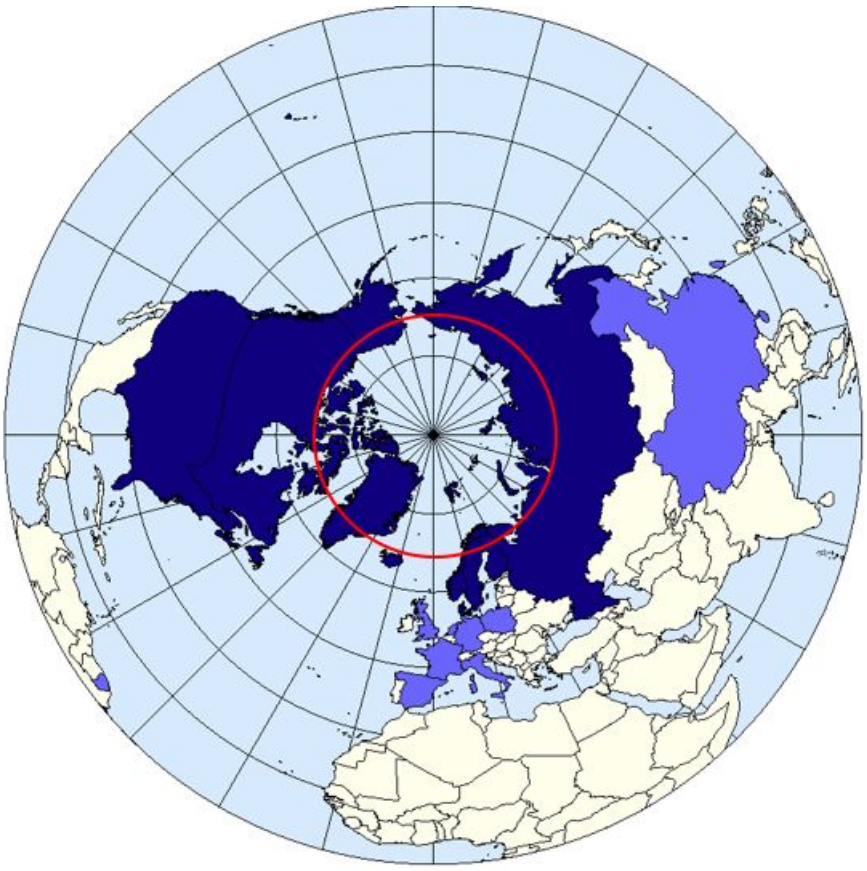

Fig. 7-1: The Arctic Council Member States
shown in dark blue, the Observer States in light blue.
The Arctic Circle is shown in red (Suioy, Public Domain).

Therefore, the Arctic Council's endorsement is very important for internationally accepted policy changes, regarding the Arctic. However, these changes must be adopted by the UN and related entities such as ICAO for full effect. Of note, while Iceland, Finland, and Sweden are sometimes referred to as Arctic states, they do not have any "territorial" right with regard to the Arctic Ocean (Proelss, 2009). For all the reasons noted above, it is therefore imperative that an interim policy for obtaining scientific observations via UAS be drafted.

It is interesting to note while a strong legal framework in the Arctic does not exist, it is also not sought after by the Arctic Member states. The text of "The Ilulissat

Declaration" in May 2008, made by the five coastal nations bordering the Arctic Ocean (Canada, Denmark, Norway, the Russian Federation, and the United States of America), proclaims "We therefore see no need to develop a new comprehensive international legal regime to govern the Arctic Ocean." This would imply acceptance by the five coastal nations to provide the leadership themselves to make necessary recommendations of change to current international laws applicable to the Arctic, which still must be accepted by the entire international community. This includes changing those laws unsupportive of observing the Arctic for scientific purposes; in particular, the restrictive ICAO regulations for operating small UAS in international airspace over the Arctic Ocean.

US Arctic Policy and the UN Law of the Sea Treaty

Internally, the United States has elevated the importance of Arctic Policy, one year ago releasing a new Presidential Directive (White House, 2009) outlining US intentions. This is the first Arctic policy change in 15 years. Section A, item 6 states "It is the policy of the United States to enhance scientific monitoring and research into local, regional, and global environmental issues"; it further states that National Security interests are "...in the Arctic region...ensuring freedom of navigation and overflight". The policy also recommends the US Senate to promptly ratify the UN Convention on the Law of the Sea (UNCLOS), an international treaty currently ratified by 159 other countries (as of November 4th, 2009). This treaty was signed by the US in 1994, but the Senate still has not ratified it. Certain parts of the UNCLOS framework could be translated directly into the airspace above the Arctic Ocean as guidelines for Arctic flights, other parts would need to be modified. In particular, aspects pertaining to earth observations beyond a state's recognized 12nm (nautical mile) territorial zone, yet within the state's 200nm

Exclusive Economic Zone (EEZ) would need to be addressed; this area could become an impediment to the operations of UAS within the Arctic for scientific data collections under strict UNCLOS provisions.

Advances in Unmanned Aerial Vehicles and Systems

The recent movement of UAV's towards maturation was no doubt spurred by the dual US campaigns in Afghanistan and Iraq. The US had flown over 500,000 hours of UAV missions as of January 2008 (Associated Press, 2008). Advancements have been so dramatic the military is contemplating future bomber aircraft to be unmanned (Scully, 2009); it is generally acknowledged the F-35, currently in production, will be the last manned fighter for the US. However, the employment of small UAV's for earth observation data collection has not received much attention by the scientific community, or by policy makers. This is due to the unrecognized rapidity of the UAV advancements over the last decade, and their applicability toward science. Additionally, the unknown capabilities of miniaturized systems that could be installed in UAS to collect scientific data have been overlooked by the science community.

The conjunction of science and policy is now required to make future earth observation collections in the Arctic possible on a routine, repeatable, and reliable basis for use by scientific personnel. This approach mirrors the advances made during the 1990's with ocean buoy technology, enabling autonomous data collection across the world's oceans during the first decade of the 21st century. Again, it must be stressed that the scientific need is for small, affordable long-endurance UAS, not large expensive platforms that have been shown to be costly and problematic for the Department of Defense and Congress (GAO, 2009).

UAV variants range in size from tiny insect-sized devices, to extremely large systems the size of Boeing 737 jetliners. Obviously, the resources required to operate these systems vary exponentially, especially in terms of cost. For scientific missions, the engineering requirements would be in the middle of current UAS designs for most parameters, with the notable exception of mission duration. For remote locations, it is most useful to have long-endurance, both for maximum on-station time and to be able to make long transitions from an adequate launch site to the operational area. UAS would need to be of small size, yet have a modest cargo bay, so various scientific payloads could be installed; sometimes this is referred to as a multi-mission platform. The micro-sized UAS platforms would lack both duration and payload capacity, while large UAS involve excessive cost and over capacity. Therefore it is the small UAS that will best meet requirements. It is noted that many instruments such as lidar systems would need to be miniaturized to fit into a small UAS, but the immense data collection opportunities overcome the engineering costs.

As noted above, there have been considerable advances by industry in UAS over the past decade. It is recognized that there are over 200 UAV designs just in the US (www.uavforum.org), which would make an ICAO blanket approval of UAS operations in the Arctic impossible. Additionally, the cost to any of the Arctic Council nations operating a disparate fleet of platforms to obtain scientific data would be much more than operating a few Certificated platforms. Limiting certification acceptance in the Arctic scientific research category would solve these problems and provide opportunities for commonality between nations. Commonality is a key factor in cost control of UAS (GAO, 2009). This does not imply in any way that exclusivity would continue to exist once the

full integration of UAS into international airspace is obtained, just during the interim period. In fact, limiting platforms would be detrimental to innovative science.

A small UAS, which in this study is subjectively defined as less than 40kg (88lbs), would be of such construction as to minimize damages if involved in an impact, utilizing such things as breakaway wings, fuselage, etc. These built-in safety requirements could alleviate some issues with the operation of UAS in remote regions, by mitigating the damages if a collision were to occur.

International Support for Earth Observations in Data-Poor Regions

There have been numerous frameworks adopted by the international community for sparse regions of earth observational data. In particular, the ten basic principles adopted by the Conference of the Parties (COP) to the UN Framework Convention on Climate Change (UNFCCC) in December 2003 outline justifications to remedy the situation. Principles 7 and 8, reproduced in the text below, indicate the worldwide desire to implement new observations in data-poor regions of the world, and to generate long-term requirements to facilitate engineering and operations to successfully carry out such earth observations on a regular basis (http://www.wmo.ch/pages//prog/gcos/index.php).

Principle 7 states: High priority for additional observations should be focused on data-poor regions, poorly observed parameters, regions sensitive to change, and key measurements with inadequate temporal resolution.

Principle 8 states: Long-term requirements, including appropriate sampling frequencies, should be specified to network designers, operators and instrument engineers at the outset of system design and implementation.

It is proposed that an Arctic-focused earth observation requirement list be generated; it would leverage input from existing international structures instead of creating another organization. Secondly, the conversion from a research observing system into long-term systematic observations, in a carefully planned manner, cannot be underemphasized.

A Regional Approach to Data Collection in the Arctic

A key benefit of international scientific groups is the collaboration and acceptance over what scientific data should be collected worldwide, and how to encourage collection efforts of these data. Relevant examples can be taken from the GCOS community that enumerated 44 Essential Climate Variables (ECV's) for worldwide data collection. These variables are key inputs for such entities as the UNFCCC and IPCC. Examples of atmospheric ECV's are: Air temperature, Precipitation, Air pressure, Wind speed and direction, Water vapor, Earth radiation budget (including solar irradiance), Upper-air temperature, Cloud properties, Carbon dioxide, Methane, Ozone, and other long-lived greenhouse gases (www.wmo.ch/pages/prog/gcos/index.php). Similar efforts are being made in the cryospheric community, with ECV's such as snow cover extent, snow water equivalent, and snow cover duration being developed (Armstrong et al., 2009; IGOS, 2007).

It is proposed that a similar list of internationally acceptable variables for the Arctic, acquirable via UAS, be defined as Arctic Key Parameters (AKP's). Applicable AKP's would come from recommendations by GCOS, GOOS, GTOS, and other internationally recognized entities. This would create an ecosystem-based observation strategy vs. a

traditional community-based strategy, such as the existing ocean or atmospheric focused networks.

The remote Arctic region discussed in this study includes both national and international waters and airspace. Within a sovereign Arctic nation, many AKP's are likely already being acquired; if not, they could be acquired through national means. It is precisely because AKP's are also outside national jurisdictions that the global community needs to address the requirement to obtain such baseline data. This study is written to emphasize this point; if important baseline data could be obtained via traditional methods, collection efforts would already be in place. However, we currently have sparse datasets of the Arctic region because of its remoteness and forbidding climate. This is why the UAS solution is unique; it can cover large areas with full instrumentation, obtaining robust datasets in relatively little time.

Why are UAS not in operation in the Arctic today? It is not due to a lack of technology, as many successful scientific expeditions have shown. It is based purely on administrative regulations: the world community has not truly addressed the need for UAS-based scientific observations. This is largely due to lack of awareness of the capabilities, potential, and benefits of an autonomous system. As with the ocean buoy networks in the 1990's, the time has come for science and policy to merge, allowing for sustained Arctic Key Parameters (AKP's) to be collected.

This proposal to generate AKP's parallels the recommendation made by IGOS that "The report does not propose to establish a new, dedicated and stand-alone observing system for the cryosphere," but goes a few steps beyond requirements generation. This study is attempting to facilitate the actual collection of the AKP's by changing the way

small UAS, operating on scientific missions, are handled by the international aviation community. Only by describing the earth observations required, and the realization that UAS can fill part of that need, will there be any hope in an international aviation agreement on operational changes to UAS scientific data collection.

Assuming the international community agrees on the specific AKP's, the next question will be how to collect the data. Using existing platforms and techniques is not the subject of this paper as those methods are proven, but the spirit of exchange will be highlighted to show the current international good-will in overcoming obstacles in the pursuit of shared, reliable scientific data sets. For example, the Ocean Facilities Exchange Group (www.ofeg.org) uses bartering for better allocation of sea time between European countries on oceanographic vessels. In this spirit, the goals of observing the AKP's should be kept in mind when deliberating the merits of modifying international Arctic airspace regulations to allow for scientific UAS flights.

Summary of Problem

Summarizing the problem, there appears to be a conundrum in acquiring new scientific observations in the Arctic:

1) The world has numerous international science organizations desiring observations, however,

2) adequate observations are not being taken (such as accurate snow depth on sea ice) mainly due to the remoteness and expense of Arctic observations, and,

3) various established governmental entities insist they do not need another international organization to enable governance over the Arctic Ocean, yet

4) current governance policies designed for the lower latitudes negate and block implementing technological solutions to obtaining more observations over the Arctic Ocean.

A block diagram of a potential solution path is shown in Fig. 7-2.

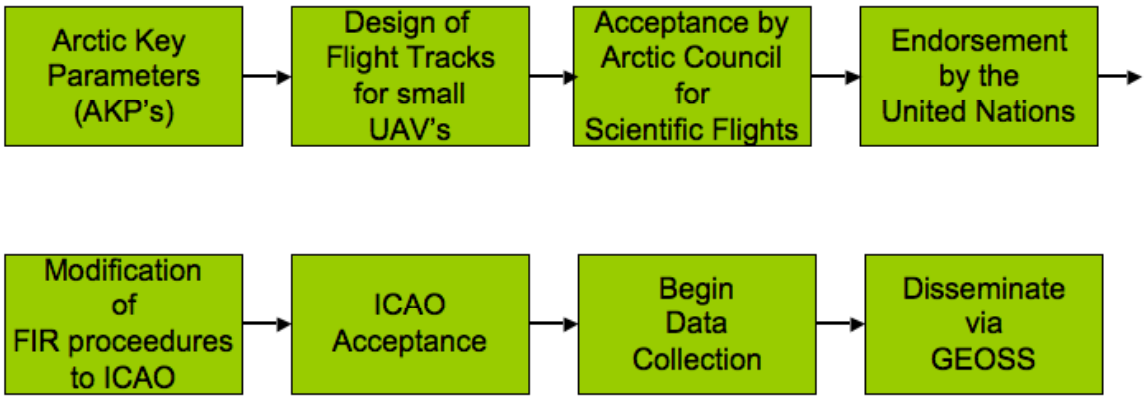

Fig. 7-2: A flow diagram to obtain AKP's (Arctic Key Parameters).

ICAO and UAS flights in Support of Science Objectives

Taking AKP's from the scientific community to the Arctic Council for endorsement would be extremely useful in advancing the acceptance of ICAO, the international aviation governing body with a membership of 190 Contracting States. Limiting the scope of UAV flights to scientific measurements on pre-approved routes, and collecting only pre-approved AKP's, will negate other UAV mission types (such as new platform testing). This is required while the international aviation community solves the problem of integrating UAV's into international airspace in a general sense. However, the recommended approach will still allow for baseline measurements of AKP's in the Arctic to be made, that otherwise would be neglected for years. Fig. 7-3 shows the numerous Flight Information Regions (FIR's) requiring approvals to operate a UAS over the Arctic. Even for a short

mission, due to the “wedges” designed by ICAO, numerous authorities must be interfaced with, even though it is a sparsely populated area.

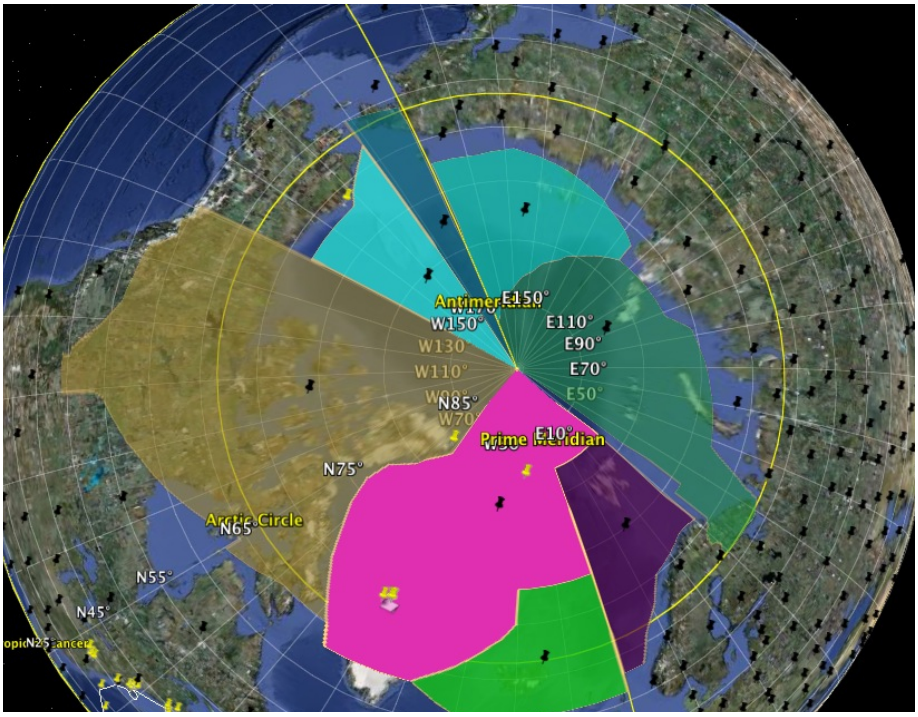

Fig. 7-3: Wedged-shaped Air Traffic Control regions in the Arctic each requiring specific coordination under the auspices of ICAO.

After contacting the manager of the ICAO Study Group on UAS in early 2009, it was indicated that ICAO approvals of such scientific flights could be obtained, assuming agreements were made beforehand between the countries involved. This is why approval by the Arctic Council is critical, as it represents all nations bordering and within the Arctic Circle.

A second issue brought up by ICAO is the requirement of an Airworthiness Certificate by any UAV that would fly in the Arctic region. Small UAV’s could meet this requirement (and indeed it has already been met by the large Global Hawk UAS) by applying directly to the appropriate aviation authority (the FAA in the US). However, this could lead to a chicken and egg situation: Why give an Airworthiness Certificate if there

are no approved areas to fly a UAV? Alternatively, why designate a region to fly UAV's if there are no authorized platforms to fly in such a region?

This study, therefore, recommends a leadership position to establish the scientific requirements for Arctic earth observations, followed by the international authorization of UAS flights in international Arctic airspace. Industry will then respond with the appropriate platforms to be certificated, once it knows what the actual requirements are.

A third issue ICAO brought up is the physical location of the pilot, and how that legally comes to bear during regular flights and mishaps. Technology is now in place to physically launch a long-endurance UAS from a ground site in the Arctic, then operationally hand it off to controllers anywhere in the world who fly the main portion of the mission, and finally return the control to the local base for landing. To alleviate the multi-national legal issues, a requirement could be levied that all phases of flight be controlled by pilots physically located within the borders, or on vessels under the authority of Arctic Council Member nations only. Therefore, accountability remains within the Arctic Council Member states.

Data Collection and Dissemination

The distribution of all data collected via UAS in operations under this proposed framework would be via the Global Earth Observation System of Systems (GEOSS). GEOSS strives to become the world's portal for observing systems, providing "information for the benefit of society." This distribution method is logical since the approval for these flights was based on the necessity of collecting AKP's for all nations, not just the Arctic Council Members. Baseline scientific data are essential for modeling efforts worldwide. In fact, US policy in the Arctic under Presidential Directive NSPD-66/HSPD-25 is to

"Promoting International Scientific Cooperation," and specifically under section E.2 "The United States promotes the sharing of Arctic research platforms with other countries in support of collaborative research that advances fundamental understanding of the Arctic region in general and potential Arctic change in particular." Further, it encourages efforts such as UAS earth observations by stating that it will "Lead the effort to establish an effective Arctic circumpolar observing network with broad partnership from other relevant nations."

Notional Trans-Arctic AKP Mission Scenario

Consider a notional trans-Arctic UAS mission that would measure sea ice thickness, snow depth on top of the sea ice, freeboard height of the sea ice, ocean surface temperature, atmospheric pressure, temperature, humidity, while imaging the ocean/ice surface as the UAS passes overhead. This hypothetical experiment could collect data on low-level tracks (<1000m) between Barrow, Alaska, and Tiksi, Russia over a three-week period. In comparing anticipated costs, a governmental agency that operates manned scientific aircraft was contacted for a rough price estimate, along with two different contractors who each developed an unmanned aircraft that potentially meets the mission requirements. Fig. 7-4 shows the notional flight paths for this exercise.

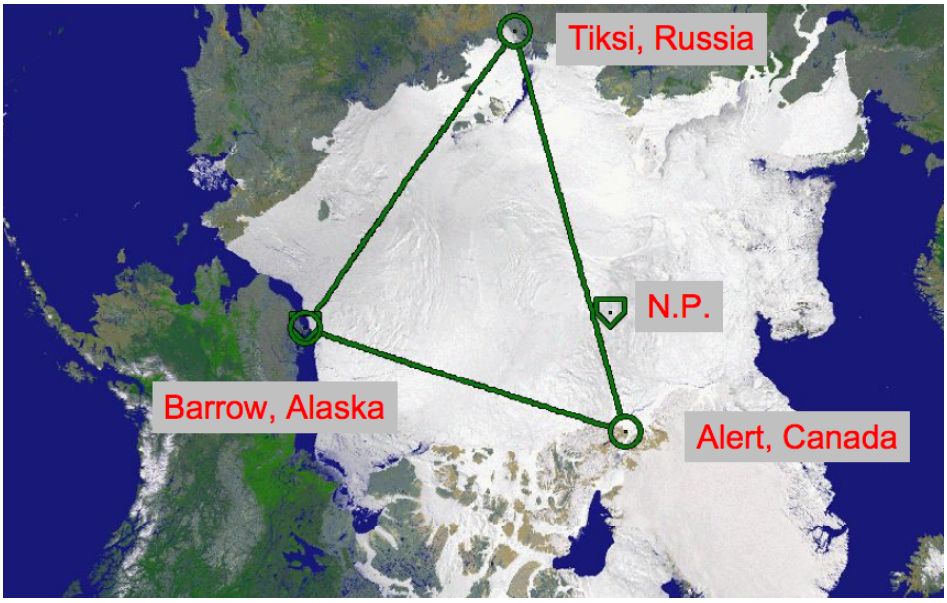

Fig. 7-4: Notional trans-Arctic flight lines including the Barrow-Tiksi leg discussed in this study (distance = 2472km).

One key difference between the manned aircraft and the UAS was flight duration. The manned aircraft were limited to 8-10 hours, while the unmanned aircraft could remain aloft for 18-24 hours. The manned project would require the choice of a large aircraft with the range to make the trans-Arctic flight, or the use of smaller twin-engine aircraft that could fly out halfway but then must return. In all comparisons, the manned flight costs were lower than the unmanned flight costs; the largest differential being 16%. While this appears to favor manned aircraft, other factors must be discussed beyond perceived flight costs.

The most overlooked factor in UAS operations is the availability of multiple platforms on-site for data collection. This ensures data collection even if the primary aircraft is non-operable for whatever reason; a factor rarely available in manned aircraft. In manned aircraft missions, if the plane is down, all science stops. In unmanned aircraft, the second platform is launched and the science continues.

Two other key points are: manned aircraft cost estimates do not take into account the true price of the airframe, and they do not account for missed science days (it is assumed the aircraft will always be available except for planned maintenance). While this was not a true apple-to-apple comparison, it is argued the costs of manned vs. unmanned aircraft are for all intents equal. Therefore, a conclusion could be drawn that while UAS are not the least-cost solution, they are the best value option, which does justify their implementation in remote regions.

Recommendations

It is proposed to change existing international flight regulations in the international airspace of the Arctic (> 66.5° North) to enable the systematic collection of AKP's by small (< 40kg) long-endurance (> 16 hours) UAS flying on pre-approved flight tracks and altitudes. Pre-approved tracks are essential to the approval process. It will allow for:

1. A priori knowledge of potential conflict areas,

2. All eight Arctic nations to adjust their air traffic control routines, as applicable,

3. Dissemination to all manned pilots of these UAS routes and their activation via the traditional Notice to Airmen (NOTAM) system, which publishes daily flight notices worldwide.

Additionally, all UAS are to be equipped with satellite two-way command and control links, and a transponder that is compatible with Traffic Alert/Collision Avoidance System (TCAS), or its equivalent. Other important requirements such as lost communications procedures should be standardized, but will not be discussed in this study, since the objective is to obtain international acceptance of UAS to measure Arctic Key Parameters.

A final recommendation is that all UAS flights be operated only under the direct auspices of an Arctic Council Member governmental entity. For instance, the US could fly under the National Oceanic and Atmospheric Administration (NOAA) or the National Aeronautics and Space Administration (NASA) where the UAS would be owned or leased for scientific missions. However, the US manufacturer of the UAS would not be able to fly missions without government sponsorship until the ICAO international agreement on UAS integration is fully implemented. This would ensure the UAS is seen as a State Aircraft, and not a private venture. In conjunction, a maximum liability for small UAS operating under such a scenario would be limited to $3 million dollars in damages, double the current liability required by some nations for small UAS operations. This will ensure an equitable settlement in case of a mishap, while negating any arbitrary onerous payments.

Chapter Summary

Scientifically-based Arctic Key Parameters (AKP's) are needed throughout the data sparse Arctic to better understand our environmental processes. Similar to the global buoy networks, the technological challenges to collect many AKP's have been met, it is only administrative issues that keep the world from obtaining better in-situ and remotely sensed data in the Arctic. International cooperation is desired for both the scientific rationale, and aviation oversight, of UAS-based earth observations in the Arctic. Listing specific routes, equipment, and observations to be collected provides a framework for mission and platform designs. Allowing only Arctic Council State Aircraft designations to fly approved missions will limit UAS operations until the international community,

through ICAO, implements UAS into worldwide air traffic control. All collected data will be immediately available to all parties worldwide via GEOSS.

The next chapter is the conclusion of this dissertation, and offers ideas for future work in the study of supraglacial lakes on the Greenland Ice Sheet.

Chapter 8: Summary and Conclusions

Overview

Global sea level rise is influenced by contributions from the Greenland Ice Sheet (GIS), both in the frozen form of icebergs calving into the sea, and in the liquid form of surface runoff. Supraglacial lakes store some of the GIS runoff until they drain, releasing the water onto and inside of the ice sheet. Quantifying this water volume is problematic.

Supraglacial lake depth measurement in the Jakobshavn region of western Greenland is an important, yet elusive task due to high costs, remoteness of the region, and environmental complexity. To assist with this problem, the first scientific unmanned flight operations over the GIS were carried out in 2007 and continued into the summer of 2008. This study, entitled Arctic MUSCOX (MUltiSensor Cryospheric Observation eXperiment), used many data sources and observation platforms to quantify four supraglacial lake volumes throughout three melt seasons along a 68.73°N transect of the GIS. Additionally, a new model for surface runoff calculations was developed based on observed surface height change measurements at AWS stations.

Supraglacial lakes result from melting summer snow and ice, which become runoff that collects in local depressions on the surface of the GIS. Many lakes completely drain into the ice sheet during the summer melt season, some have drained in less than 24 hours, adding both water and energy into the GIS via moulins and/or crevasses. The effects of these seasonal supraglacial lake drainages on outlet glacier discharge rates are not understood. One key parameter necessary to understand the surface and internal processes is determining the actual water volume in supraglacial lakes.

Measurements of the areal size of supraglacial melt lakes on the GIS have been well documented using satellite imagery (Box and Ski, 2007; Sneed and Hamilton, 2007; Sundal et al., 2008). However, determining the depth of these lakes is problematic (Sneed and Hamilton, 2007) and various techniques have produced mixed results. McMillan et al. (2007) studied 292 supraglacial lakes in the Jakobshavn region, and attempted to determine supraglacial lake depths by dividing runoff (determined by a Positive Degree Day model) by the observed lake areas to get an average lake depth. Like other lake depth or volume studies, the values obtained were not corroborated with in-situ measurements.

In this study, a recently drained supraglacial lake was mapped in three dimensions using a UAV profiling lidar with postings at 90m intervals. These data enabled the depth of the first of four lakes to be determined, which was in agreement with in-situ pressure sensor readings taken during the same time frame (Das et al., 2008). Lake areal extent was determined by employing two 250m MODIS imagery channels, maximizing horizontal resolution and temporal measurements. Employing MODIS areal extent as a mask, ASTER DEM datum points were obtained for depth determination, and volume calculations were performed on Lake 1.

The ASTER volume information was then corrected by using the MUSCOX-derived DEM and in-situ pressure data. Finally the three remaining lake volumes were determined by applying the same ASTER DEM correction value to the appropriate MODIS masks. This technique leverages the single lake volume estimate from the lidar survey to be scalable to other lakes.

Results

The results of this study show supraglacial lake lifespans vary annually on an individual basis, but some general trends are apparent. First, the maximum volume for any observed lake was 0.147km^3; the maximum surface area observed was 10.4km^2.

Second, lake size changes were fairly smooth during the period the lakes were filling, but very abrupt in the drainage phase. This suggests a catastrophic change in the ice structure below or along the edges of the supraglacial lake, probably a result of either a direct bottom rupture into the ice sheet via a moulin, or a side rupture via an outflow crevasse that continues along the surface of the ice sheet.

Third, the infrequent optical viewing of the lakes from satellites inhibits daily monitoring. Usable cloud-free MODIS imagery is one of the major limitations of this technique. Small unmanned aerial systems could provide glimpses under the cloud cover in addition to making direct observations using lidar.

Using observed dH measurements at two AWS sites in the ablation region, a new model for runoff calculations was created, termed the dH Model. The dH Model did show very close results for runoff calculations at JAR1 and JAR2. On a daily basis, the observed snow or ice surface height changes were converted into liquid water, and adjusted for sublimation and elevation change. Runoff was then calculated over the Jakobshavn region, and for a smaller inset strip where the four lakes were located.

Daily supraglacial lake volumes were produced for each of the 42 individual days of usable MODIS imagery spanning the 3 melt seasons of 2006, 2007, and 2008. Early in the melt season, runoff from the inset strip did not appear to produce enough water for the observed lakes. It is thought that a representative area that included more equal

elevation contours could account for the early season's missing water. Later in the melt season comparing the lake volumes to the calculated runoff over all three years, it is estimated that 10-30% of runoff is stored in the form of supraglacial lakes.

A final analysis involves the anticipated effects that a +0.5°C to a +3.0°C average atmospheric temperature increase would have on supraglacial lake formation. It is anticipated more lakes will form due to a temperature increase, and due to the flatter slopes of ice sheet at higher elevations. At +3.0°C it is calculated that the area favorable to supraglacial lake formation will increase by 43%.

Next Steps

The results of this study show the importance of an accurate, high-resolution DEM for both runoff calculations and lake volume determination. Further, it showed that more temporal resolution is needed than overhead imagery can provide to adequately monitor the supraglacial lakes. An airborne bathymetric lidar system that directly measures supraglacial water depth could provide a solution that mitigates both problems: it can sample with high resolution, and it can be flown in all but the lowest cloud deck situations (<500m), skirting issues that inhibit satellite optical measurements. Additionally, an unmanned airborne system can sample many lakes over a few hour period with minimal risk. Further, an unmanned aerial vehicle could make numerous repetitive flight tracks in remote and expansive regions without the expense and availability issues of manned platforms.

In the future, studies focusing on englacial conduit structures should be emphasized to understand how runoff and drainage water flow on top of and within the ice sheet. Limited information exists on englacial processes in the ablation region of the

GIS. Only by knowing the entire flow pattern of runoff can one determine its effects on the ice sheet and glacial outflow velocities.

Concluding Remarks

This project is a mirror of the larger problems facing the scientific community in the Arctic (and other remote regions) today. A serious challenge involves adequate sensor placements in international regions that are very remote. The lack of governance in the Arctic inhibits operational projects that require international cooperation. A potential solution to gathering more robust atmospheric and surface datasets in the Arctic for the international community, as presented in Chapter 7, is to first develop Arctic Key Parameters (AKP's) agreed to by the United Nations and its affiliates. Deploying emerging technologies in innovative ways will allow for better scientific understandings of climate, ecosystems, and the role that humans play in the earth's systems.

Bibliography

Abdalati, W. and K. Steffen (1997), Snowmelt on the Greenland ice sheet as derived from passive microwave satellite data, *Journal of Climate*, *10*(2), 165-175.

Ahrens, C. D. (2007), *Meteorology Today 8th Edition*, Thompson Brooks Cole, California.

American Meteorological Society, (accessed 2009), http://amsglossary.allenpress.com/glossary.

Arctic MUSCOX (accessed 2010), http://arcticmuscox.org

Armstrong, R., et al. (2009), Assessment of the status of the development of the standards for the Terrestrial Essential Climate Variables, *Global Terrestrial Observation System Secretariat*, Rome, Italy.

Associated Press (2008), *Rise of the Machines: UAV Use Soars*, Associated Press, January 2nd.

Bamber, J. L., et al. (2001), A new, high-resolution digital elevation model of Greenland fully validated with airborne laser altimeter data, *Journal of Geophysical Research-Solid Earth*, *106*(B4), 6733-6745.

Benson, C.S., (1960), *Stratigraphic studies in the snow and firn of the Greenland ice sheet*, Cold Reg. Res. And Eng. Lab., Hanover, New Hampshire, Res. Rep. 70.

Box, J. E. and K. Ski (2007), Remote sounding of Greenland supraglacial melt lakes: implications for subglacial hydraulics, *Journal of Glaciology*, *53*(181), 257-265.

Box, J. E. and K. Steffen (2001), Sublimation on the Greenland ice sheet from automated weather station observations, *Journal of Geophysical Research-Atmospheres*, *106*(D24), 33965-33981.

Christopherson, R. (2009), *Geosystems, 7th Edition*, Pearson Prentice Hall, Upper Saddle River, New Jersey.

CRC Handbook of Chemistry and Physics (2008-2009), *CRC Press*, David Lide, editor, 89th edition.

Cullen, N. J., et al. (2007), Nonstationarity of turbulent heat fluxes at Summit, Greenland, *Boundary-Layer Meteorology*, 122(2), 439-455.

Curry, J. A., et al. (2004), Applications of Aerosondes in the Arctic, *Bulletin of the American Meteorological Society*, 85, 1855-1861.

Das, S. B., et al. (2008), Fracture propagation to the base of the Greenland Ice Sheet during supraglacial lake drainage, *Science*, *320*(5877), 778-781.

Dowdeswell, J. A. (2006), The Greenland Ice Sheet and Global Sea-Level Rise, *Science*, Vol. 311, 963-964.

GAO (2009), Defense Acquisitions, Opportunities Exist To Achieve Greater Commonality And Efficiencies Among Unmanned Aircraft Systems, *US Government Accountability Office*, Report to the Subcommittee on Air and Land Forces, Committee on Armed Services, House of Representatives.

Geiger, R. et al. (2003), *The Climate Near the Ground*, Rowman & Littlefield, Oxford, United Kingdom.

Greuell, W. (2000), Melt-water accumulation on the surface of the Greenland ice sheet: Effect on albedo and mass balance, *Geografiska Annaler Series a-Physical Geography*, *82A*(4), 489-498.

Hanna, E., et al. (2005), Runoff and mass balance of the Greenland ice sheet: 1958-2003, *Journal of Geophysical Research-Atmospheres*, *110*(D13).

Hanna, E., et al. (2006), Observed and modeled Greenland ice sheet snow accumulation, 1958-2003, and links with regional climate forcing, *Journal of Climate*, *19*(3), 344-358.

Hanna, E., et al. (2008), Increased runoff from melt from the Greenland Ice Sheet: A response to global warming, *Journal of Climate*, *21*(2), 331-341.

Henneken, E. A. C., et al. (1994), A Case-Study Of The Daily Energy-Balance Near The Equilibrium-Line On The Greenland Ice-Sheet, *Global and Planetary Change*, *9*(1-2), 69-78.

Hock, R. (2005), Glacier melt: a review of processes and their modelling, *Progress in Physical Geography 29,3*, 362-391.

Huff, R. and K. Steffen (accessed 2010), http://cires.colorado.edu/steffen/greenland/melt2005/

Huff, R. (2006), Melt Anomalies of the Greenland Ice Sheet and Large Scale Modes of Atmospheric Circulation, Dissertation Abstracts International, Volume: 68-03, Section: B, page: 1524.

Huybrechts, P., and J. de Wolde (1999), The dynamic response of the Greenland and Antarctic ice sheets to multiple-century climatic warming, *Journal of Climate*, *12*(8), 2169-2188.

IGOS (2007), Cryosphere Theme Report, Integrated Global Observing Strategy, *World Meteorological Organization*, Geneva, Switzerland

IPCC (1997), The Regional Impacts of Climate Change: An Assessment of Vulnerability, Watson, R. T. et al., *Cambridge University Press*, Cambridge, U.K.

IPCC (2007), Climate Change 2007: The Physical Science Basis. Contribution of Working Group 1 to the Fourth Assessment Report, *Cambridge University Press*, Cambridge, U.K.

Joughlin, I., et al. (2008), Seasonal speedup along the western flank of the Greenland Ice Sheet, *Science*, *320*(5877), 781-783.

Kaab, A. (2002), Monitoring high-mountain terrain deformation from repeated air- and spaceborne optical data: examples using digital aerial imagery and ASTER data, *Journal of Photogrammetry & Remote Sensing*, 57, 39-52.

Krabill, W. B., et al. (1995), Greenland ice sheet thickness changes measured by laser altimetry, *Geophysical Research Letters*, 22(17), 2341-2344.

Krabill, W. B., et al. (2002), Aircraft laser altimetry measurement of elevation changes of the greenland ice sheet: technique and accuracy assessment, *Journal of Geodynamics*, *34*(3-4), 357-376.

Liston, G. E. and Elder, K. (2006), A Distributed Snow-Evolution Modeling System (SnowModel), *Journal of Hydrometeorology*, 7(6), 1259-1276.

Lubin, D. & R. Massom (2006), Polar Remote Sensing (v. 1. Atmosphere and Polar Oceans & v. 2. Ice Sheets), Praxis Publishers, U.K.

Luthcke, S. B., et al. (2006), Recent Greenland ice mass loss by drainage system from satellite gravity observations, *Science*, *314*(5803), 1286-1289.

Mernild, S. H., et al. (2010), Meltwater flux and runoff modeling in the ablation area of Jakobshavn Isbræ, West Greenland, *Journal of Glaciology*, 56, No. 195.

NASA, (accessed 2009), http://imagine.gsfc.nasa.gov/docs/ask_astro/answers/980301b.html.

NASA GISS (Goddard Institute for Space Studies), (accessed 2010), http://pubs.giss.nasa.gov/

NSIDC, (accessed 2009), http://nsidc.org/data/swe.

Oke, T. R. (1987), *Boundary Layer Climates, 2nd Edition*, Methuen, London, United Kingdom.

Proelss, A. (2009), Governing the Arctic Ocean, *Nature Geoscience*, Vol 2.

Przybylak, R. (2003), *The Climate of the Arctic*, Kluwer Academic Publishers, Dordrecht, The Netherlands.

Randall, C. (2007), Class notes dated 17Jan07 and 14Feb07, *ATOC/ASEN 5235*, University of Colorado.

Reeh, N. (1991), Parameterization of Melt Rate and Surface Temperature on the Greenland Ice Sheet, *Polarforschlung*, 59/3, 113-128.

Rick, U. (2008), Meltwater Transport Through Firn In The Accumulation Zone Of The Greenland Ice Sheet, ProQuest LLC Dissertation.

Scambos, T. A., and T. R. Haran (2002), An image-enhanced DEM of the Greenland ice sheet, in *Annals of Glaciology, Vol 34, 2002*, edited, pp. 291-298.

Scully, M. (2009), Gates says next-generation bomber might fly without pilot, *Government Executive*, May 14th Congress Daily.

Sellers, W. (1965), *Physical Climatology*, University of Chicago Press, Chicago.

Serreze, M. C., and Barry, R. G. (2005), The Arctic Climate System, *Cambridge University Press*, Cambridge, U.K.

Serreze, M. C. and J. A. Francis (2006), The arctic on the fast track of change, *Weather*, *61*, 65-69.

Steffen, K. (1995), Surface energy exchange at the equilibrium line on the Greenland ice sheet during the onset of melt, *Annals of Glaciological Society*, 21, 13-18.

Steffen, K., and J. Box (2001), Surface climatology of the Greenland ice sheet: Greenland climate network 1995-1999, *Journal of Geophysical Research-Atmospheres*, *106*(D24), 33951-33964.

Sundal, A. V., et al. (2009), Evolution of supra-glacial lakes across the Greenland Ice Sheet, *Remote Sensing of Environment*, 113, 2164-2171.

Truffer, M. and M. Fahnestock (2007), Rethinking Ice Sheet Time Scales, *Science*, Vol . 315, 16 March, 1508-1509.

USGS, (accessed 2009), http://vulcan.wr.usgs.gov/Glossary/Glaciers/glacier_terminology.html

van den Broeke, M. et al. (2008), Surface radiation balance in the ablation zone of the west Greenland ice sheet, *Journal of Geophysical Research*, *113*(D13).

van den Broeke, M. et al. (2009), Partitioning Recent Greenland Mass Loss, *Science*, 326, p 984.

Vaughan, D. G. and R. Athern (2007), Why Is It Hard to Predict the Future of Ice Sheets?, *Science*, 315, 1503-1504.

Warren, S. G. (1982), Optical-Properties Of Snow, *Reviews of Geophysics*, *20*(1), 67-89.

White House, (2009), National Security Presidential Directive and Homeland Security Presidential Directive, NSPD-66/HSPD-25.

Zwally, H. J. and M. B. Giovinetto (2001), Balance mass flux and ice velocity across the equilibrium line in drainage systems of Greenland, *Journal of Geophysical Research*, 106, D24, 33, 717-33, 728.

Zwally, H. J. et al. (2002) Surface melt-induced acceleration of Greenland ice-sheet flow, *Science*, 297, 218-222.